Experimental and Modeling Study of Nickel, Cobalt and Nickel-Cobalt Alloy Electrodeposition in Borate-Buffered Sulphate Solutions

by

Jorge Gabriel Vazquez

A thesis
presented to the University of Waterloo
in fulfillment of the
thesis requirement for the degree of
Doctor of Philosophy
in
Chemical Engineering

Waterloo, Ontario, Canada, 2011

AUTHOR'S DECLARATION

I hereby declare that I am the sole author of this thesis. This is a true copy of the thesis, including any required final revisions, as accepted by my examiners.

I understand that my thesis may be made electronically available to the public.

Abstract

Nowadays, the development of novel materials involves diverse branches of science as a consequence of the new requirements imposed by modern society. This includes aspects ranging from the optimization of the manufacturing processes to the durability of the materials themselves. Ideally, some synergism should exist between the durability, the properties of interest in the material. Although metals in their pure state are often desired, the best properties or combination of properties often cannot be satisfactorily achieved with a single metal. In these situations, the desired properties can be attained by the formation of alloys of these metals with others. Ni-Co alloys are no exceptions and so have received considerable attention especially in microsystem technology due to the magnetic properties of cobalt and the corrosion and wear resistance of nickel. Moreover, this interest has been further stimulated by its use in the manufacture of sensors, magnetic devices, microrelays, inductors, actuators, memory devices and hard drives. The fabrication of these alloys (particularly coatings) via electroplating has been shown to be techno-economically feasible in comparison with other processes: capability of high volume production, low cost and the ability to coat thin layers on non-planar substrates. In addition, the materials fabricated by this technology exhibit excellent characteristics such as refined grain structure, smoothness, low residual stress and coercivity, etc., making them advantageous to materials produced by other physical methods of deposition.

Nevertheless, one of the biggest problems faced during the formation of Ni-Co alloys is its anomalous behavior whereby cobalt preferentially deposits over nickel under most conditions, even when the Ni(II) concentration is significantly higher than that of Co(II). This problem has complicated the prediction and control of the metal composition in these alloys during their production and as a consequence the ability to obtain the desirable properties associated with high nickel content. Although this problem is not recent, the studies that have been carried out so far to analyze this system have not always been as comprehensive as they could be in terms of the experimental conditions investigated or the reaction mechanisms and mathematical models developed to describe its behavior. Consequently, the origin of this behavior is still not completely understood. Thus, this work presents a contribution in terms of the analysis of the reaction mechanisms for single metal deposition of nickel and cobalt and for the formation of Ni-Co alloys in sulphate media with the intention of gaining a better understanding of the phenomena controlling the anomalous behavior of this system.

Analyses of the single metal deposition of nickel and cobalt are first carried out to better understand their reaction mechanisms. Such an approach should allow the contributions of the reduction of each metal ion and interactions between the two systems during alloy co-deposition to be more clearly understood. In order to analyse the aforementioned systems, both steady state and transient techniques are employed. Among these techniques, electrochemical impedance spectroscopy (EIS) is employed since it is a robust and powerful method to quantitatively characterize the various relaxation phenomena occurring during the electrodeposition of metals. The experimental data acquired from this technique are analyzed with comprehensive physicochemical models and the electrochemical processes are quantified by fitting the models to these data to determine the kinetic parameters. During the development of the physicochemical models, several assumptions (e.g. neglect of convection, homogeneous reactions and single electron-transfer steps) made in former models are relaxed in order to investigate their combined impact on the predicted response of the system. Estimates of the kinetic parameters determined by EIS for the deposition of the single metals reveals that the first step of Co(II) reduction is much faaster tha the corresponding step of Ni(II) reduction.

Some limitations of the EIS technique (i.e. analysis at high overpotentials) are exposed and compared in the case of the nickel deposition using linear sweep voltammetry (LSV). Likewise, physicochemical models accounting for most of the important phenomena are derived and fitted to experimental data.

Ni-Co alloy formation is analyzed using LSV and steady state polarization experiments for different pH, current density and electrolyte composition. Current efficiencies for metal depsoition and alloy composition are also evaluated. To date, no experimental study considering all these variables has been reported in the literature. Then a steady state model is presented to describe the electrode response during alloy formation and used to provide insight into the anomalous behavior of this system. This model is based on information obtained from previous studies reported in the literature and from the current research. After being fitted to the experimental data, the model reveals that the anomalous behavior observed for this alloy is likely caused by the much faster charge-transfer of Co(II) reduction than that of Ni(II) reduction and not by other previously proposed mechanisms such as competition between adsorbed species for surface sites, formation of aqueous hydroxides ($MeOH^+$) or mixed intermediate species ($NiCo(III)_{ads}$) on the surface of the electrode.

Acknowledgements

I would like to thank my supervisor, Prof. Mark Pritzker, for all his guidance, support and friendship during the course of this thesis. It has been a pleasure and honor to have worked with you and learn so many things.

Also, I want to recognize the valuable comments from the committee members of the final examination: Professors Jacek Lipkowski (University of Guelph), David Harrington (University of Victoria), Michael Fowler and Ting Sui. Their comments and questions have improved the discussion presented in this thesis. Likewise, I am indebted to the Mexican Council of Science and Technology (CONACyT) for the scholarship granted to carry out my graduate studies and to the Natural Sciences and Engineering Research Council of Canada (NSERC) for financial support of the project.

I want to express my gratitude to my family and parents, specially my mother Carmen, for her unconditional love and teaching. Your dedication has given results, Thanks mom!. To my father Jorge who has always been an example to follow. To my beloved wife Fabiola, for spending this last year of my studies with me, sharing good times and being supportive and lovely.

Finally, I would like to thank my Mexican and Canadian friends witgh who I spent so many great moments at the Grad House, playing soccer, volleyball or talking about any subject. Thanks guys, this thesis includes parts of you.

To my parents

Fabiola, and

M. and A. Vazquez

Table of Contents

List of Tables

List of Figures

Nomenclature

Acronyms

CCE	Cathode current efficiency
CPE	Constant phase element
dc	Direct current
EDL	Electrical double layer
EIS	Electrochemical impedance spectroscopy
HER	Hydrogen evolution reaction
ICP	Inductively coupled plasma emission spectrometry
LSV	Linear sweep voltammetry
OCP	Open circuit potential (V)
RDE	Rotating disc electrode
rpm	Revolutions per minute
SEM	Scanning electron microscopy

Constants, Parameters and Variables

A	Area of the electrode (m^2)
$\bar{a}$	Dependent variable *a* under steady-state conditions
$\tilde{a}$	Phasor of dependent variable *a*
$B(OH)_3$	Boric acid
$B(OH)_4^-$	Mono-borate
$B_3O_3(OH)_4^-$	Tri-borate
$B_4O_5(OH)_4^{2-}$	Tetra-borate
C_j	Concentration of species j (mol m^{-3})
C_{dl}	Double layer capacity (F m^{-2})
$\overline{C}_j$	Steady state concentration of species *j* (mol m^{-3})
C_j^b	Bulk concentration of species *j* (mol m^{-3})
C_j^s	Surface concentration of species *j* (mol m^{-3})
Co	Cobalt

Co(II)	Any dissolved species containing cobalt in the +2 oxidation state
Co^{2+}	Cobaltous ion
$Co(OH)_{2(s)}$	Cobalt hydroxide
$CoSO_4$	Cobalt sulphate
$CoSO_{4(aq)}$	Dissolved cobalt(II) sulphate ion-pair
Cu	Copper
D_i	Diffusion coefficient of species *i* ($m^2\ s^{-1}$)
E	Applied or measured electrode potential (V)
$\overline{E}$	Constant *dc* potential (V)
$\tilde{E}$	Phasor of the potential (V)
E'	Electrode potential corrected for the ohmic drop (V)
E_{eq}	Equilibrium electrode potential (V)
E_0	Amplitude of sinusoidal voltage waveform (V)
e^-	Electron
F	Faraday constant (96485.5 C mol^{-1})
f	Frequency (Hz)
H^+	Proton
H_2	Hydrogen molecule
H_{ads}	Adsorbed H atom intermediate
I	Current (A)
I_f	Faradaic current (A)
I_{DL}	Capacitive current due to double layer charging effects (A)
I_0	Amplitude of sinusoidal current waveform (A)
i_A	Current density for the simultaneous catalysis of cobalt deposition and inhibition of nickel deposition (A m^{-2})
i_c	Capacitive component of the current density (A m^{-2})
i_f	Overall faradaic current density (A m^{-2})
i_j	Faradaic current density for the reduction of species *j* (A m^{-2})
i_L	Limiting current density (A m^{-2})
i_T	Total measured or applied current density (A m^{-2})
j	Imaginary unit $\sqrt{-1}$

k_{0ji}	rate constant of j^{th} step of reduction of metallic ion i (m s^{-1} or mol m^{-2} s^{-1})
k_{2H}	rate constant of the 2nd step of H^+ reduction (mol m^{-2} s^{-1})
m(t)	Mass of coating formed over t seconds of deposition
Me^{2+}	Metal ion in solution
Me(II)	Any dissolved species containing metal Me in the +2 oxidation state
$Me(I)_{ads}$	Adsorbed Me(I) intermediate
Me^0	Elemental metal Me
$MeOH_{ads}$	Adsorbed MeOH intermediate
n	Number of electrons transferred in electrochemical reaction
Na_2SO_4	Sodium sulphate
Ni(II)	Any dissolved species containing Ni in the +2 oxidation state
Ni	Nickel
$NiSO_4$	Nickel sulphate
$NiSO_{4(aq)}$	Dissolved nickel(II) sulphate ion-pair
$Ni(I)_{ads}$	Adsorbed Ni(I) intermediate
$NiCo(III)_{ads}$	Adsorbed mixed species containing Ni and Co in the +3 oxidation state
N_j	1-dimensional diffusive and convective flux (mol m^{-2} s^{-1})
P_x	Mass fraction of metal x
Q	Constant phase element coefficient (s^{α} Ω^{-1} m^{-2})
Q_x	Electrochemical equivalent of metal x (g C^{-1})
R	Molar gas constant (8.314 J mol^{-1} K^{-1})
R_s	Solution resistance (Ω m^2)
R_t	Charge transfer resistance (Ω m^2)
r_{ji}	Forward rate of j^{th} step of reduction of metallic ion i (mol m^{-2} s^{-1})
Sc	Schmidt number υ / D_i
T	Temperature (K)
t	Time (s)
v_y	Fluid velocity to a RDE in y-direction (m s^{-1})
wt. %	Weight percentage
y	Spatial variable (m or μm)

Z	Global impedance ($\Omega\ m^2$)
Z'	Real component of the impedance ($\Omega\ m^2$)
Z''	Imaginary component of the impedance ($\Omega\ m^2$)
$\lvert Z \rvert$	Magnitude of the impedance $(\Omega\ m^2)^{0.5}$

Greek Letters

α	Constant phase element exponent
α_{jx}	Charge transfer coefficient for species *j* in reaction step *x*
Δx	Sinuosoidal amplitude of variable *x*
β	Equilibrium constant ($mol\ m^3$, $mol^{-2}\ m^{-6}$ or dimensionless)
β_{H2O}	Equilibrium constant for water dissociation ($mol^{-2}\ m^{-6}$)
β_{3B}	Equilibrium constant for tri-borate dissociation ($mol\ m^3$)
β_H	Charge transfer coefficient for proton reduction
β_W	Charge transfer coefficient for water reduction
ν	Kinematic viscosity ($m^2\ s^{-1}$)
η	Overpotential (V)
δ	Boundary layer thickness (m)
θ	Phase angle (^{o})
θ_i	Fractional coverage of species *i* adsorbed on electrode surface
Γ_i	Adsorption density of species *i* required to completely fill a monolayer on electrode surface ($mol\ m^{-2}$)
τ	Duration of polarization during chronoamperometry experiments (s)
ω	Angular frequency $2\pi f$ (s^{-1})
Ω	Rotational speed of working electrode 2π(rpm)/60 (s^{-1})

Chapter 1 Introduction and Background

1.1 Alloys

In nature, metals generally are found in association with other elements. Chemical and/or physical processes are required to separate the various components and obtain metals in the pure state. The processes involved can be complex and depend on most cases on the concentration, nature of the associated elements and many other factors. Although metals in their pure state are often desired, the desired properties or combination of properties often cannot be satisfactorily achieved with a single metal. In these situations, the desired properties can be attained by the formation of alloys of these metals with others (or metalloids). An "alloy" is defined as a substance that has metallic properties and is composed of two or more chemical elements of which at least one is a metal [1].

As in the case of single metals, important uses of alloys are for decorative and protective purposes. These two categories comprise the largest number of applications for alloys. For example, iron (steels, ferroalloys, cast iron, etc) and copper (brass, bronze, etc), the two most commonly alloyed metals, fall into these categories. Other alloys involve different metals and are used for other purposes such as magnetic devices, corrosion resistance, catalysis, etc.

A widely cited and general classification of alloys was developed by Brenner who distinguished between homogeneous and heterogeneous systems [2]. In this classification, the types of alloys are summarized as follows:

I. One-phase alloys (homogeneous)

a) Solid solution (solid-state solution of one or more solutes in a solvent). Such a mixture is considered a solution rather than a compound when the crystal structure of the solvent remains unchanged by addition of the solutes and when the mixture remains a single homogeneous phase.

b) Intermetallic compound

II. Two-phase alloys (heterogeneous)

These are mixtures consisting of two of the following phases:

a) Solid solution

b) Intermetallic compound

c) “Virtually” unalloyed elements (metals which are usually considered insoluble in each other)

The phases of a heterogeneous alloy may be of the same or different types; for example, they may be a mixture of two solid solutions or a mixture of a solid solution and a virtually unalloyed metal. Under II(c), the limiting word “virtually” is used because metals which are usually considered insoluble in each other (e.g., lead and copper) are often in reality not pure when they separate out from a melt. Each metal contains a small proportion of the other in solid solution, in some cases only hundredths of a per cent. Therefore, II(c) is a limiting case of II(a) [2].

Some commercial alloys are homogeneous, while others are heterogeneous. The latter type is probably the more common. Familiar alloys, such as sterling silver and ordinary solder, in the annealed state are largely intimate mixtures of virtually unalloyed metals. It is rather surprising that pairs of metals which are closely related chemically, such as copper and silver, lead and tin or zinc and cadmium, have very little mutual solid miscibility [2]. Another such example is the nickel-cobalt system, where both of these metals exhibit similar chemical, but rather different magnetic properties [3]. Due to this last factor and their superior permanent magnetic properties in comparison to that of ferroalloys [4], Ni-Co alloys have received considerable attention especially in microsystem technology for the manufacture of sensors, magnetic devices, microrelays, inductors, actuators, memory devices and hard drives [5-8].

In the electrocatalysis field, it is known that both Ni and Co show interesting activity for the reduction of certain ions and molecules. Alloys of this type can be prepared as catalysts for the hydrogen evolution reaction (HER). This catalytic activity has been linked with the abilities of these materials to absorb a large amount of hydrogen and to store it in the amorphous layers that comprise the alloy [9-11]. Ni-Co alloys have also been used for the electrocatalysis of the oxygen evolution reaction. Their use in this regard has been accelerated due to the role of oxygen evolution in a number of important applications at low and moderate temperature: hydrogen production in water electrolysis, metal electrowinning, energy storage in metal-air batteries and anodic organic synthesis [12-14].

However, it is in the corrosion field where Ni-Co alloys have gained particular popularity in recent years due to their combined properties of extraordinary hardness and high corrosion resistance (greater than Ni-Fe films). This makes them a potential replacement for hard chromium which is a more toxic material [15, 16]. Other applications as a protective

material include their use in medical instruments, energy generation processes, aerospace devices and various environments where materials have to withstand high temperatures and oxidizing conditions [15, 17, 18].

1.2 Research Motivation

Nowadays, the development of novel materials involves diverse branches of science as a consequence of the new requirements imposed by modern society. This includes aspects ranging from the optimization of the manufacturing processes to the durability of the materials themselves. Since the durability of a material is directly related to its hardness and corrosion resistance, these properties are also important considerations when designing and assessing processes for the production of new materials. Ideally, some synergism should exist between the durability and the other properties of interest in the material. Electrochemical processes are no exceptions to this trend and so new processes have been developed in recent years, particularly those involving the fabrication of coatings. The materials fabricated by this technology exhibit excellent characteristics such as refined grain structure, smoothness, low residual stress without co-deposition of sulphur, low coercivity, etc. [18-23]. Moreover, electroplating has several advantages over physical methods of deposition: capability of high volume production, low cost and the ability to coat thin layers on non-planar substrates [22].

Alloys are one of the materials that can be produced by this technique with a number of advantages over other methods. An example are the Ni-Co alloys [3, 21, 22], which have lately received interest for microfabrication due to the magnetic properties of cobalt and the corrosion and wear resistance of nickel [21]. Moreover, this interest has been further stimulated by use in magnetoresistive recording read-heads and sensors [24]. However, one of the biggest problems associated with the electrodeposition of Ni-Co alloys is the anomalous behavior of the formation of these alloys whereby cobalt is preferentially deposited over nickel under almost any condition, even when the Ni(II) concentration is higher in the bulk solution. This problem has complicated the prediction and control of the metal composition in the alloys during their production and as a consequence the ability to obtain the desirable properties associated with high nickel contents. Although this problem is not recent, the studies that have been carried out so far to analyze this system have not always been as comprehensive as they could be in terms of the experimental conditions investigated or the reaction mechanisms and mathematical models developed to describe its

behavior. Of course, regardless how thorough and detailed any model is, its derivation inevitably involves some assumptions that hopefully can be assessed by comparison with experimental data. Nevertheless, it is expected that the more comprehensive a model is, the more insight and better explanations it can provide regarding the behavior of a given system. To date, most of the studies have dealt with experimental conditions whereby the different microscopic phenomena and conditions occurring during the alloy co-deposition have not been completely disclosed. Although several studies have concerned with modeling aspects [42, 88, 89], the operating conditions (e.g. current density, pH, and electrolyte composition) that yield the desired alloy properties of the Ni-Co alloys are still empirically determined.

This provides a motivation to use a variety of electrochemical techniques to comprehensively study the reaction mechanism involved in the formation of Ni-Co alloys under different experimental conditions in a typical acidic buffered sulphate plating bath. The impact of the experimental conditions during dc electrolysis on such quantities as the alloy composition and current efficiency of metal deposition will also be studied. Since the analysis of the formation of this alloy must draw upon knowledge of the behavior of the electrodeposition of nickel and cobalt alone in similar solutions, this thesis will also focus on the single metal deposition of nickel and cobalt. Considerable attention will be focused on developing phenomenological models for the electrode response of both the single metal and alloy systems and then quantitatively fitting these models to experimental data obtained by a variety of techniques.

1.3 Research Objectives

Since the various reaction steps and phenomena involved in the electrodeposition of single metals and alloys are often highly coupled and occur over a wide range of time scales, direct current techniques are not always effective for identification of the steps and quantitative analysis of the dynamics involved. Electrochemical impedance spectroscopy (EIS) has been shown in recent years to be a robust and powerful technique for the quantitative characterization of the various relaxation phenomena occurring during the electrodeposition of metals: transport, adsorption, multi-step charge transfer, etc [24]. The relaxation of these phenomena gives rise to either inductive or capacitive loops in EIS spectra, characterized by *distributed time constants*. The methods for determining the distributed time constants are generally not straightforward. The most direct approach is to interpret the EIS spectra on the

basis of physicochemical models that account for kinetics and mass transport effects [25]. However, the disadvantage of this approach is that the required mathematical analysis can be quite complicated. As a consequence, very few studies on the use of EIS have been reported to investigate the nickel and cobalt electrodeposition [24, 38, 44, 45, 47]. Thus, the use of EIS in this project will significantly contribute not only to a better understanding of the deposition of these metals, but also to extending the general use of this experimental technique to more complex systems.

Given the complex nature of the formation of Ni-Co alloys, this study was carried out in two stages in order to achieve the final goals. Hence, the main objectives of this work are two-fold:

a) Investigation of the mechanism for single metal electrodeposition of nickel and cobalt on nickel and cobalt substrates, respectively.

I. The initial experiments involved the use of direct current techniques on a rotating disc working electrode (RDE); the main purpose is to qualitatively assess the system and determine the range of potentials to be used in subsequent experiments. The first technique used is *linear sweep voltammetry* (refer to section 3.2), followed by *chronoamperometry* (see also section 3.4). This latter technique involves the application of a constant electrode potential to the working electrode to enable the desired reaction to occur. The response to this input is a current-time transient plot obtained under well-stirred conditions through the use of the RDE. The resulting currents measured at some fixed time (τ) are plotted versus the potential to yield *sampled-current voltammograms* (also called *steady-state polarization curves*).

   Once the direct current experiments are completed, *electrochemical impedance spectroscopy* (refer to section 3.5) is performed employing the same RDE. This transient method can drive phenomena with relaxation times that vary over a wide range of scales (distributed time constants), making it one of the most powerful analytical tools for both faradaic (charge transfer involved) and non-faradaic processes (no charge transfer involved).

II. A 1-dimensional physicochemical model is then developed for single nickel/cobalt deposition on a RDE that incorporates the effects of mass transport, electrode kinetics and homogeneous reactions. The mass transport accounts for diffusion and

convection, while the electrode kinetics includes that of hydrogen evolution (HER) in addition to metal deposition. The models are derived for both steady-state and transient conditions. An impedance model is obtained from the transient equations by linearization of the various kinetic and mass transport equations.

III. These models are subsequently fitted to the experimental data (EIS and the current-potential curves) to estimate the kinetic parameters for deposition of the single metals.

b) Investigation of the mechanism for Ni-Co alloy electrodeposition on copper substrates.

I. The effect of different Ni(II)/Co(II) concentration ratios on the electrode response during alloy deposition is analyzed in order to study the reaction mechanism under different experimental conditions. In particular, the effects of pH, boric acid concentration, metal concentration will be investigated.

II. A steady-state mechanism for Ni-Co alloy deposition is then proposed and derived based on the previous experiments and the analysis of single nickel and cobalt deposition.

III. Kinetic parameters for Ni-Co co-deposition are obtained by fitting the model for alloy deposition to the experimental data and compared with those for single metal deposition.

1.4 Structure of the Thesis

This thesis is comprised of nine chapters. Chapter 2 provides background on the theory of alloy electrodeposition, highlighting aspects of the Ni-Co system. Chapter 3 reviews details of the electrochemical techniques (LSV, EIS, etc.) used in this research. Chapter 4 describes the experimental conditions, equipment, reagents, materials and procedures that are used and followed during this research. Chapter 5 is concerned with the single metal deposition of cobalt in buffered sulphate solutions. Included in this chapter are thermodynamic calculations of the solution chemistry involved in this system, experimental LSV and EIS data, development of the steady state and impedance models for this system, discussion of the

fitting of these models to the experimental data, a sensitivity analysis of the model to the various fitted parameters and simulations of the model using the best-fit parameters to gain further insight into cobalt electrodeposition. A similar analysis on single metal deposition of nickel is presented in Chapter 6. Chapter 7 describes an extension of the analysis of the single metal deposition of nickel to conditions of higher overpotential than that covered in Chapter 6 as well as the development of a transient model that is subsequently fit to experimental LSV curves. Chapter 8 describes a comprehensive LSV study to investigate the sequence of reactions that occur during Ni-Co alloy electrodeposition under different conditions of pH, current and electrolyte composition. Finally, a steady-state model for Ni-Co alloy deposition in sulphate media at different $NiSO_4/CoSO_4$ concentration ratios is presented and fit to experimental data in Chapter 9. A summary of the contributions of this work and directions for future research are presented in Chapter 10.

Chapter 2 Alloy Electrodeposition

At the present time, alloys find very wide use since their properties are often superior to those of pure metals. This has motivated the development of still more novel alloys to meet the demands of industry.

Currently, the use of electrochemical methods to produce metal and alloy products has gained considerable interest due to their low cost, flexibility and efficiency in contrast with other methods. As a consequence, many such processes are economically feasible and have become commercially established. Electrochemical processes find a wide variety of industrial applications for the surface treatment of metals and alloys. They include i) cathodic processes such as electroplating and degreasing by hydrogen evolution, ii) anodic processes such as anodization, electropolishing and electrochemical machining and iii) processes proceeding without the application of an external current such as electroless plating, phosphating, chromating and chemical polishing [26].

Among them, electroplating or electrodeposition which involves the electrolytic deposition of a coating is perhaps the most widely used electrochemical surface treatment process. Its purpose is generally to alter the characteristics of a surface so as to provide improved appearance, ability to withstand corrosion, resistance to abrasion or other desired properties or a combination of them, although occasionally it is used simply to alter its dimensions [27].

Metals, alloys and metal matrix composites can be deposited as single layer or multi-layer coatings. In some cases, the electrochemical deposition of certain metals (e.g., W, Mo, Ti) which is not possible in aqueous solutions when they are pure can be induced when they are co-deposited with other metals. Examples are the alloys W-Fe, W-Ni, W-Co, Mo-Ni, Ti-Fe, etc. [28]. As mentioned previously, a particularly attractive aspect of alloy plating is that it can yield materials with properties not attainable by electrodeposition of single metals. Alloy coatings have been shown to be denser and harder, more corrosion and wear resistant, more protective of underlying substrates, have superior magnetic and antifriction properties, etc. [27]. Since electrodeposition of alloys is governed by many of the same variables and parameters as that of single metals, progress in both types of plating has depended on similar advances, which have been considerable in the last few decades [27].

2.1 Principles of the deposition process

2.1.1 Metal deposition mechanism

When immersed in an aqueous solution, an electrode (substrate) normally carries an electric charge and attracts water molecules, which are dipoles, as well as ions carrying charges of the opposite sign. Water molecules may be held by adsorption forces which are often quite strong. Ions are held near the metal surface by electrostatic attraction, forming an electrical *double layer* with a measurable capacitance. When an electrode is polarized cathodically, metal ions from the solution may reach the surface, be reduced, eventually find their way to stable positions in the metal lattice and release their ligands, with the result that their overall charge is neutralized. This process constitutes a spontaneous flow of cathodic current (faradaic current). When an electrode is sufficiently polarized anodically, atoms may become sufficiently loosened from the metal lattice forces to coordinate with some of the adsorbed water molecules, move to the solution side of the double layer as hydrated ions, and then diffuse into the solution. This outward movement of positive charge constitutes an anodic or dissolution current [27].

When the electrode is at its equilibrium state, the anodic and cathodic processes at this electrode occur at the same rate and so no net current is measured. The partial current for the anodic or cathodic process under these conditions is called the exchange current. The exchange current is a measure of the speed of the electrode kinetics and can vary over a wide range. For example, the reduction of Sn^{2+} and Pb^{2+} has very fast kinetics and so has a very high exchange current; if the electrode is an amalgam, the exchange current density may exceed 2000 A m^{-2} [28]. The exchange currents for the reduction of Cu^{2+} and Zn^{2+} in acidic solutions are more moderate at about 0.2 A m^{-2}. On the other hand, the reduction of Ni^{2+} is much slower and has an exchange current density of about 2×10^{-5} A m^{-2} [29]. As might be expected, the relative magnitudes of these exchange currents are similar to the relative rates at which their respective ions undergo ordinary chemical reactions involving exchange of coordination ligands and water molecules to become complexed [30] since electrode reactions involve the exchange of anionic and cationic ligands with metallic coordination bonds. The presence of adsorbed impurities or addition agents sharply decreases the exchange currents because these substances tend to preferentially and more strongly bond to the substrate than water ligands. In the case of the metal ion reduction, energy expended to strip the ligand water molecules from the metal ion is counteracted by the energy released as

the ion finds its place in the metal lattice. The relative magnitudes of these two energies determine the reaction potential [27].

Metal atoms are not deposited as continuous sheets from one edge of the cathode to the other. Metal ions become attached to the cathode at certain favored sites, losing some of the previously attached water or other ligands, in order to form bonds with the cathode surface and partially neutralize their charge [31]. In this state, these ions are referred to as adions. These adions diffuse over the surface to kinks, edges, steps or other irregularities where they may become incorporated into the metal lattice. As these growth sites travel across the crystal face, monoatomic layers bounded by microsteps are produced and grow until they encounter adsorbed impurities and join to form multilayer growth stacks and macrosteps. Lateral growth proceeds from various centers until neighboring lattices meet to form a boundary at the lines of contact. Symmetrical crystal faces are not developed; accordingly the individual structures are called grains. Continued growth must proceed outward [27, 28].

Metal reduction from complex salt solutions (i.e., contain chemical groups or ligands other than water that tend to form aqueous complexes with the metal) often yields very poor deposits. In many instances, reduction occurs directly from complexed ions and transformation to the simple ion is seldom observed before deposition. No fundamental difference exists between plating from simple or complex ions, but the effects of the adsorption of free ligands on the cathode surface and increased concentration polarization are often significant [27].

2.1.2 Polarization

A potential difference must be applied across a normal cell (cathode and anode) to produce a current. The application of this potential is called *polarization*. At each electrode of an unpolarized cell, cathodic and anodic reactions must proceed at equal rates so that no net current flows. Application of the polarizing potential lowers the potential at the cathode, thereby accelerating the cathodic direction and retarding the anodic direction of the half-cell reaction occurring there. This leads to a net cathodic current and corresponding deposition of metal. At the anode, the potential is raised with the opposite consequences. The shift in potential at each electrode with respect to the equilibrium potential of the half-cell reaction that is occurring is its polarization overvoltage η. It is negative for a cathodic reaction and

positive for an anodic reaction [31]. Three factors contribute to the total overvoltage in an operating cell: electrode kinetics (activation), mass transfer limitations (concentration) and nucleation.

2.1.3 Mass transport in deposition processes

Three processes operate to supply metal ions to the depleted solution at the cathode and to remove them from the enriched solution at the anode. In the following discussion, only the cathode is considered, but analogous processes occur at the anode.

When a potential drop is applied across the electrodes, an electric field is established in the bath. Responding to this field, cations move by a process termed migration toward the cathode on account of their positive charge, while anions move away from it. The total flux of ions through the solution occurs by the combination of diffusion, convection and migration.

Convection is a form of mass transport characterized by movement of substantial quantities of the solution relative to the electrode. Either the solution or electrode, or both, may move. Near the cathode, the solution becomes less dense as metal ions are plated out; this causes upward streaming of electrolyte when the electrode is placed at the upper part of the cell. Conversely, downward streaming occurs at the anode. This movement of solution due to density differences is called natural convection and may result in stratification (a dense layer lying below less dense fluid) of the plating bath, with layers of high density accumulating near the bottom of the tank [27]. In the experiments of this study, a rotating disk electrode set-up is used and so forced convection is dominant over natural convection. The use of a rotating disk electrode is discussed in section 3.3.

Diffusion refers to the movement of ions or neutral molecules through the solution in response to a concentration gradient. It is a consequence of random molecular motion, which operates to produce a more uniform distribution of each species throughout a solution. Both diffusion and convection become particularly important in the region close to an electrode where species become depleted or accumulate due to the electrode reactions and electric field effects. This region near the electrode where the concentration of an ionic or molecular species differs from its bulk concentration is called the diffusion layer.

2.2 Alloy plating

As noted previously, the original progress in alloy deposition depended on many of the same advances as did single metal deposition: purity of commercial chemicals, commercially available electric power and reliable conversion equipment to supply direct current, instrumentation and changes from the practice of an "art" to one of technology.

Properties superior to those possible with single metal electroplates are reported in the literature for alloys. It is well recognized that alloy deposition provides properties not attainable by electrodeposition of single metals. As mentioned earlier, alloy coatings are often sought due to their superiority with regard to the following properties: density, hardness, corrosion resistance in certain composition ranges, substrate protection, toughness, strength, wear resistance, magnetic properties, lubricity and suitability for subsequent electroplate overlayers and conversion chemical treatments [2, 27].

2.2.1 Constituents of plating baths and their functions

In general, constituents are added to alloy plating baths for different purposes [27]: (1) primary salts which provide the primary ions, (2) secondary salts which influence the dissociation of the primary ion sources by mass action effects, (3) addition agents which affect the structure of the deposit or nature of deposition, (4) buffer compounds, (5) conductivity salts and (6) salts promoting anode solubility.

***Primary and secondary salts*.** The primary salts are largely responsible for the ionic activities of the depositing metals since they determine the concentration and charge of the ions. Secondary salts contain non-depositing metals with or without an anion common to the primary salt. These salts are added to improve solution conductivity and influence the pH, ionic strength and ionic mobilities in the cathode film. $CoSO_4$, $NiSO_4$ are primary salts, whereas Na_2SO_4 and H_2SO_4 are secondary salts.

***Addition agents and buffer compounds*.** In many cases, no clear distinction can be made between bath constituents acting as addition agents or buffers since many substances act in both capacities. Their main function is to help produce high quality deposits which otherwise could be powdery, brittle or irregularly cover the substrate, for example. Addition agents can be colloidal in nature or can be truly dissolved. The addition agent may act in one of many

ways: altering the limiting current density of one or both metals (generally is determined by the more noble metal), changing the polarization characteristics during co-deposition or increasing the current efficiency at the anode or cathode or both as a result of a change in the reaction mechanism [27]. In some cases, two or more additive agents can be added together to produce a desired effect which cannot be achieved by each one separately. PEG and Thiourea are examples of addition agents. Boric acid is a buffer compound.

An addition agent can also influence the plate composition [32] if it forms complex ions with one or both metals. Addition agents effective in single-metal plating baths are also likely to be effective in alloy plating baths of the same type. In cases of alloy plating where the composition is dominated by a single metal, one can often think of the secondary metals as acting as addition agents influencing the structure and properties of the main component.

2.2.2 Influence of the common variables in alloy plating

The independent variables current density, agitation, temperature, pH and plating bath composition influence the ratio in which the metals co-deposit, the physical characteristics of the coatings and the rate of deposition. An appreciable change in any one of these variables may require a substantial and compensating effect by another variable or combination of them in order to maintain the deposit composition at a particular value. No single variable has a unique and independent effect on the deposit composition or physical properties although each variable often has certain general effects. Thus, the composition of an electrodeposited alloy is usually determined by a combination of inter-related variables, the main ones of which are as follows [2]:

A. Variables of bath composition

1. concentrations of depositing metals
    a. ratio of the concentrations of the depositing metals
    b. combined concentration of the depositing metals
2. concentration of complexing agents
3. pH
4. presence of addition agents
5. presence of indifferent electrolytes or conducting salts

B. Variables of plating operation

1. current density
2. temperature
3. extent of agitation of bath or movement of cathode

C. Miscellaneous variables

1. cathode current efficiency
2. cathode shape
3. metal substrate
4. deposit thickness
5. mode of electrolysis (see Chapter 4)

Since some of these variables are self-explanatory, only the most important ones are discussed below.

***Current density*.** The effect of the current density may be examined from two view points: diffusion control and the cathode potential [2]. According to simple diffusion theory, the rate of deposition of a metal has an upper limit which is determined by the rate at which its ions can move through the cathode diffusion layer. If the two metal ions being deposited have the same concentration, the rate of deposition of the more noble metal at a given current density is much closer to its limiting value than that of the less noble metal. A further increase of current density (and more negative potential) will therefore affect the rate of deposition of the less noble metal to a greater extent than that of the more noble component and lead to a higher content of the less noble metal in the alloy. The magnitude of the change in alloy composition resulting from a variation of current density is rather large for the regular type codeposits and smaller for the other types. However, no general rule can be given since the effects depend on specific properties of each alloy plating system. With regard to the cathode potential, an increase of the current makes the potential in the cathode to become more negative (less noble), whereby the electrodeposition conditions approach more to those related to the current-potential curve of the less noble metal. Thus, this should increase the composition of the less noble metal in the alloy [2].

Since addition agents influence the physical properties of deposits, the maximum operating current densities can be altered by using the appropriate addition agents. Agitation, temperature, pH and other factors also influence the effect of current density. If addition

agents are used, their influence on the deposit composition must be considered when judging current density effects [27].

pH. The effects of pH on the composition of an electrochemical alloy are specific and usually unpredictable. In some baths, the pH has a large effect (e.g. HER occurring along with deposition), while in others it has only a small effect on the composition of the deposit. Apart from the obvious situations where the HER occurs, the importance of pH depends on the chemical nature of the metal-containing ions through its effect on metal solution chemistry of the depositing metal. Under conditions where bare metal cations are most stable, the system is less sensitive to variations in the pH of the solution; this is indicated by a slight variation in the thermodynamic activity of the ions. Thus, one might lower the pH to very acidic conditions (e.g., ≈ 1 000 mol m^{-3}) to ensure ohmic losses in the bulk solution are low. On the other hand, the composition and stability of many complexes (in both alkaline and acid solutions) depend strongly on pH. For example, metal complexes such as stannate, zincate, cyanides and amines, are stable only in alkaline solution. As a general rule, variations of pH should have less effect on the composition of alloys deposited from baths containing the metals as simple ions and a larger effect on the composition of alloys deposited from baths in which the metals are present as complexes with large instability constants [2].

Indifferent salts. This category includes salts which do not contain the depositing metals, do not form complexes with the metals or act as addition agents, and as far as can be determined from their chemistry, should have no direct or specific effect on the composition or properties of the deposit. For example, sodium sulphate in a nickel plating bath is an example of an indifferent salt. Often, indifferent salts are added to a plating bath to increase its conductivity. They are also added because they are supposed to have, or have been found to possess, some positive influence on a deposit due to some poorly understood mechanism [2].

Current efficiency. It is very important to operate electrodeposition of metals at as high current efficiency as possible for economic reasons since it is a measure of the effective utilization of electrical energy. It is also a factor in determining the time required to produce a coating with desired thickness and hence its production.

The cathode current efficiency (CCE) for alloy deposition includes the total amount of deposited metal including all components being plated and cannot be calculated as is the

case for single metal deposition from knowledge of only the weight of deposit and the quantity of current. In addition, the composition of the resulting deposit must be known. The cathode current efficiency of alloy deposition can be determined from the sum of the cathode current efficiencies for deposition of the individual metals:

$$CCE = \frac{P_1\, m(t)}{Q_1\, I\, t} + \frac{P_2\, m(t)}{Q_2\, I\, t} \qquad (2.1)$$

where P_1 and P_2 are the mass fraction of the metals in a deposit, Q_1 and Q_2 are their respective electrochemical equivalents expressed in grams per coulomb and $m(t)$ is the mass of the deposit formed after t seconds of deposition. The current I is expressed in amperes.

Examples in which the co-deposition current efficiency exceeds that of the deposition of one or both metals when plated alone from the same bath in question have been reported [27]. When this occurs, the current efficiency depends on the alloy composition.

Chapter 3 Electrochemical Techniques

Electrode reactions are generally very complex with the possible involvement of adsorption, coupled chemical reactions, phase formation, etc. in addition to electron transfer. Numerous experimental techniques can be used to determine which steps are important in controlling the overall rate of a particular system [33]. Approximately 30 distinct techniques involving the perturbation of potential, current and charge have been used in the study of electrode processes. However, no more than 10 to 12 techniques have been commonly used partly because of the mathematical difficulty associated with relating the response for many of the methods proposed. A discussion of the more popular techniques can be found in refs. [31] and [33].

The electrochemical techniques generally are classified according to the type of perturbation imposed upon the system. Their uses depend greatly on: a) the speed of the reaction, b) the required information and accuracy and c) experimental factors such as solvent properties (conductance, viscosity), temperature, pressure and accessibility of the electrode for the application of ancillary techniques (e.g. ellipsometry). Another distinction that can be made between methods is whether they operate under steady state or transient conditions. The following sections discuss some general concepts related to the techniques used in this study and provide some background to the techniques themselves.

3.1 Faradaic and non-faradaic processes

Two types of processes occur at electrodes. One kind involves reactions in which electrons are transferred across the metal-solution interface. This causes reduction or oxidation to occur via processes that are termed “faradaic”. Under certain conditions, the same interface will exhibit a range of potentials where no charge-transfer reactions occur because they are thermodynamically or kinetically unfavorable. However, whenever the potential (or solution composition) is changed, an additional current attributed to non-faradaic processes flows whether or not a faradaic process occurs. Although faradaic processes are usually of primary interest, the current due to non-faradaic processes must be taken into account in models to obtain information regarding charge transfer and associated reactions.

These non-faradaic processes are mostly associated with the electrical double layer at the electrode-solution interface. The inner layer closest to the electrode is made up of solvent molecules and specifically adsorbing species. A more loosely structured region containing the solvent and solvated ions form the next layer. The interaction of these ions with the charged electrode involves only long-range electrostatic forces and so is essentially independent of the chemical properties of the ions and electrode, i.e., non-specific [31, 34, 35]. The existence of the double layer has consequences on the electrode response regardless whether a non-faradaic or a faradaic process is occurring. Whenever the potential (charge) of an electrode changes, this causes the double layer to adjust by changing its distribution of ions, dipoles and solvent molecules. This flow of charged species to and from the interface constitutes a non-faradaic current often referred to as the charging current. Since the electrical potential at the plane where electron transfer occurs influences the concentration of charged species, the double layer affects faradaic processes by acting as a capacitor in parallel with the electron transfer reactions. The total current passing through the electrode is split between a portion for the electron transfer reactions and a portion to charge the double layer capacitor. This reduces the amount of current that can be used for the faradaic reactions [31, 33, 35]. Since the double layer has a greater effect on electrode kinetics when the ionic concentration is low, its influence can be reduced by operating with a high concentration of a supporting electrolyte [31, 33, 35].

Once the double layer has reorganized to the structure appropriate to the new potential, the charging current will decay to zero. Since this readjustment normally requires only a few milliseconds, the charging current is a transient effect that persists only over a very short timescale [31, 33, 35]. It depends on the concentration of electrolyte (inert electrolyte + reactant) and the electrode potential.

On the basis of the previous considerations, the total current at the electrode surface can be split between two contributions:

$$I = I_f + I_{DL} \qquad (3.1)$$

where I_f and I_{DL} are the faradaic and double layer charging currents, respectively. Kinetic analysis without correction for the existence of the double layer may be done in many situations.

3.2 Linear sweep voltammetry (LSV)

Voltammetry is a very popular technique which is particularly useful during the initial studies of a new system. Many experiments can be carried out within a few minutes. Moreover, the data are presented in a form which allows rapid, qualitative interpretation without recourse to detailed calculation. In this experiment, the current is recorded as a function of the potential [31, 33, 35]. Essentially, the potential is swept over the range where an electrode reaction occurs in order to gain a qualitative understanding of the sequence of electron transfer reactions that can occur. Potential sweep rates range from a few millivolts per hour to tens of volts per second. The slow sweep rates are frequently used to measure near steady-state current/voltage curves on the assumption that the electron transfer reactions relax rapidly enough that the system is negligibly different from its true steady state. On the other hand, very high sweep rates are frequently used to test for the existence of short-lived intermediates.

Since the electrode potential is always measured with respect to a reference electrode (ideally nonpolarizable so that its potential does not change upon passage of current), a portion of this potential is required to overcome ohmic resistance. Thus, the actual electrode potential available for electrochemical reactions is given by:

$$E' = E - iR_s \qquad (3.2)$$

where E' is the electrode potential corrected for the ohmic drop, E is the applied or measured electrode potential, i is the measured current density (I/A), and R_s is the solution resistance between the working and reference electrodes.

The departure of the electrode potential (or cell potential) from the equilibrium value for a given half-cell reaction upon passage of faradaic current is termed overpotential:

$$\eta = E' - E_{eq} \qquad (3.3)$$

where E_{eq} is the equilibrium potential given by the Nernst equation. Current-potential curves, particularly those obtained under steady-state conditions, are sometimes called polarization curves.

3.3 Rotating disk electrode (RDE)

The solution is often agitated under well controlled conditions during experiments. This is typically done to enhance the effects of mass transfer, allow steady-state to be attained more quickly or enable certain measurements (e.g., limiting current) to be made with high precision. Moreover, once steady-state is reached, double layer charging is no longer a factor in the measurements. The simplest mathematical treatment of convective systems is based on the diffusion layer concept. In this model, it is assumed that convection maintains the concentration of all species uniform and equal to bulk values beyond a certain distance from the electrode. Within this layer, no solution movement occurs and mass transfer occurs by diffusion [31, 33]. However, this model does not realistically describe mass transfer since convection close to the electrode is ignored.

A hydrodynamic method in which convection within the boundary layer can be treated more realistically involves the use of the rotating disk electrode (RDE). This is one of the few convective electrode systems for which the hydrodynamic equations and the convective-diffusion equation can be expressed and solved relatively easily. The RDE consists of a polished disk of the chosen electrode material embedded in an insulating sheath having a substantially larger diameter. The disk can be rotated (including its non-conducting sheath) at a desired constant velocity (rpm, revolutions per minute), although the most useful descriptor of rotation rate is the angular velocity Ω .

This technique is often coupled with LSV (section 3.2) using rotation speeds between 100 and 6000 rpm. The solution moves toward the electrode in a highly organized manner so that it may be considered to consist of a series of separate, non-mixing layer. This defines a boundary layer with thickness $\delta = 1.61 D_i^{1/3} \Omega^{-1/2} \upsilon^{1/6}$. From this, it is straightforward to derive an expression for the limiting current density i_L for a reaction when the surface concentration of the electroactive reacting species is zero and the electrode reaction is entirely controlled by mass transfer. Since the limiting current density is related to the flux of the reactant as follows:

$$i_L = -nFD_i \left(\frac{\partial C_i^b}{\partial x} \right)_{x=0} = -nFD_i \frac{C_i^b}{\delta} \qquad (3.3)$$

substitution of the expression above for δ leads to the well-known Levich equation:

$$i_L = 0.62\, nFD_i^{2/3} \upsilon^{-1/6} \Omega^{1/2} C_i \qquad (3.4)$$

where n is the number of electrons transferred in the reaction, F is the Faraday constant and υ is the kinematic viscosity of the electrolyte, while D_i and C_i are the diffusion coefficient and the concentration of the electroactive species i, respectively.

During RDE experiments, it is possible to identify three distinct ranges as the potential becomes negative for a reduction reaction [33]:

a) *Electron transfer control*. At electrode potentials not too negative with respect to the equilibrium potential of a half-cell reaction, the kinetics of this reaction is rate determining. In this potential range, the surface concentration of O (oxidized form of the metallic ion) will not deviate significantly from its bulk value.

b) *Mixed control*. As the overpotential is made more negative, the rate of electron transfer continues to increase exponentially and eventually the rate of reduction of O at the electrode will approach the rate of its transport to the surface. In this state, neither kinetics nor mass transfer of the electroactive species alone is rate determining. The electron transfer process is now fast enough that the surface concentration begins to decrease below the bulk value and mass transport now becomes one of the controlling factors for the rate of the reaction. The current density still continues to increase as the potential is made more negative, although at a continually slower rate.

c) *Mass transport control*. The continued rise in the kinetics of electron transfer as the overpotential increases ensures that it will become faster than mass transport and the surface concentration of O will eventually drop to zero. At this limiting condition, the current density becomes completely mass transport-controlled and no longer depends on the potential. The current rise levels off to a plateau or limiting value at this point defined by Eq. (3.4).

3.4 Chronoamperometry

In this technique, the change in current due to a step change in the electrode potential is monitored over time [31, 33, 35]. Usually, the potential is changed from a value where no current passes to one where the electrode reaction of interest takes place. It should be noted that potential step experiments are excellent for determining exact kinetic parameters when a mechanism is fully understood but much less suited to preliminary studies because the current-time transients for most systems usually look very similar to each other.

3.5 Electrochemical impedance spectroscopy (EIS)

EIS has become a very important technique for studying electrochemical systems because it allows phenomena operating on different time scales to be separated out by measuring the electrode response to a sinusoidally varying input signal (current or potential) as a function of frequency. In this way, the effects of various factors affecting the response that would normally be convoluted when measured as a function of time tend to be de-convoluted when measured as a function of frequency. EIS is suitable for studying both faradaic and non-faradaic processes. Moreover, it allows the study of systems with highly resistive nature or complex diffusional problems (e.g., solid ionics) that are inaccessible for other techniques (e.g., some *dc* techniques). Advances in electronic instrumentation have somewhat facilitated the development and popularity of the EIS technique. Consequently, the most complex aspect of the technique is the satisfactory analysis of the data in order to extract useful information rather than obtaining reliable data itself.

EIS is a non-stationary technique in which small-amplitude sinusoidal oscillations of voltage or current are applied to the system over a wide range of frequencies [25]. The response of the system is described in terms of two quantities: the ratio of amplitudes of the perturbation and response signals which yields the impedance and the phase difference between the signals which defines the phase angle of the impedance vector. For instance, if a sinusoidal voltage $E = E_0 \sin \omega t$ is applied (where E_0 is the amplitude, $\omega = 2\pi f$ is the angular frequency, f is the frequency and t the time), a sinusoidal current $I = I_0 \sin(\omega t + \theta)$ is obtained as the response, with I_0 being its amplitude and θ the difference in phase with respect to the input E. The magnitude of the impedance is then expressed as $|Z| = E_0 / I_0$ and its phase angle is θ.

Currently, there are two approaches to analyze the data in EIS spectra for electrochemical systems. One is based on physicochemical models for the system in question, while the second approach makes use of equivalent electrical circuit analogs to describe the frequency response. The first one is adopted in this research since the model used directly describes the actual physicochemical phenomena that occur during the electrochemical process and the model parameters (e.g., rate constants, transfer coefficients) obtained by fitting the model to the data are directly related to these phenomena.

The EIS data obtained can be represented in several different types of impedance diagrams that differ according to the required information and the field of application [25]. In electrochemical systems, the two common types of plots that have been employed are the Nyquist and Bode diagrams. These diagrams make use of the vectorial nature of the impedance which can be manipulated as a complex number with real and imaginary components, as well as being described by a modulus and phase angle [25]:

$$\bar{Z} = Z' + jZ'' = |Z|(\cos\theta + j\sin\theta) \qquad (3.5)$$

Nyquist diagram – In this diagram, impedance data are plotted on the complex plane, with its real component (Z') along the x-axis and the negative of imaginary component (Z'') along the y-axis. Consequently, a global view of the behavior of the system is displayed, allowing the various phenomena (ie. resistance, capacitance, and inductance) associated with it and the predominant circuit elements in a particular region of the spectrum to be distinguished. Some resistive elements and their magnitudes can be roughly estimated directly from this plot.

One of the drawbacks of this type of diagram is that the frequency is not explicitly shown, making it sometimes difficult to distinguish variations in the capacitative behavior. Also, since the measured impedance can often span several orders of magnitude, details of the regions of the diagram with small impedance values tend to be lost when the entire diagram is plotted on a single scale.

Bode diagram – In this type of diagram, the relationship between the frequency ν and the module $|Z|$ or phase angle θ is represented, typically as $\log|Z|$ vs. $\log f$ or θ vs. $\log f$. One of the main advantages of Bode diagrams is that the frequency is shown explicitly as the independent variable. Additionally, since it utilizes a logarithmic scale, phenomena relaxing at higher frequencies can be more easily distinguished. Since EIS is the main technique for studying the reaction mechanism of the Ni-Co alloys and single metal deposition, other details concerning this technique will be discussed later.

Chapter 4 Experimental Setup and Fitting

4.1 Chemical Reagents

4.1.1 Single metal deposition

The electrochemical experiments were conducted at room temperature in a supporting electrolyte of 1500 mol m^{-3} Na_2SO_4 (99.3 %, Fisher) and 500 mol m^{-3} $B(OH)_3$ (99.8 %, Alfa Aesar) in order to minimize complications due to migration of reacting species and to buffer the acid solution. The pH value was adjusted to 3 using concentrated H_2SO_4, as is typical of baths for nickel and cobalt deposition under acidic conditions [2, 22, 24]. All the solutions were freshly prepared and deoxygenated with N_2 (Praxair, grade 4.8-99.998 %) prior to experiments. Deionized water (~pH 6.8) was used to prepare the solutions.

Different $NiSO_4$ (99.3 %, Fisher) and $CoSO_4$ (99.3 %, Fisher) concentrations: 50, 100, 200 mol m^{-3}, etc. were considered to analyze the reaction mechanisms occurring during single metal deposition. No additives or complexing baths (e.g. pyrophosphate, Cl^-) were used in order to avoid the masking of the kinetics by the presence of these compounds.

4.1.2 Alloy co-deposition

The same electrolyte used in the single metal deposition was employed during the alloy co-deposition (refer to Section 4.1.1). Different $NiSO_4/CoSO_4$ concentration ratios in the electrolyte were considered to assess the reaction mechanism of alloy co-deposition, the impacts of the electrical parameters (e.g. cathodic current) on the formation of the alloy and the variation of the anomalous character of the alloy. The ratios used in this study are reported in Tables 8.1 and 9.1 (Chapters 8 and 9).

All the experiments on alloy co-deposition were galvanostatically conducted unless otherwise specified in the text. This mode was used because it is the standard electrochemical mode by which this process is carried out at an industrial level. In addition, it is a convenient way to control the charge passed during deposition for the purpose of comparing the effects of the different experimental conditions with each other. It is important to note that the number of coulombs passed during co-deposition has not been controlled during many

studies reported in the literature. This may have an influence on phenomena such as the HER that may vary over the duration of deposition. Thus, in this work, the duration of each galvanostatic experiment was set to ensure that the total charge transferred was limited to 1.5 C and that steady-state had been reached (i.e. 50 s) long before the experiment was terminated.

4.2 Electrolytic cell

A conventional 3-electrode cell containing approximately 75 ml solution was used to conduct the electrochemical experiments. A pure graphite rod (6.15 mm dia x 152 mm long, Alfa AESAR, 99.999 %) and a $Hg\text{-}Hg_2SO_4$ electrode (Radiometer Analytical) were used as the counter and reference electrodes, respectively. All the potentials referred herein correspond to the SHE scale. The working electrodes used were nickel (Alfa AESAR, 99.999 %), cobalt (Alfa AESAR, 99.95 %) and copper (99.9 %) rotating disks embedded in nylon to provide 1.96×10^{-5} m^2 (0.005 m diameter) exposed area.

These surfaces exhibit lower overpotential for metal deposition than does a foreign substrate such as glassy carbon. Moreover, when obtaining EIS spectra, it is important that the electrode response has reached steady state at the base potential (or base current) prior to the application of a sinusoidal signal at any particular frequency. Since a steady state response was not possible during the deposition of nickel or cobalt onto a substrate such as glassy carbon until the surface was completely covered by the coating, it was necessary to begin with a pre-coated working electrode. However, it was much simpler just to begin with a nickel or cobalt substrate in the first place. A glassy carbon surface was also considered as the working electrode using a pre-coating time (5, 10, 20, 50, 100 and 200 s), which is necessary for EIS. However, competition of the HER with metal deposition was stronger (probably due to roughness of the deposited surface and nucleation effects). This phenomenon was reflected in EIS spectra that were noisy and difficult to reproduce. When no pre-coating time was allowed during the experiments, the spectra became affected by effects of nucleation (i.e. the generation of a third loop) on a foreign substrate, some which was undesirable because it could mask some of the kinetics. Thus, substrates made from the same metals involved in the deposition are considered for the kinetic studies, i.e. Ni-Ni.

Prior to each experiment, the working electrode surface was mechanically polished using SiC-type abrasive paper (1200 grade) and polished to a mirror finish using Buehler

alumina powder (final grain size ≤ 0.05 μm). In order to remove any dust or alumina particles on the electrode surface, the electrodes were then rinsed with deionized water and placed in an ultrasonic cleaner for 5 min. Preparation of cobalt electrodes required more care than that of nickel during experiments since cobalt tended to oxidize more easily.

The working electrode was mounted on a Teflon shaft (EDI101 Radiometer Copenhagen) and rotated using a separate electronic rotator unit (CTV101 Radiometer Copenhagen). A rotation speed of 1,000 rpm was used in most cases in order to mimic the typical conditions during industrial operations and laboratory experiments [15, 33]. The counter electrode was placed a distance of approximately 0.004 m from the working electrode. Its surface area was at least ten times larger than that that of the working electrode to ensure that the reaction at the counter electrode did not limit cell operation. The reference electrode was located as close as possible to the working electrode to minimize the ohmic drop effects. The three electrodes were connected to a PGSTAT 30 galvanostat/potentiostat (Autolab^{TM}) controlled by a personal computer using the GPES and FRA software.

4.3 Inductively coupled plasma analysis

After alloy co-deposition, each sample was immersed in a vial containing a 100 mol m^{-3} HNO_3 solution to dissolve the coatings. The solutions contained in the vials were then analyzed in a high dispersion inductively coupled plasma (ICP) spectrometer (Teledyne Leeman^{TM}, model Prodigy) to measure the concentrations of dissolved cobalt and nickel. These concentrations were used to independently determine the experimental partial current densities for nickel and cobalt co-deposition, from which the current efficiencies and weight percentage of nickel in the alloy could be calculated (Chapter 8). A steady-state model for Co-Ni alloy deposition is also fit to these data in Chapter 9.

4.4 Electrochemical Techniques

EIS was obtained using the frequency response analyzer module (FRA). The potentiostatic mode for the EIS technique was chosen because it yielded a more defined and reproducible spectrum in the low frequency region than the galvanostatic mode [36]. In EIS, some conditions must be met in order to acquire correct spectra. First, a stationary state must be attained before the sinusoidally varying input signal is applied. In potentiostatic mode, a

sinusoidal wave with a given frequency and small amplitude is superimposed on a constant electrode potential. The amplitude is small enough to allow linearization of the response of the system to the input signal, but high enough to yield a response that is detectable from the measurement noise [34, 36, 37]. A wave amplitude of 10 mV was found to be suitable for this purpose. Once the current response to this input reached a stationary state, the software automatically changed the frequency and applied the next sinusoidal potential wave. The frequency was swept from 100 kHz to 20 mHz at 10 points per decade which was more than adequate for the system being studied. Different base *dc* electrode potentials were applied, as will be described. Finally, the solution resistance R_s was estimated from the Nyquist diagram by extrapolating the high frequency portion of the spectrum to the axis of the real component of the impedance.

On the other hand, the maintenance of a smooth electrode and a fixed steady state current were very important during EIS experiments. Consequently, care was taken in designing and conducting these experiments to minimize roughening of the electrodes. For example, the base potential used during the EIS experiments was limited to ensure that the current was never close to the limiting current for the metal reduction. The steady state current was monitored throughout the EIS experiments to ensure that it did not drift and returned to the same value as the frequency was adjusted from one value to the next. The electrode surfaces were carefully examined before and after EIS experiments to ensure that the electrodes remained smooth and bright. All the coatings obtained after performing the EIS experiments remained smooth and bright to the naked eye. SEM images were also taken of some samples after EIS experiments and showed that their surfaces remained smooth. Three replicate EIS experiments were conducted for each condition and found to be virtually identical.

4.5 Least-square fitting

The models presented in this work composed of systems of PDEs and/or ODEs, algebraic expressions and boundary conditions were solved using the finite element method in the COMSOL Multiphysics® 3.5a software package [102]. A Lagrange quadratic polynomial with fourth order of integration was used as the shape function in the finite elements. An Intel Core i5 CPU running at 2.6 GHz with a RAM memory of 12.00 GB was used to carry out the calculations. The span of this procedure requires different times depending on the

complexity of the problem and the amount of experimental data to fit. COMSOL Multiphysics™ 3.5a was coupled with Matlab® to simultaneously solve for the model numerically and fit it to experimental data.

The estimation of the kinetic parameters through modeling of the experimental data for single metal deposition (Chapters 5, 6 and 7) and for the alloy formation (Chapter 9) was carried out using a least-square method $\left(i_T^{model} - i_T^{experimental}\right)^2$ in the Matlab® *R2009b* toolbox. Three different Matlab® routines were used depending on the complexity of the model and the stiffness of the system: fminsearch, fmincon and genetic algorithms [103]. The genetic algorithm method solves optimization problems by mimicking the principles of biological evolution and modifying a population of individual points using rules modeled on gene combinations in biological reproduction. Due to its random nature, this technique was used to find the initial guesses for the other two methods and the region surrounding the roots of the problem. This method was carried out first since it improves the chances of the search not becoming trapped in a local minimum and finding a global solution. Moreover, it does not require the functions to be continuous. Once the location close to the global solution was found, fmincon and fminsearch routines were used to refine and speed up the fitting procedure. In general, fminsearch is faster than fmincon and therefore was the method in most cases. However, verification of the fits obtained by both models was always checked. Initial guesses for these methods were obtained from the genetic algorithm routine or values reported in literature. fmincon is a constrained nonlinear optimization method that uses sequential quadratic programming as the solution algorithm by updating an estimate of the Hessian of the Lagrangian at each iteration [103]. fminsearch is an unconstrained nonlinear optimization method, which uses a simplex search method and does not require numerical or analytic gradients [103]. At each step of the search, a new point in or near the current simplex is generated. The function value at the new point is compared with the function values at the vertices of the simplex and usually replaces one of the vertices, giving a new simplex. This step is repeated until the diameter of the simplex is less than the specified tolerance. See reference [103] for further information concerning these routines.

Statistical evaluations were conducted to analysis the significance of the fits to the experimental data and confidence intervals according to the tests described in literature for linear models [114, 115]. These evaluations were adopted since only a few tests have been developed for nonlinear models [114]. The methods that have been developed are time-

consuming (i.e. Monte Carlo) or the information required to perform these tests is not available at the end of the Matlab® least-square routine. One of these tests for linear models consists of determining if a linear relationship between the response variable and a subset of the regressor variables exists. This procedure requires that the errors in the model be normally and independently distributed with mean zero [115]. To perform the calculations, the variance, covariance matrix and residual sum of squares are calculated. However, this test did not succeed in the analysis of the EIS data since the values estimated for the coefficients testing the hypothesis were overestimated. The calculation of the confidence intervals using linear approaches was also not conclusive, since it led to an overestimation in the intervals for the non-sensitive parameters in the model. This is likely associated with the large amount of non-sensitive parameters in the model. Therefore, in this work the quality and significance of the fits was only based on the use of the genetic algorithm to determine good estimates of the initial guesses and the low residual sum of square errors ($<10^{-3}$) obtained in the fits.

Chapter 5 EIS Modeling of Cobalt Deposition

5.1 Introduction

Different mechanisms have been reported in the literature for cobalt electrodeposition in acidic solutions [6, 38-40]. In general, the most comprehensive studies report that deposition occurs similarly to that of other iron-group metals (i.e. *Fe*) by involving two consecutive 1-electron transfer steps [24, 41-47]. The first step involves the formation of an intermediate adion $Co(I)_{ads}$ which is then consumed in the second step to produce the metal. As shown in section 5.2, thermodynamic calculations indicate that the $CoSO_4$ ion pair is the predominant metal-containing species for conditions prevailing during cobalt deposition from sulphate - borate solutions. For convenience, this ion pair is denoted as Co(II). Cobalt deposition can then be considered to proceed by the following steps:

$$Co(II) + e^- \rightarrow Co(I)_{ads} \qquad (5.1)$$

$$Co(I)_{ads} + e^- \rightarrow Co^0 \qquad (5.2)$$

H^+ reduction is thermodynamically more noble than cobalt deposition and so must also be considered [48]. HER occurring during the deposition of iron-group metals has been considered to proceed according to the Volmer-Tafel mechanism and a single 2-electron transfer step [41-45]. The first step involves the formation of an adsorbed intermediate H_{ads} species on the electrode surface:

$$H^+ + e^- \rightarrow H_{ads} \quad \text{(Volmer)} \qquad (5.3)$$

The second step involves the chemical combination of two H_{ads} to form H_2 (Tafel mechanism), i.e.,

$$2\,H_{ads} \rightarrow H_2 \quad \text{(Tafel)} \qquad (5.4)$$

Reaction (5.3) tends to increase the pH at the electrode/solution interface and eventually can become limited by mass transfer, particularly when carried out at higher overpotentials.

Adapted from J. Vazquez-Arenas and M. Pritzker, "Transient and steady-state model of cobalt deposition in borate-sulphate solutions", Electrochimica Acta, 55, (2010) 8376-8387; and J. Vazquez-Arenas and M. Pritzker, "A comprehensive EIS model for cobalt deposition accounting for homogeneous reactions and adsorptive effects in sulphate media", Electrochimica Acta, Accepted for publication.

These conditions could lead to a third cathodic reaction in which water itself is reduced [49]:

$$H_2O + e^- \rightarrow H_{ads} + OH^- \qquad (5.5)$$

The role of water reduction during the deposition of iron-group metals has been investigated in only a few studies [42, 49]. Therefore, in this study, hydrogen evolution (HER) is considered to occur by both H^+ and water reduction followed by the chemical combination of H_{ads} (i.e., reactions 5.3-5.5). If the pH rise in the vicinity of the electrode due to reactions (5.3) and (5.5) becomes too high, this can cause metal oxide or hydroxide to precipitate at or near the electrode surface.

Boric acid $B(OH)_3$ is commonly added to these plating baths to counteract this pH rise without affecting the quality of the deposits [50]. Different roles ascribed for $B(OH)_3$ include i) adsorption onto the electrode surface [39, 40], ii) inhibition of H^+ reduction by shifting its potential for onset in the negative direction and iii) lowering the pH rise at the cathode surface [40]. Recently, boric acid adsorption was shown to have little influence on the electrode response during cobalt and nickel deposition when carried out on a substrate of the same metal type [41, 51]. However, in none of the previous studies on cobalt deposition have the different possible roles of boric acid been investigated in a comprehensive way over a relatively wide range of potentials and when water reduction and homogeneous reactions have been considered in the reaction mechanism or the effect of agitation included. Consequently, one of the aims of the present Chapter is to derive a physicochemical model for the EIS response of this system to conditions of low and high overpotential, including the appropriate homogeneous reactions as well as water reduction and investigate the effect of the working electrode rotation speed. This analysis is complemented by finding the equivalent electric circuit that best fits the EIS spectra to determine the number of time constants detectable from the experimental data.

5.2 Results

5.2.1 Thermodynamic calculations

Thermodynamic calculations for the solution chemistry of the $CoSO_4$–Na_2SO_4–$B(OH)_3$ system were carried out to identify the predominant dissolved species to be included in the model under the conditions applicable to the EIS experiments. This step is particularly

important given the extensive computational effort required to numerically solve the EIS model and carry out a least-square fit to the experimental data.

Table 5.1. Equilibrium constants used to construct the fraction-pH diagrams shown in Figure 5.1.

Equilibrium reaction	log β	reference
$B(OH)_3 + H_2O \leftrightarrow B(OH)_4^- + H^+$	-9.236	[54]
$2B(OH)_3 = H^+ + B_2O(OH)_5^-$	-9.36	[53]
$3B(OH)_3 = H^+ + B_3O_3(OH)_4^- + 2H_2O$	-7.03 (β_{3B})	"
$4B(OH)_3 = 2H^+ + B_4O_5(OH)_4^{2-} + 3H_2O$	-16.3	"
$H_2O = H^+ + OH^-$	-14 (β_{H2O})	"
$2B(OH)_3 = B_2O_{3(s)} + 3H_2O$	-5.745	"
$B(OH)_3 = H_3BO_{3(s)}$	0.07	"
$B(OH)_3 = HBO_{2(s)} + H_2O$	0.5	"
$Co^{2+} + H_2O \leftrightarrow Co(OH)^+ + H^+$	-9.2	"
$Co^{2+} + 2H_2O \leftrightarrow Co(OH)_2 + 2H^+$	-18.6	"
$Co^{2+} + 3H_2O \leftrightarrow Co(OH)_3^- + 3H^+$	-31.7	"
$Co^{2+} + 4H_2O \leftrightarrow Co(OH)_4^{2-} + 4H^+$	-46.4	"
$2Co^{2+} + H_2O \leftrightarrow Co_2(OH)^{3+} + H^+$	-9.8	"
$4Co^{2+} + 4H_2O \leftrightarrow Co_4(OH)_4^{4+} + 4H^+$	-29.9	"
$Co^{2+} + 2H_2O \leftrightarrow Co(OH)_{2(s)} + 2H^+$	-12.2	"
$Co^{2+} + SO_4^{2-} \leftrightarrow CoSO_{4(aq)}$	2.34	"
$2H^+ + SO_4^{2-} \leftrightarrow H_2SO_4$	0	"
$H^+ + SO_4^{2-} \leftrightarrow HSO_4^-$	1.98	"
$Na^+ + H_2O \leftrightarrow H^+ + NaOH$	-14.18	"
$Co^{2+} + B(OH)_3 + H_2O \leftrightarrow CoB(OH)_4^+ + H^+$	-8.036	[55, 56]

The calculations were done using the chemical equilibrium software package Medusa® in a Windows interface linked to the MS-DOS programs INPUT-SED-PREDOM [52]. Medusa® is based on free energy minimization algorithms developed by Eriksson. The reactions and equilibrium constants required by the software to calculate the fractional distribution of the various species are obtained from different sources in the literature (Table 5.1). Most of the equilibrium constants are available in the HYDRA database within the Medusa® software package [53].

Figure 5.1 presents the equilibrium fractional distribution–pH diagrams for: a) boron-containing species, b) sulphate-containing species and c) cobalt-containing species in a solution containing 1500 mol m^{-3} Na_2SO_4, 500 mol m^{-3} $B(OH)_3$ and 200 mol m^{-3} $CoSO_4$. Figure 5.1a shows that undissociated $B(OH)_3$ is the predominant boron-containing species until the pH rises above approximately 7.7. It is not expected that the pH anywhere within the boundary layer adjacent to the working electrode will increase above this level during Co(II) reduction in a typical experiment [51]. The calculations also indicate that no other boron-containing species co-exists to any measurable degree at pH below 4.5. However, as the pH rises, $B(OH)_3$ becomes less stable relative to $B_3O_3(OH)_4^-$. $B_3O_3(OH)_4^-$ becomes detectable at approximately pH 4.5 and the predominant species from pH 7.7 to 9.7. A small amount of $B_4O_5(OH)_4^{2-}$ is present from pH 8 to 11. $B(OH)_4^-$ becomes stable in alkaline solutions and eventually becomes predominant above pH 10.0.

In the case of sulphate species, the analysis is simpler since only two species predominate between pH 0 and 14. HSO_4^- predominates at pH < 2, while SO_4^{2-} is the main species at pH > 2 (Figure 5.1b). When cobalt-containing species are considered (Figure 5.1c), the ion pair $CoSO_{4(aq)}$ is the only species present in any significant amount over the range 2.3 < pH < 7.6. $CoSO_{4(aq)}$ remains predominant until the pH increases to 7.8 whereupon $Co(OH)_{2(s)}$ begins to precipitate. The predominance of $CoSO_{4(aq)}$ over Co^{2+} stems from the large amount of sulphate present in solution. This differs from the assumption made in a previous model of this system that Co^{2+} is the main form of dissolved cobalt under acidic conditions [38]. Therefore, based on this thermodynamic evaluation, the species $CoSO_{4(aq)}$ (denoted hereafter as Co(II)), H^+, OH^-, $B(OH)_3$ and $B_3O_3(OH)_4^-$ were considered in the model. The homogeneous reactions in which they participate are highlighted in Table 5.1 and included in the model presented in Section 5.3. Na^+ and SO_4^{2-} are not incorporated in the model since they do not participate in homogeneous reactions to any significant extent and migrational transport of the reacting species can be ignored for the conditions of this study.

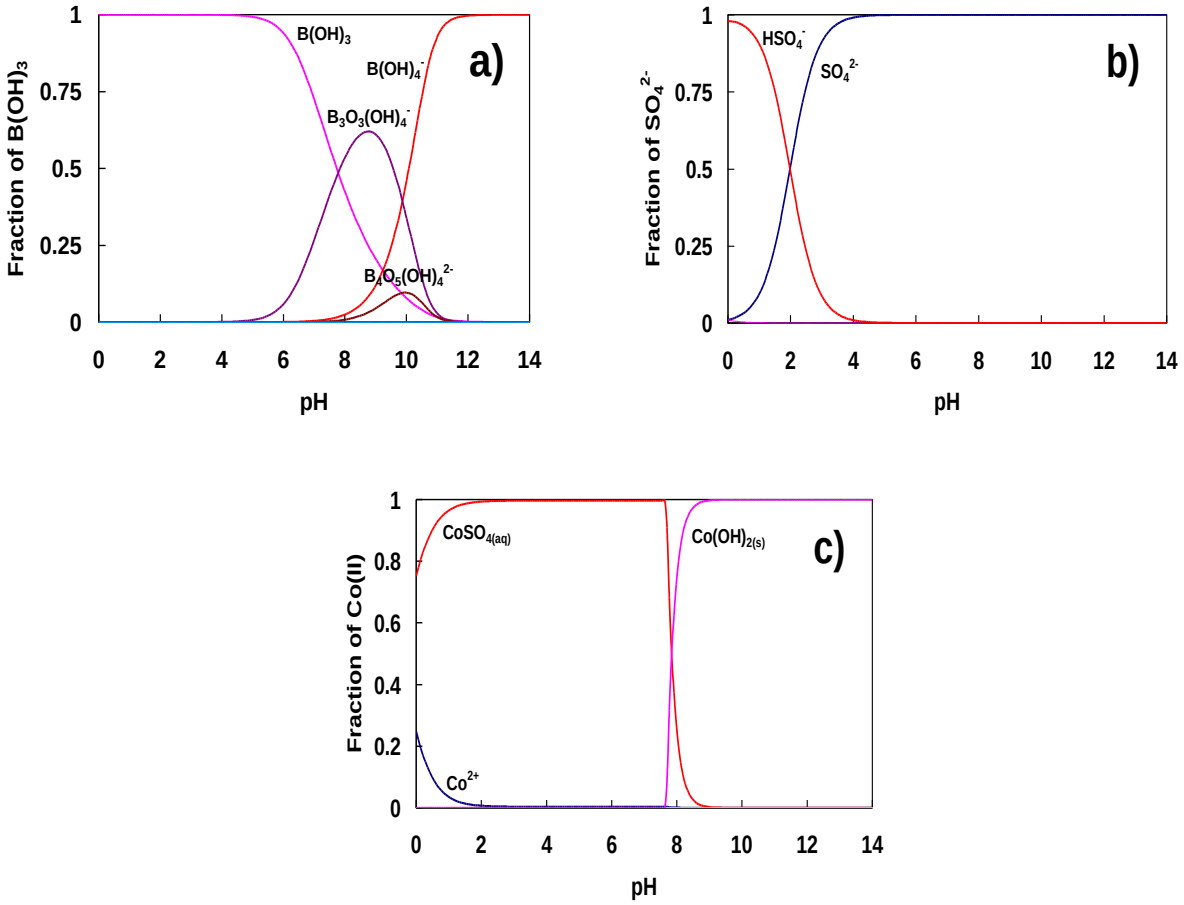

Figure 5.1. Thermodynamic diagrams showing the pH dependence of the fractional distribution of: a) boron-containing, b) sulphate -containing and c) cobalt-containing species in a solution with 500 mol m^{-3} $B(OH)_3$, 1500 mol m^{-3} Na_2SO_4 200 mol m^{-3} $CoSO_4$. The plots were calculated using the equilibrium constants reported in Table 5.1.

5.2.2 Linear sweep voltammetry

Linear voltammograms obtained on a cobalt substrate rotating at 1000 rpm in solutions containing 1500 mol m^{-3} Na_2SO_4, 500 mol m^{-3} $B(OH)_3$ and 0, 50, 100 and 200 mol m^{-3} $CoSO_4$ at pH 3 are shown in Figure 5.2. A sweep rate of 0.050 V s^{-1} was used to scan the potential from the open circuit potential in the negative direction. A gradual increase of the current density depending on the $CoSO_4$ concentration is observed to begin at about –0.71 V, suggesting that cobalt deposition is underway at this potential. From the comparison of the voltammograms in Figure 5.2 with those obtained for nickel deposition [41] (section 6.2.2), two differences are observed. Firstly, Ni(II) reduction appears to begin at more positive

potentials than that of Co(II). Secondly, the magnitude of the current density during cobalt deposition increases more steeply at potentials more negative than –0.75 V than during nickel deposition. Further discussion concerning this second observation will be included later.

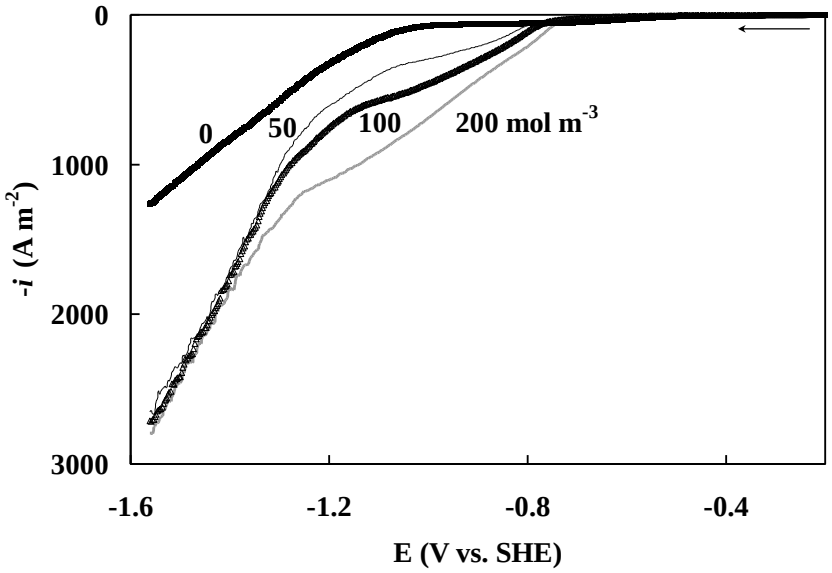

Figure 5.2. Linear voltammograms measured at a scan rate of 0.05 V s^{-1} on a cobalt disk rotating at 1000 rpm in solutions containing 1500 mol m^{-3} Na_2SO_4, 500 mol m^{-3} $B(OH)_3$ and 0, 50, 100 and 200 mol m^{-3} $CoSO_4$ at pH 3.

The occurrence of the HER during cobalt deposition prevents the appearance of a limiting current plateau for Co(II) reduction during the scans. This makes it more difficult to determine the potentials to apply during the chronoamperometry and EIS experiments so that the system is not too strongly influenced by mass transfer effects and a true steady-state is reached. It is worth noting that a shoulder appears in each of the scans in Figure 5.2 obtained in the presence of $CoSO_4$ at more negative potentials between –1 and –1.25 V. To assess whether this shoulder is associated with the limiting current plateau for Co(II) reduction, the current density associated with the shoulder at each $CoSO_4$ concentration was compared with the limiting current density for Co(II) reduction estimated from the Levich equation. In all cases, the current density observed at each shoulder is significantly lower than the estimated limiting current density for cobalt deposition. This suggests that the shoulder is not associated with this reaction.

To gain further insight into the origin of this shoulder, the effect of the presence of $B(OH)_3$ on the linear scans obtained on a cobalt substrate was investigated in solutions containing 200 mol m^{-3} $CoSO_4$ and 1500 mol m^{-3} Na_2SO_4. Figure 5.3 shows a comparison of the responses obtained in a solution containing 500 mol m^{-3} $B(OH)_3$ to one that is borate-free. At low overpotential, $B(OH)_3$ clearly has no effect on the electrode response, whereas at higher overpotential, the presence of boric acid does eventually affect the electrode response by causing an increase in current when the potential reaches −1.3 V, very close to where the shoulder in the linear scans in Figure 5.2 is observed. Zech and Landolt [49] previously reported a similar result and attributed it to the buffering ability of boric acid although they focused only on the HER in boric acid solutions in a metal-free system. In this way, boric acid counteracts the effect of H^+ reduction (reaction 5.3) and water reduction (reaction 5.5) that occur simultaneously during Co(II) reduction and tends to raise the pH at the cathode.

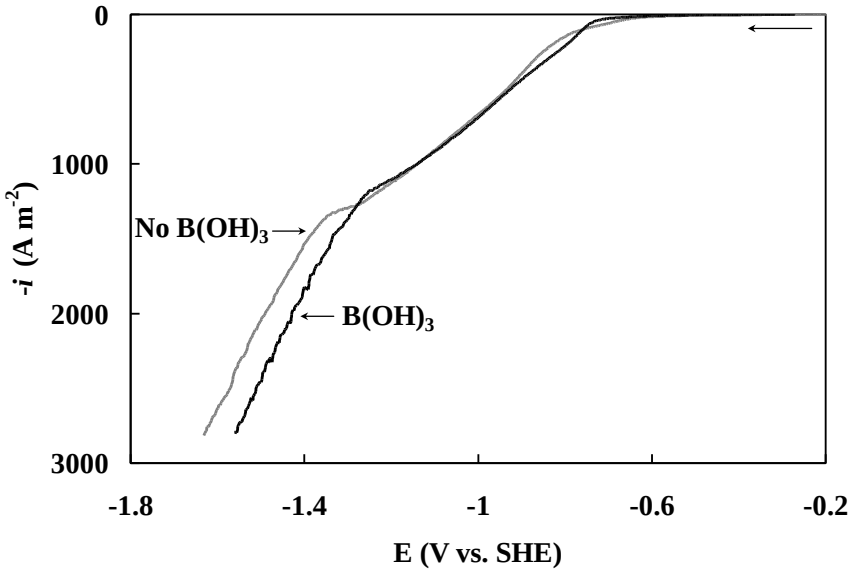

Figure 5.3. Linear voltammograms measured at a sweep rate of 0.05 V s^{-1} on a cobalt disk electrode rotating at 1000 rpm in solutions containing 1500 mol m^{-3} Na_2SO_4 and 200 mol m^{-3} $CoSO_4$ at pH 3 in the presence and absence of 500 mol m^{-3} $B(OH)_3$.

On the basis of numerical modeling, Zech and Landolt showed that in the absence of boric acid the surface pH can increase enough as the scan proceeds to effectively terminate H^+ reduction. Thus, what appears as a shoulder in the scans is a potential range before the onset of water reduction where H^+ reduction is slowing down or has terminated. Zech and Landolt showed that the presence of boric acid counteracts this effect as it undergoes hydrolysis and

releases H^+ ions in the vicinity of the cathode as the surface pH rises. Consequently, the potential where the HER is effectively terminated is shifted considerably in the cathodic direction. Interestingly, the main effect of boric acid observed in Figure 5.3 is to shift the steeper rise portion of the curve at potentials below about –1.3 V in the positive direction rather than to affect the slope of this portion of the curve. Thus, boric acid probably has no effect on the kinetics of water reduction once it is underway.

5.2.3 Electrochemical Impedance Spectroscopy

Nyquist diagrams obtained potentiostatically at three base potentials (–0.86, –0.91, –0.96 V) in solutions at pH 3 containing 1500 mol m^{-3} Na_2SO_4, 500 mol m^{-3} $B(OH)_3$ and $CoSO_4$ concentrations of 100 and 200 mol m^{-3} are shown in Figures 5.4a and 5.4b, respectively. The response at the high frequency end of the spectra which is strongly associated with the electrolyte resistance R_s is found to be very similar at the two $CoSO_4$ concentrations. This behavior is not surprising since R_s is affected much more strongly by the major components of the solution (i.e. supporting electrolyte) than $CoSO_4$. R_s is determined by extrapolating the real component of the impedance at high frequencies in Figures 5.4 to be 1.5 x 10^{-4} Ω m^2, a parameter used subsequently in the model.

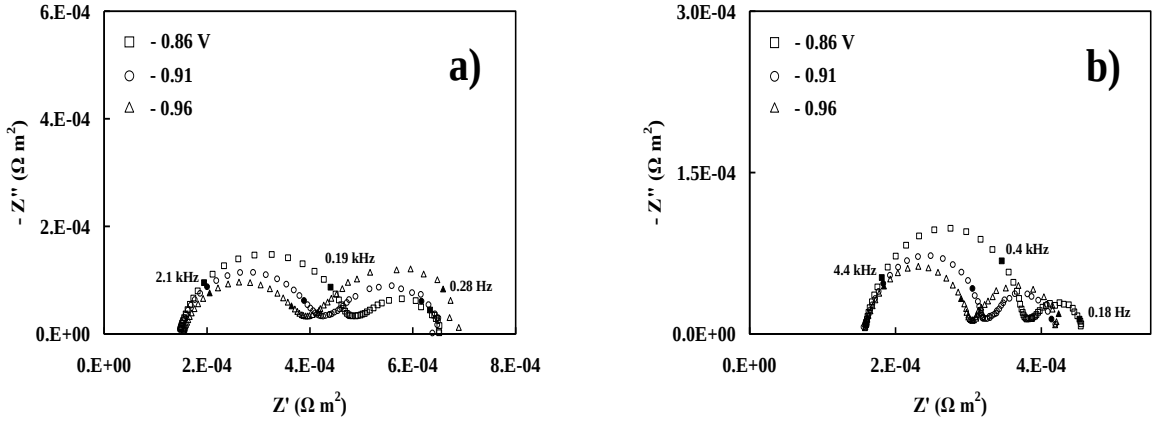

Figure 5.4. Nyquist diagrams obtained on a cobalt disk rotating at 1000 rpm and base potentials –0.86, –0.91 and –0.96 V in solutions at pH 3 containing 1500 mol m^{-3} Na_2SO_4, 500 mol m^{-3} $B(OH)_3$ and a) 100 or b) 200 mol m^{-3} $CoSO_4$.

Two loops appear in all Nyquist diagrams when Co(II) is present and its reduction occurs. As the base potential is made more negative at both $CoSO_4$ concentrations, the first loop at higher frequencies becomes smaller while the lower frequency loop grows in size. A similar observation was made for the EIS spectra obtained at more positive base potentials in an earlier study on cobalt deposition [51]. A comparison between Figure 5.4a and 5.4b at fixed potential shows that both the real and imaginary components of the impedance at any frequency become smaller as the $CoSO_4$ concentration in solution increases. This effect indicates that Co(II) concentration directly or indirectly affects the electrode response at all frequencies.

5.2.4 Determination of the time constants on the basis of EIS experiments

As previously mentioned, two different approaches can be used to fit EIS data – electric circuit analogs and physicochemically-based models. It would be interesting to analyze the same experimental data on cobalt deposition and obtain useful information about the system using the two methods. The number of parameters required to fit an equivalent circuit model to experimental EIS spectra is generally less than the number of parameters required for a physicochemical model to fit the same data. We applied some strategies reported in the literature [57, 58] to determine the number of time constants revealed by the experimental EIS data and used EQUIVCRT® software to obtain an equivalent circuit that best fits the experimental data [59]. One of these strategies consists in plotting the imaginary component of the impedance (Z") vs. log f (i.e. symbols without filling in Figure 5.5). Therefore, a maximum or minimum in the plot is associated with the relaxation of a new time constant.

Figure 5.5 shows the variation of the real and imaginary components of the impedance with the logarithm of the frequency for the experiments reported in Figure 5.4a. This type of diagram more clearly displays the characteristic time constants during a frequency scan than does a Bode plot [58]. The plot in Figure 5.5 reveals two characteristic time constants of ~ 9.75 $x10^{-4}$ s at high frequencies and ~ 1.35 s in the low-to-intermediate frequency range. Therefore, based on these findings, two time constants should be sufficient to describe the electrode response during the EIS experiment. According to the likely reaction mechanism for this system, cobalt deposition and the HER presumably contribute to both of these time constants. In order to determine the best fitting equivalent circuit for the experimental spectra, we tested a wide range of possibilities using the EQUIVCRT® software

and found that two R_tQ elements (i.e. resistor-constant phase element) in parallel or in series with respect to the solution resistance R_s yields the best fit with the smallest number of required elements. R_t represents the charge transfer resistance due to an electrode reaction, while Q represents the capacitative effect of the reaction affected by the adsorption of intermediates on the electrode since its exponent is higher than 0.75.

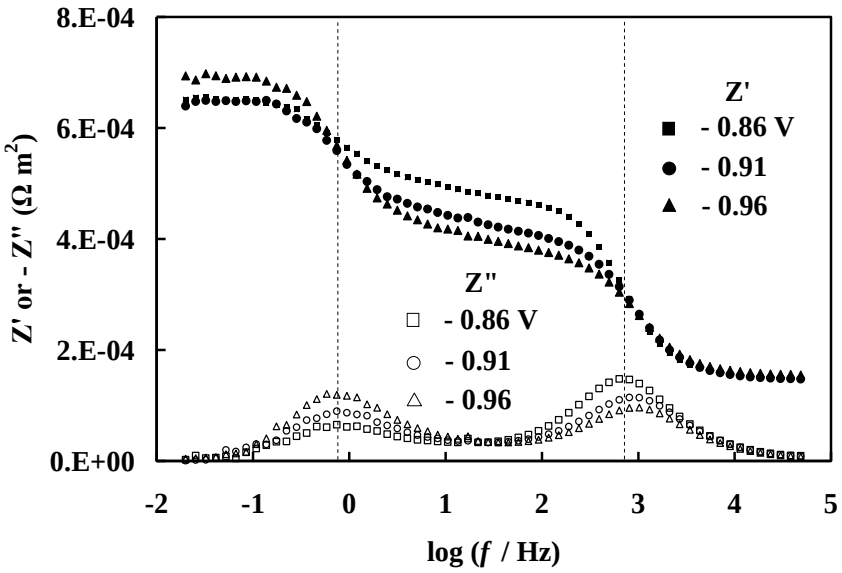

Figure 5.5. Dependence of the real and imaginary components of the impedance on the logarithm of the frequency obtained from the EIS experiments shown in Figure 5.4a for 100 mol m^{-3} $CoSO_4$ and base potentials –0.86, –0.91 and –0.96 V.

A capacitor is an electrical circuit element which describes the behavior of the electrode-solution interface since charges cannot cross the interface but form a structured region that varies according to the electrode potential [31]. In electrochemistry, it is commonly used to describe adsorption phenomena or double layer effects. However, its usefulness in fitting equivalent circuits to EIS data has been less successful due to dispersion effects (i.e. a single-valued time constant does not apply for a reaction or physical phenomenon) usually attributed to inhomogeneities in geometry, reactivity or potential along the electrode surface [37]. Instead, the use of constant phase element defined as CPE = $Q(j\omega)^{\alpha}$ has been found to more satisfactorily fit experimental EIS data. When n is close to 1.0, the impedance of the CPE resembles that one of a capacitor $1/Z = C(j\omega)$. A constant phase element with an exponent higher than 0.75 is consistent with the mechanisms for Co(II) and H^+ reduction which involve the adsorption of intermediates (reactions 5.1 – 5.3)

and lends further support to the conclusion that these two time constants are associated with these two processes occurring simultaneously on the cathode surface. No segments of the EIS spectra at a 45° slope with respect to the imaginary impedance axis that would reflect diffusional transport appear in any of the spectra. Furthermore, all experimental spectra can be very well fit without the need for a diffusive Warburg impedance in the circuit; in fact, its introduction always leads to a poorer fit regardless of the configuration assumed for the electric circuit, e.g. RQ in series or parallel.

On the other hand, as will be shown later, the working electrode rotation speed has an important effect on the electrode response during the EIS experiments, indicating that convective mass transport plays a role. Therefore, the equivalent circuit for this system should ideally include a convective Warburg impedance. Analytical solutions have not been typically developed for the convective-diffusion equation and so only numerical or semi-analytical solutions are tractable. Thus, it is not possible to develop a general expression for the convective Warburg impedance applicable for any situation and a new solution must be derived for each particular problem. The approach originally reported by Tribollet and Newman [58] can be followed, but the problem they considered was much simpler than that of the current study. The derivation of the convective Warburg impedance for a multicomponent/multi-reaction system involving adsorbed intermediates, such as cobalt electrodeposition, is very lengthy and involved. Given that the primary aim of fitting an equivalent circuit model to the experimental data is to determine the number of time constants revealed in the spectra and the focus of this study is on the physicochemical model, we do not go beyond fitting the spectra with a relatively simple circuit involving two R_tQ elements (i.e. resistor-constant phase element) and the solution resistance R_s and do not include a convective Warburg impedance element.

5.3 Model development

5.3.1 Mechanism and kinetics

This section presents a physicochemical model for the response observed during EIS experiments that is consistent with the thermodynamic analysis carried out in Section 5.2.1. The reaction mechanism for Co(II) reduction and the associated electrode kinetics are based on previous studies of cobalt and nickel deposition [41-47, 51], while the assumptions and

formulation of the mass transport equations are provided in section 5.3.2. Co(II) reduction is considered to proceed via the consecutive 1-electron transfer steps given by reactions (5.1) and (5.2) without the assumption as to which is rate-controlling. No stable dissolved Co(I) species has been reported in any modeling or experimental work reported in the literature [42, 49, 51]. Thus, such a species is not considered in the reaction mechanism. The HER which takes place concurrently with Co(II) reduction occurs by both H^+ (reaction 5.3) and water (reaction 5.5) reduction. Both these reactions occur by Volmer-type mechanisms and generate H_{ads} on the electrode surface which block active sites that otherwise could be occupied by $Co(I)_{ads}$. The consumption of the H_{ads} species proceeds by their chemical combination to form H_2 molecules (reaction 5.4). The reduction of water molecules furnishes H_{ads} species to the surface of the electrode at high overpotential or low $CoSO_4$ concentration. Based on previous studies, the amount of $B(OH)_3$ that adsorbs is negligibly small and so is ignored [41, 51].

Assuming Langmuir adsorption behavior for $Co(I)_{ads}$ and H_{ads} and neglecting the reverse direction of the electrode reactions, we can write the following expression for the current density associated with cobalt deposition (reactions 5.1 and 5.2):

$$i_{Co} = -F(r_{1Co} + r_{2Co}) = -F\left[\begin{array}{l} k_{01Co}\ \exp\left(-\alpha_{Co1}\dfrac{FE'}{RT}\right)C^{s}_{Co(II)}(1-\theta_{Co}-\theta_{H}) \\ \\ +\ k_{02Co}\ \exp\left(-\alpha_{Co2}\dfrac{FE'}{RT}\right)\theta_{Co} \end{array}\right] \qquad (5.6)$$

The current density due to H^+ and water reduction (also ignoring the reverse direction of each step) is given by the following expression:

$$i_{HER} = -F(r_{1H} + r_{1W}) = -F\left[\begin{array}{l} k_{01H}\ \exp\left(-\beta_{H}\dfrac{FE'}{RT}\right)C^{s}_{H} \\ \\ +\ k_{01W}\ \exp\left(-\beta_{W}\dfrac{FE'}{RT}\right) \end{array}\right](1-\theta_{Co}-\theta_{H}) \qquad (5.7)$$

The rates of formation of $Co(I)_{ads}$ and H_{ads} on the active surface sites are respectively [51]:

$$\begin{aligned} R_{Co} &= \Gamma_{Co}\frac{d\theta_{Co}}{dt} = r_{1Co} - r_{2Co} \\ &= k_{01Co}\ \exp\left(-\alpha_{Co1}\frac{FE'}{RT}\right)C^{s}_{Co(II)}(1-\theta_{Co}-\theta_{H}) - k_{02Co}\ \exp\left(-\alpha_{Co2}\frac{FE'}{RT}\right)\theta_{Co} \end{aligned} \qquad (5.8)$$

$$R_H = \Gamma_H \frac{d\theta_H}{dt} = r_{1H} + r_{1W} - 2r_{2H}$$
$$= \left[k_{01H} \exp\left(-\beta_H \frac{FE'}{RT} \right) C_H^s + k_{01W} \exp\left(-\beta_W \frac{FE'}{RT} \right) \right] (1 - \theta_{Co} - \theta_H) - 2k_{2H}\theta_H^2 \quad (5.9)$$

where Γ_{Co} and Γ_H represent their adsorption densities that completely fill a monolayer. In Eqs. (5.6) – (5.9), $C^s_{Co(II)}$ and C^s_H represent the surface concentrations of Co(II) and H^+, respectively, while θ_{Co} and θ_H are the fractions of the electrode area covered by $Co(I)_{ads}$ and H_{ads}, respectively. k_{01Co}, k_{02Co}, k_{01H}, k_{2H} and k_{01W} are rate constants and $\alpha_{Co1}, \alpha_{Co2}$, β_H and β_W are charge transfer coefficients for reactions (5.1)–(5.3) and (5.5). E' is the electrode potential corrected for the electrolyte ohmic resistance R_s:

$$E' = E - i_T R_s \quad (5.10)$$

The total current density is composed of faradaic ($i_f = i_{Co} + i_{HER}$) and capacitative (i_c) components:

$$i_T = i_f + i_c = i_{Co} + i_{HER} + C_{dl} \frac{dE'}{dt} \quad (5.11)$$

where C_{dl} is the double layer capacity.

5.3.2 Development of transport model

The following assumptions are made in developing the transport equations applicable to a rotating disk working electrode:

a) The current distribution is uniform over the working electrode; only transport in the direction normal to the electrode surface is considered.
b) The transport properties are uniform throughout the system.
c) The solution is incompressible and isothermal at 298 ºK.
d) Ideally dilute behavior is assumed in the solution (i.e. activity coefficients are equal to 1.0).
e) Since the solution contains an abundance of supporting electrolyte, the migration fluxes of the reacting species are negligible relative to their diffusive and convective fluxes.
f) The homogeneous reactions exhibit fast kinetics relative to that of the electrode reactions and the rates of mass transport of the dissolved species and so remain at pseudo-equilibrium.

The solution is separated into a boundary layer region of thickness δ and a well-mixed bulk region where concentrations are uniform. The bulk region is considered to be fully established at a distance of 3δ from the electrode [59], where δ is given as:

$$\delta = 1.61 D_j^{1/3} \Omega^{-1/2} \upsilon^{1/6} \qquad (5.12)$$

D_j is the diffusion coefficient of any species in the system subject to chemical gradients, Ω is the rotational speed of the working electrode and υ is the kinematic viscosity of the solution (see Table 5.2 for their numerical values). The 1-dimensional flux for each soluble species *j* (i.e. Co(II), H^+, OH^-, $B(OH)_3$ and $B_3O_3(OH)_4^-$) due to diffusion and convection can be expressed as:

$$N_j = -D_j \frac{\partial C_j}{\partial y} + v_y C_j \qquad (5.13)$$

where the solution velocity $v_y = -0.51023\ \Omega^{3/2} \upsilon^{-1/2} y^2$ (5.14)

Table 5.2. Parameters held fixed during the fitting procedure.

Parameter	Value	Reference
$D_{Co(II)}$	7.32 x 10^{-10} m^2 s^{-1}	[60]
D_H	9.31 x 10^{-9} m^2 s^{-1}	[35]
D_{OH-}	5.26 x 10^{-9} m^2 s^{-1}	"
$D_{B(OH)3}$	1.0 x 10^{-9} m^2 s^{-1}	[49]
$D_{B3O3(OH)4-}$	1.0 x 10^{-9} m^2 s^{-1}	"
υ	1.5 x 10^{-6} m^2 s^{-1}	[60]
R_s	~1.5 x 10^{-4} ohm m^2	This work
C_{dl}	0.65 F m^{-2}	[51]
Γ_{Co}	5.9 x10^{-5} mol m^{-2}	"
Γ_{Ni}	5.98 x10^{-5} mol m^{-2}	[41]
Γ_H	1.24 x10^{-6} mol m^{-2}	"

5.3.3 Steady-state model

Coupling of the steady state transport equations for these species to the homogeneous reactions within the region $0 < y < 3\delta$ yields:

$$-\nabla \cdot N_{Co(II)} = 0 \qquad (5.15)$$

$$-\nabla \cdot N_{H^+} + \nabla \cdot N_{OH^-} + \nabla \cdot N_{B_3O_3(OH)_4^-} = 0 \qquad (5.16)$$

$$-\nabla \cdot N_{B(OH)_3} - 3\nabla \cdot N_{B_3O_3(OH)_4^-} = 0 \qquad (5.17)$$

The following algebraic equations describing the equilibria of the homogeneous reactions (water dissociation and boric acid hydrolysis) apply everywhere within the boundary layer and complete the system of equations to be solved:

$$C_{OH^-} C_{H^+} - \beta_{H_2O} = 0 \qquad (5.18)$$

$$\frac{C_{B_3O_3(OH)_4^-} C_{H^+}}{(C_{B(OH)_3})^3} - \beta_{3B} = 0 \qquad (5.19)$$

The boundary condition at outer edge $y = 3\delta$ is given by:

$$C_j(3\delta) = C_j^b \qquad (5.20)$$

where C_j^b is the bulk concentration of species *j*. The boundary conditions at the electrode surface are:

$$D_{Co(II)} \frac{\partial C_{Co(II)}}{\partial y}\bigg|_{y=0} - r_{1Co} = 0 \qquad (5.21)$$

$$D_H \frac{\partial C_H}{\partial y}\bigg|_{y=0} - D_{OH^-} \frac{\partial C_{OH^-}}{\partial y}\bigg|_{y=0} - D_{B_3O_3(OH)_4^-} \frac{\partial C_{B_3O_3(OH)_4^-}}{\partial y}\bigg|_{y=0} - r_{1H} - r_{1W} = 0 \qquad (5.22)$$

$$D_{B(OH)_3} \frac{\partial C_{B(OH)_3}}{\partial y}\bigg|_{y=0} + 3 D_{B_3O_3(OH)_4^-} \frac{\partial C_{B_3O_3(OH)_4^-}}{\partial y}\bigg|_{y=0} = 0 \qquad (5.23)$$

The equilibria described in Eqs. (5.18) and (5.19) also apply at y = 0 and in the bulk solution.

5.3.4 Transient EIS model

The detailed methodology to derive the impedance response on the basis of physicochemical models can be found elsewhere [25, 37, 41, 51]. During a potentiostatic EIS experiment, the system is driven by an input signal comprised of a small-amplitude sinusoidal wave superimposed on a constant *dc* potential $\overline{E}$, i.e.,

$$E = \bar{E} + \tilde{E}\exp(j\omega t) = \bar{E} + \Delta E \tag{5.24}$$

where $\tilde{E}$ is the phasor of the potential, j is the imaginary unit $\sqrt{-1}$ and ω is the angular frequency of the applied wave. Since the amplitude of the input sinusoidal wave is very small in this technique (ΔE = 10 mV from peak to peak), the transient problem can be linearized and the response of each resulting dependent variable written as:

$$a = \bar{a} + \tilde{a}\exp(j\omega t) = \bar{a} + \Delta a \tag{5.25}$$

The first term on the right hand side of Eq. (5.25) corresponds to the steady-state (zeroth order) response for the variable of interest, whereas the second term (first order) gives the transient response to the EIS input. When Eqs. (5.24) and (5.25) are substituted into the governing transient equations and the resulting expressions are linearized, the system can be decomposed into separate zeroth and first order linear problems. The zeroth order problem corresponds to the steady state problem defined in section 5.3.3. The solution to the first order problem depends on the zeroth order solution. In the derivation to follow, a phasor is designated by a variable with a tilde on top. The response to the EIS input is obtained by solving the system of differential equations presented in this section to yield the impedance Z, a complex quantity defined as:

$$Z = \frac{\tilde{E}}{\tilde{i}_T} \tag{5.26}$$

where $\tilde{i}_T$ is the total current phasor.

The first order boundary value problem can be written in terms of the following fluxes for the various soluble species *j* in the system:

$$\tilde{N}_j = -D_j \frac{\partial \tilde{C}_j}{\partial y} + v_y \tilde{C}_j \tag{5.27}$$

Mass balances for the various species within $0 < y < 3\delta$ yield:

$$-\nabla \cdot \tilde{N}_{Co(II)} - j\omega \tilde{C}_{Co(II)} = 0 \tag{5.28}$$

$$-\nabla \cdot \tilde{N}_{H^+} + \nabla \cdot \tilde{N}_{OH^-} + \nabla \cdot \tilde{N}_{B_3O_3(OH)_4^-} - j\omega \tilde{C}_H + j\omega \tilde{C}_{OH^-} + j\omega \tilde{C}_{B_3O_3(OH)_4^-} = 0 \tag{5.29}$$

$$-\nabla \cdot \tilde{N}_{B(OH)_3} - 3\nabla \cdot \tilde{N}_{B_3O_3(OH)_4^-} - j\omega \tilde{C}_{B(OH)_3} - 3\, j\omega \tilde{C}_{B_3O_3(OH)_4^-} = 0 \tag{5.30}$$

As in the steady-state model, the equilibrium conditions for the homogeneous reactions complete the system of equations describing the concentration profiles in the boundary layer region:

$$C^{s}_{H^+}\tilde{C}^{s}_{OH^-} + C^{s}_{OH^-}\tilde{C}^{s}_{H^+} = 0 \tag{5.31}$$

$$C^{s}_{H^+}\tilde{C}^{s}_{B_3O_3(OH)_4^-} + C^{s}_{B_3O_3(OH)_4^-}\tilde{C}^{s}_{H^+} - 3\beta_{3B}(C^{s}_{B(OH)_3})^2\tilde{C}^{s}_{B(OH)_3} = 0 \tag{5.32}$$

Note that the dependent variables without a tilde on top correspond to steady state conditions. The first order boundary conditions required to solve Eqs. (5.28) – (5.32) are as follows:

$$D_{Co(II)}\frac{\partial\tilde{C}_{Co(II)}}{\partial y}\bigg|_{y=0} - \left(\frac{\partial r_{1Co}}{\partial E'}\right)\tilde{E}' - \left(\frac{\partial r_{1Co}}{\partial C^{s}_{Co(II)}}\right)\tilde{C}^{s}_{Co(II)} - \left(\frac{\partial r_{1Co}}{\partial \theta_{Co}}\right)\tilde{\theta}_{Co} - \left(\frac{\partial r_{1Co}}{\partial \theta_{H}}\right)\tilde{\theta}_{H} = 0 \tag{5.33}$$

$$\begin{aligned} &D_H\frac{\partial\tilde{C}_H}{\partial y}\bigg|_{y=0} - D_{OH^-}\frac{\partial\tilde{C}_{OH^-}}{\partial y}\bigg|_{y=0} - D_{B_3O_3(OH)_4^-}\frac{\partial\tilde{C}_{B_3O_3(OH)_4^-}}{\partial y}\bigg|_{y=0} - \left(\frac{\partial r_{1H}}{\partial E'}\right)\tilde{E}' - \left(\frac{\partial r_{1H}}{\partial C^{s}_{H}}\right)\tilde{C}^{s}_{H} \\ &- \left(\frac{\partial r_{1H}}{\partial \theta_{H}}\right)\tilde{\theta}_{H} - \left(\frac{\partial r_{1H}}{\partial \theta_{Co}}\right)\tilde{\theta}_{Co} - \left(\frac{\partial r_{1W}}{\partial E'}\right)\tilde{E}' - \left(\frac{\partial r_{1W}}{\partial \theta_{H}}\right)\tilde{\theta}_{H} - \left(\frac{\partial r_{1W}}{\partial \theta_{Co}}\right)\tilde{\theta}_{Co} = 0 \end{aligned} \tag{5.34}$$

$$D_{B(OH)_3}\frac{\partial\tilde{C}_{B(OH)_3}}{\partial y}\bigg|_{y=0} + 3D_{B_3O_3(OH)_4^-}\frac{\partial\tilde{C}_{B_3O_3(OH)_4^-}}{\partial y}\bigg|_{y=0} = 0 \tag{5.35}$$

Eqs (5.31) and (5.32) also apply at both boundaries, while the following condition holds at $y = 3\delta$:

$$\tilde{C}_j(3\delta) = 0 \tag{5.36}$$

The transient problem is completed by deriving the first order expressions for Eqs. (5.6) – (5.9) to relate the phasors for the fractional surface coverages of $Co(I)_{ads}$ and H_{ads} and the current to each other:

$$\begin{aligned} &\left[\left(\frac{\partial r_{1Co}}{\partial E'}\right) - \left(\frac{\partial r_{2Co}}{\partial E'}\right)\right]\tilde{E}' + \left(\frac{\partial r_{1Co}}{\partial C^{s}_{Co(II)}}\right)\tilde{C}^{s}_{Co(II)} + \left[\left(\frac{\partial r_{1Co}}{\partial \theta_{Co}}\right) - \left(\frac{\partial r_{2Co}}{\partial \theta_{Co}}\right) - j\omega\Gamma_{Co}\right]\tilde{\theta}_{Co} \\ &+ \left(\frac{\partial r_{1Co}}{\partial \theta_{H}}\right)\tilde{\theta}_{H} = 0 \end{aligned} \tag{5.37}$$

$$\begin{aligned} &\left[\left(\frac{\partial r_{1H}}{\partial E'}\right) + \left(\frac{\partial r_{1W}}{\partial E'}\right)\right]\tilde{E}' + \left(\frac{\partial r_{1H}}{\partial C^{s}_{H}}\right)\tilde{C}^{s}_{H} + \left[\left(\frac{\partial r_{1H}}{\partial \theta_{H}}\right) + \left(\frac{\partial r_{1W}}{\partial \theta_{H}}\right) - 2\left(\frac{\partial r_{2H}}{\partial \theta_{H}}\right) - j\omega\Gamma_{H}\right]\tilde{\theta}_{H} \\ &+ \left[\left(\frac{\partial r_{1H}}{\partial \theta_{Co}}\right) + \left(\frac{\partial r_{1W}}{\partial \theta_{Co}}\right)\right]\tilde{\theta}_{Co} = 0 \end{aligned} \tag{5.38}$$

$$\tilde{i}_T - \left(\frac{\partial i}{\partial E'}\right)\tilde{E}' - \left(\frac{\partial i}{\partial C_{Co}}\right)\tilde{C}^{s}_{Co} - \left(\frac{\partial i}{\partial C_{H}}\right)\tilde{C}^{s}_{H} - \left(\frac{\partial i}{\partial \theta_{Co}}\right)\tilde{\theta}_{Co} - \left(\frac{\partial i}{\partial \theta_{H}}\right)\tilde{\theta}_{H} - C_{dl}\,j\omega\tilde{E}' = 0 \tag{5.39}$$

The partial derivatives in Eqs. (5.33) – (5.39) are evaluated for steady state conditions using the expressions given in Eqs. (5.6) – (5.10). The potential phasor $\tilde{E}$ required to determine the impedance is related to the phasor $\tilde{E}'$ through the ohmic correction as follows:

$$\tilde{E}' = \tilde{E} - \tilde{i}_T R_s \tag{5.40}$$

Since the system defined by Eqs. (5.28) – (5.32) and (5.37) – (5.39) contains one less equation than the total number of phasors ($\tilde{C}^s_{Co(II)}$, $\tilde{C}^s_H$, $\tilde{C}^s_{B(OH)_3}$, $\tilde{C}^s_{B_3O_3(OH)_4^-}$, $\tilde{C}^s_{OH^-}$, $\tilde{\theta}_{Co}$, $\tilde{\theta}_H$, $\tilde{E}'$ and $\tilde{i}_T$), it is possible to obtain a solution for the ratio of any two phasors as a function of the angular frequency ω, but not a solution for any single phasor. However, this is not a problem since the aim is to solve for the frequency dependence of impedance Z which by definition is the ratio between $\tilde{E}$ and $\tilde{i}_T$ (Eq. 5.26).

5.4 Model fitting

The original objective was to obtain one set of parameters that gave a good fit of the model to all the experimental EIS spectra obtained at the different $CoSO_4$ concentrations and base potentials. As in previous studies on Ni and Co deposition at low overpotentials [41, 51], this did not give a satisfactory fit for all the spectra despite repeated efforts using different search procedures and convergence criteria for the fitness subroutine. Therefore, the requirement of obtaining a single set of parameters for all conditions is relaxed. The parameters held fixed during the fitting procedure are listed in Table 5.2. The numerical values of ν and the various diffusion coefficients are taken from the literature [35, 49, 62]. The values of C_{dl}, Γ_{Co} and Γ_H are held constant at the values obtained in a previous study on cobalt deposition since they depend primarily on structural factors and adsorbate-adsorbent interactions [51]. The kinetic parameters obtained at the different Co(II) concentrations and base potentials from the fitting procedure are listed in Table 5.3. Kinetic parameters for the second step of cobalt deposition and for water reduction (k_{02Co}, α_{Co2}, k_{01W}, β_W) are not reported in Table 5.3 because the model is found to have little or no sensitivity to their values and so cannot be determined with good certainty. Figure 5.6 shows comparisons between the model-fitted and measured spectra obtained at the following $CoSO_4$ concentrations and potentials: a) 200 mol m^{-3} and –0.86 V, b) 100 mol m^{-3} and –0.86 V, c) 200 mol m^{-3} and –0.91 V, and d) 100 mol m^{-3} and –0.96 V. Good agreement is achieved between the model and experimental data

although larger deviation is observed at low frequencies as the potential becomes more negative (Figures 5.6c and 5.6d).

Table 5.3. Parameters obtained from the fit of the model to the EIS data.

E (V)	[$CoSO_4$] (mol m^{-3})	k_{01Co} (10^{-8} m s^{-1})	α_{Co1}	k_{01H} (10^{-9} m s^{-1})	k_{2H} (10^{-2} mol m^{-2} s^{-1})	β_H
-0.86	200	4.01	0.28	0.92	1.39	0.49
	100	5.45	0.29	1.04	3.54	0.49
-0.91	200	3.36	0.31	0.96	1.70	0.49
	100	2.66	0.31	1.04	1.68	0.48
-0.96	200	3.95	0.29	1.03	2.35	0.49
	100	1.89	0.30	1.04	3.33	0.50

Bode diagrams for the impedance modulus corresponding to the Nyquist plots in Figure 5.6 have been compared to the model-predicted plots to examine the quality of the model fit depending on the frequency. This is shown in Figure 5.7. The calculated Bode plots are obtained using the physicochemical model with the fitted kinetic parameters given in Table 5.3. Excellent agreement between the experimental and model-predicted plots is obtained over the entire frequency range under all conditions shown in Figure 5.6, with the exception of low frequencies for the measurements made in the presence of 100 mol m^{-3} $CoSO_4$ at a base potential of –0.96 V (Figure 5.7b). This region corresponds to the low frequency loop in Figure 5.6d where the largest deviation between the measured and calculated Nyquist plots is observed. The poorer fit for these conditions suggests that some aspect of the model that is particularly important at low frequencies requires further refinement. The obvious choices are properties associated with transport of dissolved species within the boundary layer. It should be noted that the analysis originally focused on electrode kinetics and the reaction mechanism of cobalt electrodeposition and not on transport properties. Given the many model parameters to be fitted, initially the transport properties such as diffusion coefficients were kept fixed at the values reported in the literature and not as adjustable parameters with which to fit the model. However, the fact that the least-square fit of the model of the experimental data is very good at high frequencies and consistently

better than at low frequencies suggests that further improvement requires some focus on the transport properties.

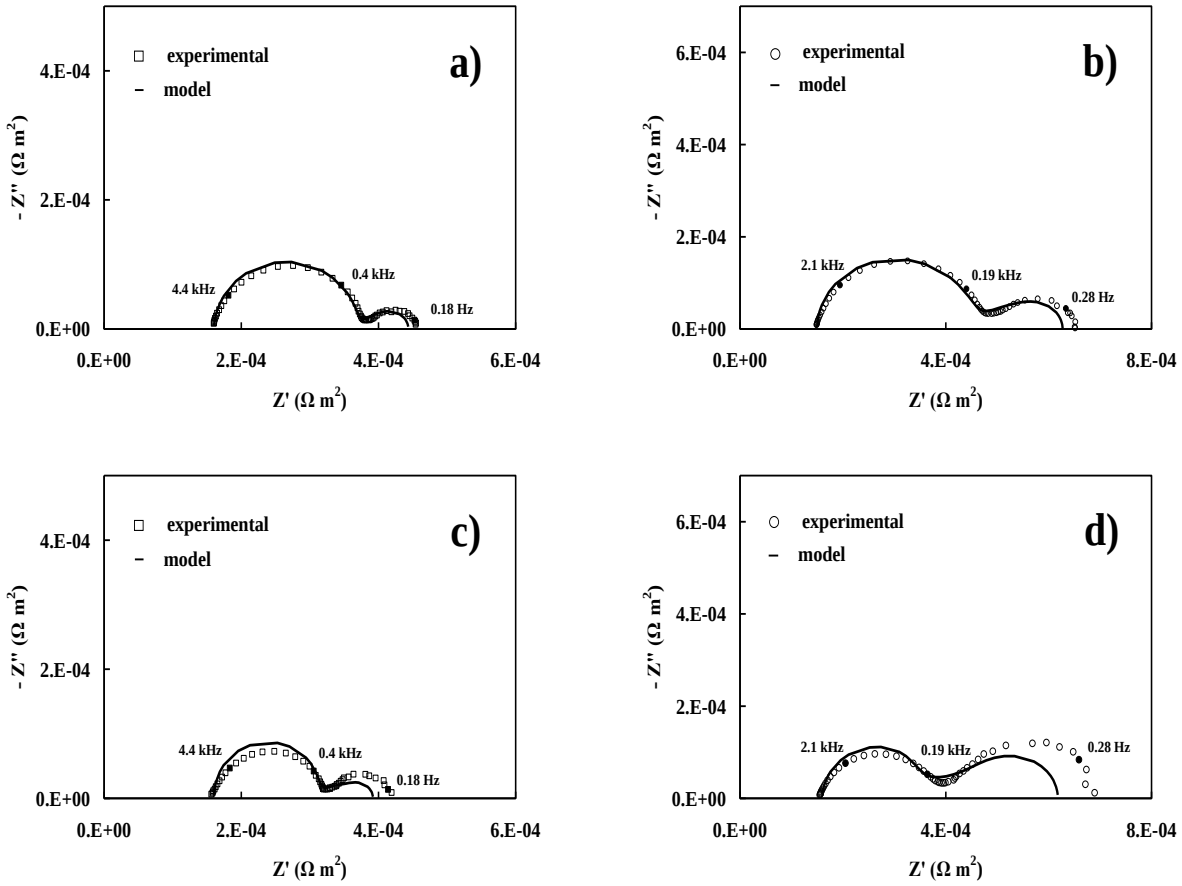

Figure 5.6. Comparison of experimental (symbols) and model-fitted Nyquist diagrams (continuous line) obtained on a cobalt disk rotating at 1000 rpm in solutions at pH 3 containing 1500 mol m^{-3} Na_2SO_4, 500 mol m^{-3} $B(OH)_3$ and a) 200 mol m^{-3} $CoSO_4$ at –0.86 V, b) 100 mol m^{-3} $CoSO_4$ at –0.86 V, c) 200 mol m^{-3} $CoSO_4$ at –0.91 V and d) 100 mol m^{-3} $CoSO_4$ at –0.96 V.

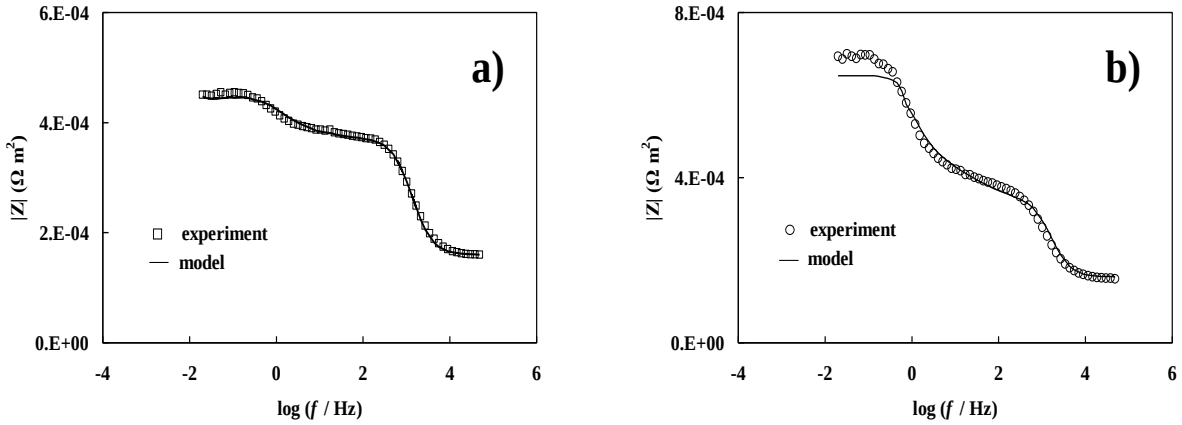

Figure 5.7. Comparison of experimental and model-simulated Bode-module diagrams obtained on a cobalt disk rotating at 1000 rpm in solutions at pH 3 containing 1500 mol m^{-3} Na_2SO_4, 500 mol m^{-3} $B(OH)_3$ and a) 200 mol m^{-3} $CoSO_4$ at –0.86 V and b) 100 mol m^{-3} $CoSO_4$ at –0.96 V.

The expression for the fluid velocity v_y in Eq. (5.14) is only the first term of a series expansion and is complete only under the limit of an infinitely large Schmidt number ($Sc = \upsilon / D_i$). To investigate the effect of this truncation, we carried out a simulation of the model to compute the Nyquist plot for solution containing 100 mol m^{-3} $CoSO_4$ and base potential of –0.86 V using the parameters listed in Tables 5.2 and 5.3 and the 3-term expansion for v_y, i.e.

$$v_y = -0.51023\ \Omega^{3/2}\upsilon^{-1/2}y^2 + 0.33333\ \Omega^2\upsilon^{-1}y^3 - 0.102667\ \Omega^{5/2}\upsilon^{-3/2}y^4 \qquad (5.41)$$

As observed in Figure 5.8, this leads to a slight improvement in the agreement between the measured and computed spectra in the low frequency loop. Far more successful are the results obtained when the diffusion coefficients of Co(II) and H^+ are also allowed to vary from the values given in Table 5.2 and the model is re-fit to the experimental spectra. Figure 5.9 shows the result obtained after fitting the model to the experimental data obtained in solutions containing 100 mol m^{-3} $CoSO_4$ at a base potential of –0.86 V at electrode rotation speeds of 500, 1500 and 2000 rpm, while maintaining the kinetic parameters at the values given in Table 5.3. The agreement between the measured and model-predicted spectra particularly at low frequency has been significantly improved. The best-fit values of $D_{Co(II)}$ and D_H are found to be 6.62 x 10^{-10} and 8.89 x 10^{-9} m^2 s^{-1}. It should be noted that the original diffusion coefficients in Table 5.2 are the values for infinite dilution conditions [35,

60]. The fact that the fitted values are lower than those at infinite dilution is reasonable since diffusion coefficients are expected to decrease as the solution becomes more concentrated.

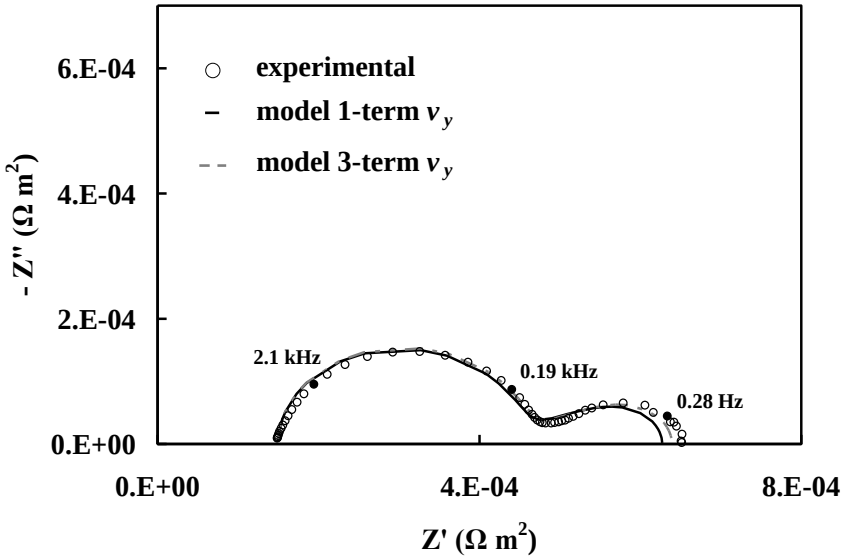

Figure 5.8. Comparison of experimental and model-simulated Bode-module diagrams obtained on a cobalt disk rotating at 1000 rpm in solutions at pH 3 containing 1500 mol m^{-3} Na_2SO_4, 500 mol m^{-3} $B(OH)_3$ and 100 mol m^{-3} $CoSO_4$ at –0.86 V, considering a 1-term and 3-term expansion in the series for v_y (eq. 5.41).

It is interesting to note that both loops in the spectra do not appear as perfect semi-circular arcs and instead are flattened. This behavior is common and often attributed to heterogeneities on the electrode due to phenomena such as surface roughness and distribution of reaction rates over the electrode surface. When this behavior is observed, a CPE is used in equivalent circuit models rather than a capacitance to enable a better fit to the experimental spectra. As evident from Figures 5.6, 5.8 and 5.9, the physicochemical model is able to account for the flattening of the loops despite the fact that it assumes that the electrode surface is uniform and does not exhibit any heterogeneous behavior. This shows that it is not necessary to invoke heterogeneous behavior to account for flattening of the loops. Such a conclusion could only be reached on the basis of a physicochemical model and highlights an advantage of this approach to interpreting EIS spectra.

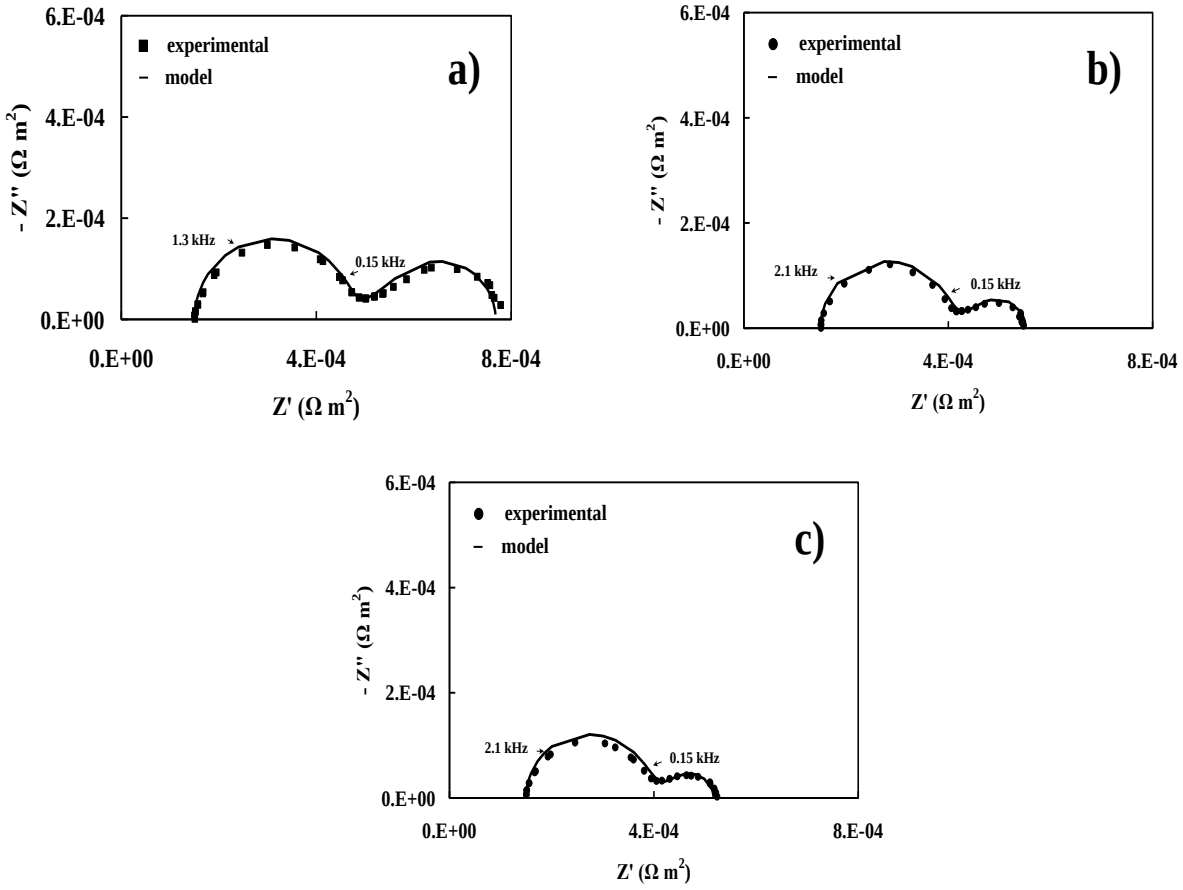

Figure 5.9. Comparison of experimental (symbols) and model-fitted Nyquist diagrams (continuous line) obtained on a cobalt disk in solutions at pH 3 containing 1500 mol m^{-3} Na_2SO_4, 500 mol m^{-3} $B(OH)_3$, 100 mol m^{-3} $CoSO_4$ at –0.86 V at rotation speeds of: a) 500, b) 1500 and c) 2000 rpm. Fitting is carried out keeping the kinetic parameters constant at the values listed in Table 5.3.

In a previous publication [51], experimental data obtained at more positive potentials without considering homogeneous reactions ($B(OH)_3$ hydrolysis and water dissociation) and water reduction in the model was analyzed. To determine whether the numerical values obtained for the kinetic parameters of Co(II) and H^+ reduction are strongly affected by the inclusion of these homogeneous reactions, the values reported in Table 5.3 are compared with those obtained in this earlier study [51] in which the homogeneous reactions and water reduction are excluded. The values of k_{01Co} obtained therein are similar but k_{01H} values are two orders of magnitude smaller than when the model includes the homogeneous reactions and water reduction. α_{Co1} increases by 0.1, while β_H remains the same. These effects on the

parameter estimates confirm the importance of including the role of boric acid via the hydrolysis reaction, in particular, in the model. It is worth noting that it is primarily the kinetics parameters associated with the HER that are affected by the neglect of these homogeneous reactions, which is a reasonable result given that the homogeneous reactions affect H^+ and not Co(II) and that Co(II) reduction is not strongly affected by pH under the prevailing experimental conditions.

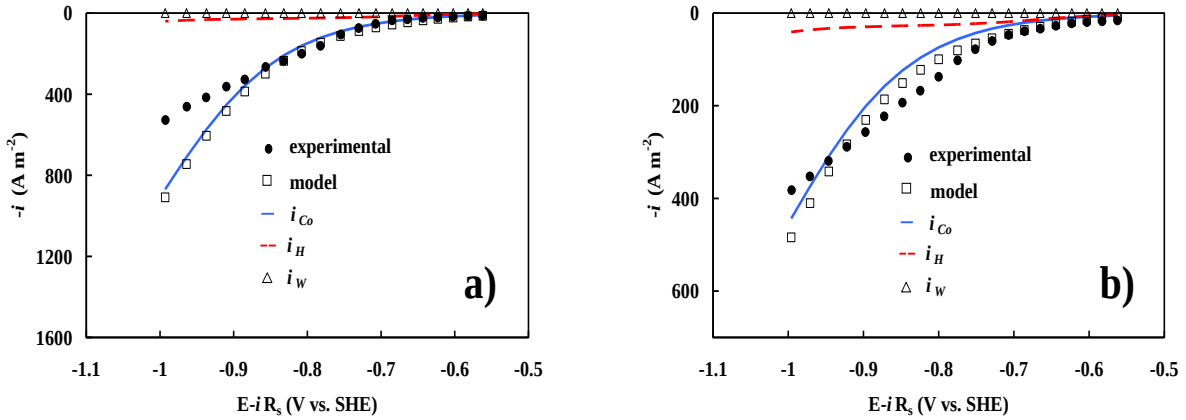

Figure 5.10. Comparison of experimental (black circles) and computed (squares) steady-state polarization curves obtained on a cobalt disk rotating at 1000 rpm in solutions at pH 3 containing 1500 mol m^{-3} Na_2SO_4, 500 mol m^{-3} $B(OH)_3$ and a) 200 and b) 100 mol m^{-3} $CoSO_4$. Also shown are the partial current densities for cobalt deposition (blue continuous line), H^+ reduction (dashed red continuous line) and water reduction (crossed green continuous line). Curves are generated using parameters listed in Table 5.3.

To further assess the model, steady-state polarization curves are simulated using the kinetic parameters reported in Table 5.3 for –0.91 V and 200 mol m^{-3} $CoSO_4$ and compared to experimentally determined ones. Steady-state polarization curves have been obtained in solutions containing 200 (Figure 5.10a) and 100 (Figure 5.10b) mol m^{-3} $CoSO_4$ from a series of chronoamperometry experiments between –0.56 and –1.06 V by monitoring the current until steady state is reached. Reasonable agreement between the predicted and measured current density is observed although some deviation is found at the most negative potentials in 200 mol m^{-3} $CoSO_4$ (Figure 5.10a). It is important to note that the computed curves are not obtained by any fitting and instead are based entirely on parameters obtained independently from the EIS spectra. The plot for i_{Co} shows that Co(II) reduction does not reach a limiting

current plateau over the range of electrode potentials considered. In this study, electrodeposition is restricted to moderate enough overpotentials that the currents are well below the limiting currents for Co(II) reduction. The limiting current densities in 100 and 200 mol m^{-3} $CoSO_4$ solutions are estimated using the Levich equation to be ~ 995 A m^{-2} and 1990 A m^{-2}, respectively.

These calculations also show that current density for water reduction remains insignificant regardless of the potential and $CoSO_4$ concentration in this study. This result is consistent with the previous observation that the computed EIS response is unaffected by the kinetic parameters associated with this reaction. In addition to simulating the steady state polarization curves, we went further by re-fitting the model to these experimental data and obtaining a new set of kinetic parameters. Although not included here, the agreement between the model-fitted and experimental curves was excellent at all potentials and both $CoSO_4$ concentrations. Also, as shown in earlier studies on Ni and Co deposition [41, 51], all the experimental data obtained at the different $CoSO_4$ concentrations could be fit with a single set of kinetic parameters.

The model is also used to calculate quantities that cannot be experimentally measured but provide useful information on the behavior of the system, e.g., steady state surface pH and Co(II) concentration. Figure 5.11 shows the variation of the steady state surface pH with potential at the two $CoSO_4$ concentrations. The model predicts the interfacial pH to rise as high as 5.3 at the most negative potential of –0.96 V applied during the EIS experiments. A comparison of this value with that obtained in a previous study [51] on cobalt deposition that did not include any homogeneous reactions in the EIS model reveals the importance that boric acid hydrolysis, in particular, and water dissociation have in mitigating the rise of the surface pH. For instance, the surface pH at –0.81 V is computed to be 4.2 when these homogeneous reactions are considered, but 6.8 when they are not [51]. As shown in Figure 5.1c, the increase in the surface pH is important (along with the Co(II) surface concentration) since it can lead to the formation of $Co(OH)_{2(s)}$ at the electrode surface which hinders cobalt deposition. Although the model presented herein does not include the formation of $Co(OH)_{2(s)}$, it is still useful in this regard since it can be used to determine whether the conditions for the onset of its precipitation have been reached. This model shows that $Co(OH)_{2(s)}$ should not form on the electrode surface during any of the EIS experiments regardless of the potential or $CoSO_4$ concentration. This is consistent with visual inspection

and microscopic analysis of the deposit surfaces produced during the course of the EIS experiments.

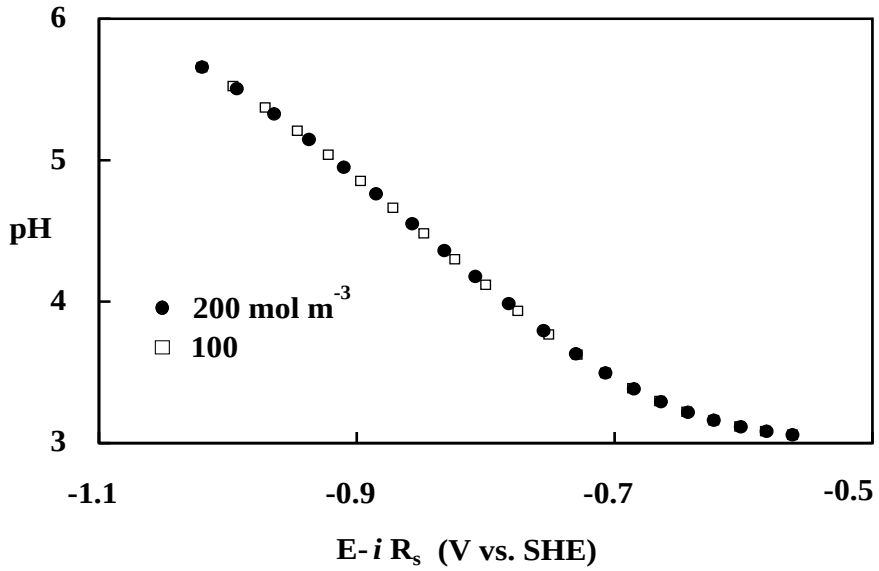

Figure 5.11. Variation of the computed steady state interfacial pH with potential on a cobalt disk rotating at 1000 rpm in the presence of 1500 mol m^{-3} Na_2SO_4, 500 mol m^{-3} $B(OH)_3$ and 200 or 100 mol m^{-3} $CoSO_4$ at pH 3. Curves are generated using parameters listed in Table 5.3.

To further examine the role of $B(OH)_3$ in buffering the rise of the surface pH, the model has been used to determine the variation of $C^{s}_{B(OH)_3}$ with potential at the two $CoSO_4$ concentrations once steady state has been reached (not shown). These results show that the consumption of $B(OH)_3$ by hydrolysis to $B_3O_3(OH)_4^-$ at the electrode surface increases as the potential becomes more negative in response to the depletion of H^+ by the HER.

The effect of potential on the steady state fractional surface coverages θ_{Co} and θ_H of $Co(I)_{ads}$ and H_{ads}, respectively, at the two $CoSO_4$ concentrations is shown in Figure 5.12. θ_{Co} remains very small on the order of 10^{-3} – 10^{-4} regardless of the potential and bulk $CoSO_4$ concentration, reflecting that the first step of Co(II) reduction is rate-controlling. Thus, all $Co(I)_{ads}$ sites formed by reaction (5.1) are rapidly converted to metallic cobalt by reaction (5.2) and the two electrons involved in the reduction of Co(II) to metallic Co are effectively transferred simultaneously. This finding is consistent with what has been previously reported for cobalt and nickel deposition at lower overpotentials [41, 51]. H^+ reduction, on the other

hand, does not appear to be strongly controlled by a single step as in the case of Co(II) reduction. This result is supported by the modeling results indicating that θ_H reaches much larger values than does θ_{Co} and increases as the potential becomes more negative and the rate of the first step of H^+ reduction is enhanced (Figure 5.12).

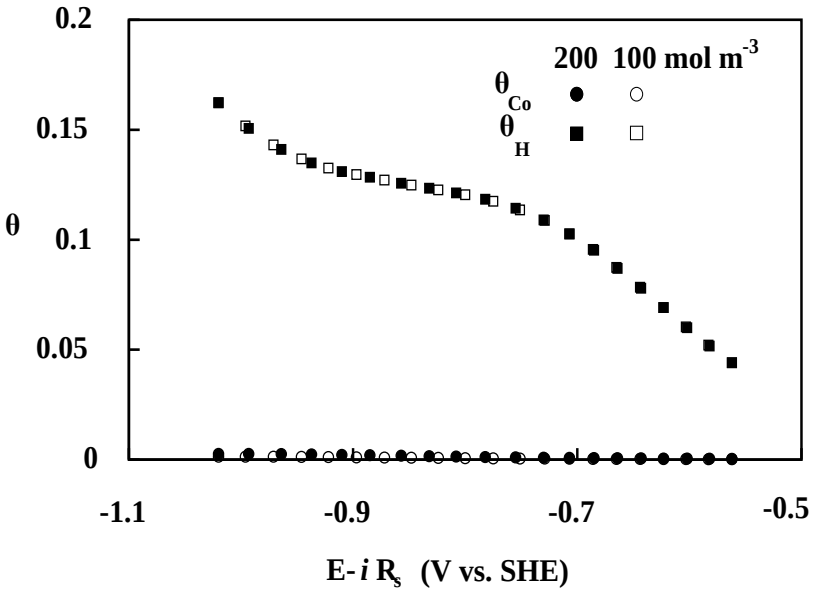

Figure 5.12. Variation of the computed steady state fractional coverage of H_{ads} and $Co(I)_{ads}$ with potential on a cobalt disk rotating at 1000 rpm in the presence of 1500 mol m^{-3} Na_2SO_4, 500 mol m^{-3} $B(OH)_3$ and 200 or 100 mol m^{-3} $CoSO_4$ at pH 3. Curves are generated using parameters listed in Table 5.3.

5.5 Sensitivity analysis

The sensitivity of the electrode response to changes in variables or parameters associated with a particular step of a reaction mechanism also reflects the extent to which the overall reaction rate is controlled by that step. As mentioned above, the model is found to be sensitive to some parameters, moderately to some others and very insensitive to still yet others. In addition, the kinetic parameters are also found to vary with potential and Co(II) concentration (Table 5.3). To more closely assess the certainty of these parameter estimates, we conduct a sensitivity analysis to determine the effect of changing the value of each parameter by the small amount of 5% on the resulting spectra while keeping the others fixed at the best-fit values listed in Table 5.3. The results of this analysis for –0.86 V and 200 mol

m^{-3} $CoSO_4$ presented in Figure 5.13 are representative of those obtained for the other conditions. These results indicate that the model is very sensitive to α_{Co1} (Figure 5.13a). Given the sensitivity of the EIS technique and the excellent reproducibility of the data, the effect on the spectrum shown in Figure 5.13a due to a change in α_{Co1} by as little as 5% would be easily detectable from the analysis. Thus, there is a good certainty regarding the estimates of this parameter shown in Table 5.3. It is also worth noting that changes to α_{Co1} affect the higher frequency loop much more than the lower frequency loop, suggesting that it is associated more strongly with the phenomenon found in section 5.2.4 to have a time constant ~ 9.75 $x10^{-4}$ s than with the one having a time constant of ~ 1.35 s.

The computed electrode response shows some sensitivity to changes in β_H (Figure 5.13b), k_{2H} (Figure 5.13c) and k_{01Co} (not shown), but the effect is less than in the case of α_{Co1}. Variations in these parameters by ~10% lead to changes in the spectra that would be clearly observable and so we are also confident of the certainty of their estimated values in Table 3. The analysis also reveals that both loops in the Nyquist plot are similarly affected by changes in the kinetic parameters for H^+ reduction. On the other hand, a variation of the parameters associated with the second step of Co(II) reduction and water reduction by 5% has no noticeable effect on any aspect of the spectrum (not shown here). Consequently, we do not report estimates for these parameters in Table 5.3. The lower sensitivity to these parameters can be attributed to two main factors. In the case of the second step of Co(II) reduction, its more facile kinetics allows it to respond much more quickly to the driving force during the EIS experiments than does the first step and so its effect cannot be detected by this technique (or any others currently available). In the case of water reduction, analysis of the model reveals that this reaction does not occur to a significant enough extent at the potentials of this study for its parameters to be determined with any certainty.

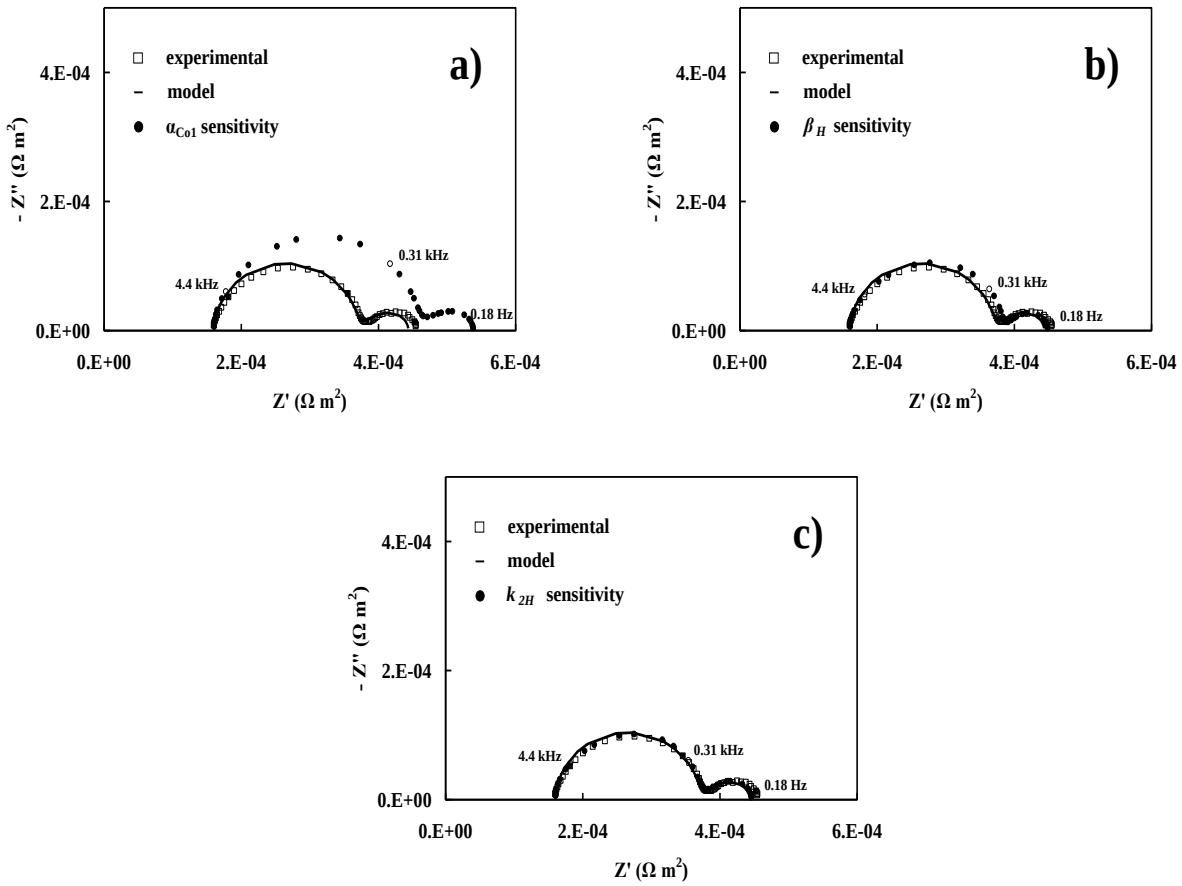

Figure 5.13. Sensitivity analysis performed by computing the effect of decreasing each of the following parameters by 5 %: a) α_{Co1}, b) β_H and c) k_{2H} (black circle) at a base potential –0.86 V and 200 mol m^{-3} $CoSO_4$. Original fitted model (continuous line) and experimental data (squares) are included for comparison.

Chapter 6 EIS Modeling of Nickel Deposition

6.1 Introduction

The reduction of metal ions to their elemental form commonly occurs by consecutive one-electron transfer steps [61, 63]. Such a mechanism has been considered for Ni(II) reduction in several studies [23, 44, 45, 47, 64]. Perhaps the most extensive study of nickel deposition was carried out by Wiart et al. [44, 45] on brass in different chloride, sulphate and mixed sulphate-chloride (Watts) electrolytes. This study showed that the electrode kinetics depends on the type of anion present in the solution. However, regardless of the type of electrolyte, the reaction mechanism was reported to be similar and involved the formation of the intermediate adion $Ni(I)_{ads}$ in the first step, i.e.,

$$Ni(II) + e^- \rightarrow Ni(I)_{ads} \qquad (6.1)$$

For convenience, Ni(II) above represents the soluble $NiSO_4$ ion pair, which is found to be the predominant species (i.e. see Figure 6.1 in the next section showing the fractional distribution diagram for Ni(II) fraction vs. pH) at the electrolyte compositions considered in this study from pH 1-7.

Two possible steps were proposed by Wiart et al. [44, 45] for the subsequent reaction of this intermediate. In the first alternative, it is converted to elemental nickel by the 1-electron step:

$$Ni(I)_{ads} + e^- \rightarrow Ni^0 \qquad (6.2)$$

In the second alternative, the intermediate acts as a catalyst for reduction of Ni(II) by a 2-electron step. However, its occurrence has not been confirmed by other authors. Likewise, Proud and Mueller [64] studied nickel electrodeposition on vitreous carbon at low concentrations using sodium sulphate and chloride as the supporting electrolyte at pH 3. Based on the considerations proposed by Wiart et al. [44, 45], they provided further support that nickel deposition occurs exclusively by reactions (6.1) and (6.2) above.

Adapted from J. Vazquez-Arenas and M. Pritzker, "EIS study of nickel deposition in borate-sulphate solutions", Journal of Electrochem. Soc., 157, (2010) D283-D294.

Since hydrogen evolution reaction (HER) occurs simultaneously during nickel deposition, it also must be included in the mechanism. Although the reaction has been assumed to proceed via a single 2-electron step by some researchers [44, 45], more comprehensive mechanisms involving the formation of the adsorbed intermediate H_{ads} have been considered in several other studies [24, 46, 64]. In these cases, HER was considered to occur by a 1-electron step (see reaction 5.3) followed by chemical combination (reaction 5.4) of adjacent H_{ads} adatoms, similar to that proposed to occur during cobalt deposition (refer to Chapter 5).

The adions and adatoms play important roles not only as intermediates but also by blocking surface sites that otherwise would be available for Ni(II) and H^+ to react according to steps 6.1 and 5.3, respectively. Previous studies have provided supporting evidence that H_{ads} blocks sites at the expense of the iron-group metal intermediates (i.e., $Ni(I)_{ads}$, $Fe(I)_{ads}$) [41, 46, 51]. Regardless of the specific mechanism, H^+ reduction increases the surface pH when the overpotential becomes high enough. In order to avoid this problem, boric acid is also commonly added to nickel plating baths to buffer the pH and prevent the precipitation of nickel hydroxides or oxides [65]. Although boric acid ($B(OH)_3$) can have other possible effects, it has been shown not to play a significant role as an adsorbed intermediate or catalyst during nickel deposition [41]. Its capacity as a buffering agent stems from the equilibrium of the hydrolysis reaction given in Table 5.1.

The depletion of H^+ at the electrode surface will presumably occur when the potential becomes negative enough during the course of deposition because of its low bulk concentration at pH 3. In this situation, water reduction (reaction 5.5) should become the main pathway to form H_{ads} on the substrate and the main cause for the rise of the surface pH, whereby the effect of boric acid becomes noticeable at high overpotentials.

Direct current techniques can elucidate some aspects of electrodeposition mechanisms, but are not always able to unambiguously identify all the reaction steps, determine kinetic parameters and distinguish between alternative mechanisms. In recent years, EIS has proven to be a robust and powerful technique for the quantitative characterization of the phenomena occurring during metal electrodeposition such as transport, adsorption and multi-step charge transfer reactions [24]. The relaxation of these phenomena gives rise to either inductive or capacitive loops in EIS spectra characterized by different distributed time constants. The most common approach in quantitatively analyzing EIS spectra is to fit equivalent electric circuit analogs to the experimental data. Although this

approach is relatively simple, direct interpretation of the results in terms of actual physicochemical processes and detailed reaction mechanisms can be ambiguous. A better approach in this regard is to interpret the EIS spectra on the basis of physicochemical models that explicitly account for kinetics and mass transport effects. To date, only one study has compared simulations of a physicochemical model for nickel deposition to experimental EIS spectra due to the mathematical complexities of this approach [47]. However, this study did not include any least-square fitting of the impedance model to experimental data in order to assess the suitability of specific reaction mechanisms and estimate kinetic parameters. The other EIS studies of this system involved only simulations of spectra with no comparison to experimental data [44, 45, 64]. A least-square fitting to estimate parameters would be very useful to better understand the electrochemistry involved as well as be useful for engineering aspects related to process scale-up and design.

Therefore, in this chapter, *dc* and impedance techniques are employed to investigate nickel deposition on a nickel rotating disk electrode at low-to-intermediate overpotentials. Chronoamperometry and electrochemical impedance spectroscopy experiments are conducted at electrode potentials chosen on the basis of linear sweep voltammetry experiments. These data are analyzed in terms of a physicochemical model for Ni(II) reduction that accounts for diffusive and convective transport of dissolved species, the HER and the presence of boric acid. This model is virtually identical to the one presented and implemented in the previous Chapter for Co(II) reduction. As mentioned above, boric acid has been proposed to play a number of roles during nickel deposition. In this study, the role of boric acid as a buffer and the influence of the pH are examined in detail. The EIS model is fit (least-square) to spectra measured at different base potentials and Ni(II) concentrations to estimate the kinetic parameters for the proposed mechanism. Once the parameters are obtained, steady state polarization curves are computed using the model and compared to experimentally determined ones. Model simulations are also carried out to gain further insight into the potential and concentration dependence of other important quantities that cannot be measured (i.e. adsorption density, interfacial pH).

6.2 Results

6.2.1 Thermodynamic calculations

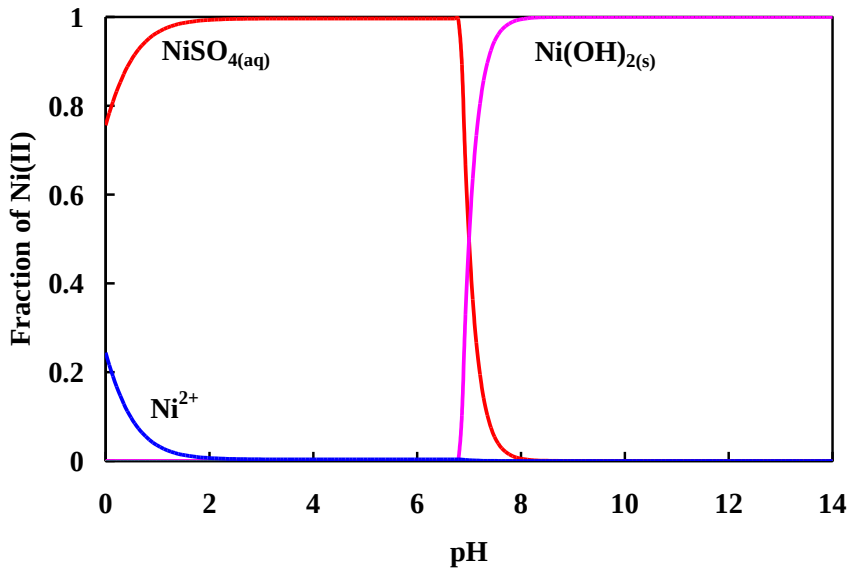

Figure 6.1. Thermodynamic diagram showing the dependence of the fractional distribution of nickel-containing species on pH in a solution containing 500 mol m^{-3} $B(OH)_3$, 1500 mol m^{-3} Na_2SO_4 and 200 mol m^{-3} $NiSO_4$.

Figure 6.1 shows a predominance diagram for the fractional distribution of Ni(II) species as a function of the pH in the $NiSO_4$–Na_2SO_4–$B(OH)_3$ system. As discussed with regard to the $CoSO_4$–Na_2SO_4–$B(OH)_3$ system deposition (Chapter 5), these diagrams are useful to identify the most important (predominant) species to consider in a system. This figure shows that the $NiSO4_{aq}$ ion pair (denoted in the text as Ni(II)) is the most predominant species in solution in the range $0 < pH < 6.79$. Not surprisingly, this result is attributed to the high concentration of SO_4^{2-} in solution, similarly to the result obtained for $CoSO_{4aq}$ in the cobalt system (refer to Figure 5.1a). At $pH > 6.79$ $Ni(OH)_{2(s)}$ is formed due to the limited solubility of Ni(II) in more alkaline solutions. Thus, it is important to consider this limiting pH since it will restrict the operating conditions during nickel plating. A comparison of Figures 6.1 and 5.1c reveals that $Ni(OH)_{2(s)}$ can form at a lower pH of 6.79 than does $Co(OH)_{2(s)}$ which first forms at pH 7.6. This situation may allow cobalt deposition to be carried out at somewhat more negative potentials or higher current densities without the formation of a hydroxide or oxide on the electrode surface than nickel deposition.

6.2.2 Linear sweep voltammetry

Figure 6.2 shows linear voltammograms obtained on a nickel substrate rotating at 1000 rpm in solutions containing 1500 mol m^{-3} Na_2SO_4, 500 mol m^{-3} $B(OH)_3$ and 0, 50, 100 and 200 mol m^{-3} $NiSO_4$ at pH 3. In each case, the potential was scanned at a rate of 0.050 V s^{-1} proceeding from the OCP in the negative direction. As expected, the current density at any potential increases as the Ni(II) concentration rises. Evidence from Figure 6.2 suggests that Ni(II) reduction is already occurring when potentials of about –0.8 V are reached during the scans since the electrode responses are clearly dependent on Ni(II) concentration at this point. The occurrence of both H^+ reduction and water reduction during the scan prevents the appearance of a mass transport limiting current plateau for Ni(II) reduction. Thus, it is difficult to distinguish ranges of the electrode potential where Ni(II) reduction is controlled by kinetics, mixed kinetics-transport or transport alone. Such information would be useful for the selection of the potentials to apply during the chronoamperometry and EIS experiments and for estimation of the kinetic parameters.

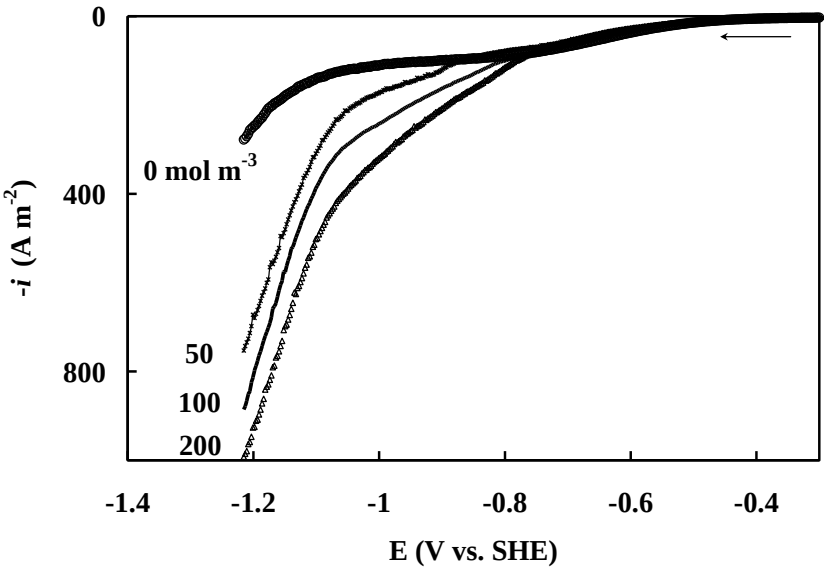

Figure 6.2. Linear voltammograms measured at a sweep rate of 0.05 V s^{-1} on a nickel disk electrode rotating at 1000 rpm in solutions containing 1500 mol m^{-3} Na_2SO_4, 500 mol m^{-3} $B(OH)_3$ and 0, 50, 100 and 200 mol m^{-3} $NiSO_4$ at pH 3.

As this information is not available, potentials (–0.71, –0.76 and –0.81 V) at which the current density is still relatively low were chosen to ensure that Ni(II) reduction would at

least be strongly controlled by electrode kinetics. This range of potentials is slightly more positive than that investigated for cobalt deposition in Chapter 5 since the EIS spectra for the nickel deposition are observed to become more noisy and change their shapes as the potential is made more negative than –0.81 V or so. This finding may reflect the fact that nickel hydroxides or oxides may be precipitating on the surface of the electrode at more negative potentials.

Further support that Ni(II) reduction is strongly controlled by kinetics can be obtained by comparing the current densities at these potentials to the limiting current densities at the corresponding concentrations. Table 6.1 shows the limiting current densities obtained using the Levich equation and a diffusion coefficient of 6.61 $x10^{-10}$ m^2 s^{-1} for Ni(II) [60]. All the measured current densities are significantly lower than the limiting current densities, indicating that mass transport of Ni(II) to the electrode should not be the dominant factor controlling the rate of Ni(II) reduction under these conditions.

Table 6.1. Limiting current density for Ni(II) reduction from the Levich equation using the following parameters: rotational speed = 1000 rpm, $\upsilon = 1 \times 10^{-6}$ m^2 s^{-1} and $D_{Ni(II)} = 6.61 \times 10^{-10}$ m^2 s^{-1} [60].

Ni(II) Concentration (mol m^{-3})	Limiting current density (A m^{-2})
50	-460
100	-930
200	-1860

A comparison of the voltammograms obtained for nickel deposition (Figure 6.2) and those obtained for cobalt deposition (Figure 5.2) reveals that the current measured during Co(II) reduction is always greater than that during Ni(II) reduction at any given potential. The rise in current during the scans is steeper in the case of cobalt deposition than in the case of nickel deposition. This suggests that Co(II) reduction exhibits faster kinetics than that of Ni(II) reduction. Further evidence supporting this behavior comes from analysis of the physicochemical models for both systems, as will be presented later in this Chapter.

As in the case of cobalt deposition, the appearance of a shoulder during the potential scans is evident in Figure 6.2. However, in the case of nickel deposition, this feature appears

at more positive potentials between –1 and –1.1 V (Figure 6.2). Similar to our approach used to investigate the cobalt system, we compared the voltammograms obtained with and without $B(OH)_3$ present to determine whether this shoulder is associated with the HER. Figure 6.3 shows this comparison of the responses obtained in a solution containing 500 mol m^{-3} $B(OH)_3$ to one that is borate-free. At low overpotential, $B(OH)_3$ clearly has no effect on the electrode response; however, at higher overpotential, the presence of boric acid does eventually affect the electrode response by eliminating the shoulder and enabling the current to increase more sharply when the potential reaches ~ –1.06 V, very close to where the shoulder in the linear scans in Figure 6.2 is observed. Not surprising, this effect can be attributed to the buffering effects of boric acid, whereby H^+ is released by the dissociation of $B(OH)_3$ at the surface of the electrode once the surface pH has risen sufficiently. As discussed previously, the rise in surface pH is further accelerated by the onset of water reduction (reaction 5.5).

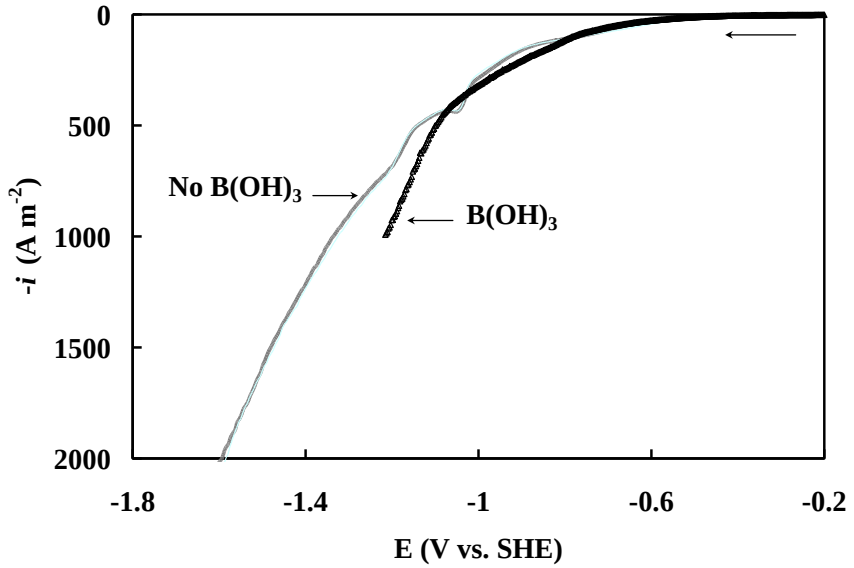

Figure 6.3. Linear voltammograms measured at a sweep rate of 0.05 V s^{-1} on a nickel disk electrode rotating at 1000 rpm in solutions containing 1500 mol m^{-3} Na_2SO_4 and 200 mol m^{-3} $NiSO_4$ at pH 3 in the presence and absence of 500 mol m^{-3} $B(OH)_3$.

It is worth mentioning that the limiting current density for Ni(II) reduction estimated from the Levich equation and shown in Table 6.1 (refer to $NiSO_4$ = 200 mol m^{-3}) is considerably lower than the one obtained for the shoulder shown in Figure 6.3. This tends to

refute the possibility that the shoulder appears due to the onset of mass-transport control for Ni(II) reduction.

6.2.3 Electrochemical impedance spectroscopy.

Figure 6.4 shows the Nyquist diagrams obtained in a solution containing the supporting electrolyte (1500 mol m^{-3} Na_2SO_4 and 500 mol m^{-3} $B(OH)_3$ at pH 3) and Ni(II) concentrations of 0, 100 and 200 mol m^{-3}. The spectra were obtained potentiostatically by applying sinusoidal waves with amplitude of 0.01 V superimposed on a dc potential of a) –0.71, b) -0.76 and c) -0.81 V at frequencies from 100 kHz to 20 mHz. In the cases where Ni(II) is present, two semi-circle loops appear. A general trend evident from the spectra in Figure 6.4a is that the impedance becomes lower as the Ni(II) concentration increases. Also, for every measurement obtained regardless of Ni(II) concentration, the magnitude of the Z' impedance component which is reflective of resistive processes is larger than the magnitude of the –Z" impedance component which is associated with capacitive effects. This finding is consistent with that of a previously reported study on nickel deposition in sulphate solution at pH 3 [64].

Another observation concerning the spectra in Figure 6.4a is that the impedance at high frequencies (i.e., left end of the spectra) becomes independent of Ni(II) concentration and identical to that obtained in a Ni(II)-free solution. As expected, this portion is virtually vertical in the different spectra, indicating that the response at high frequencies is controlled primarily by the solution resistance R_s. The independence of the solution resistance from the Ni(II) concentration is reasonable since Na_2SO_4 and $B(OH)_3$ are by far and away the major components of the electrolyte. The solution resistance is determined to be 1.5 x 10^{-4} ohm m^2 from the intercept of the spectra on the Z′ axis (real component of the impedance) and is the value used in the model throughout this study.

With a further decrease of the frequency, significant differences are observed depending on the Ni(II) concentration, implying that the relaxation during Ni(II) reduction is a significant factor over this range of frequencies. It is also found that an increase of the Ni(II) concentration causes a significant diminution of the second semi-circle loop (low frequencies), but has a much smaller effect on the first loop. This could suggest that the rate-controlling step for Ni(II) reduction is most closely associated with frequencies in the second

loop although this is very difficult to confirm since the simultaneous occurrence of H^+ reduction confounds the electrode response.

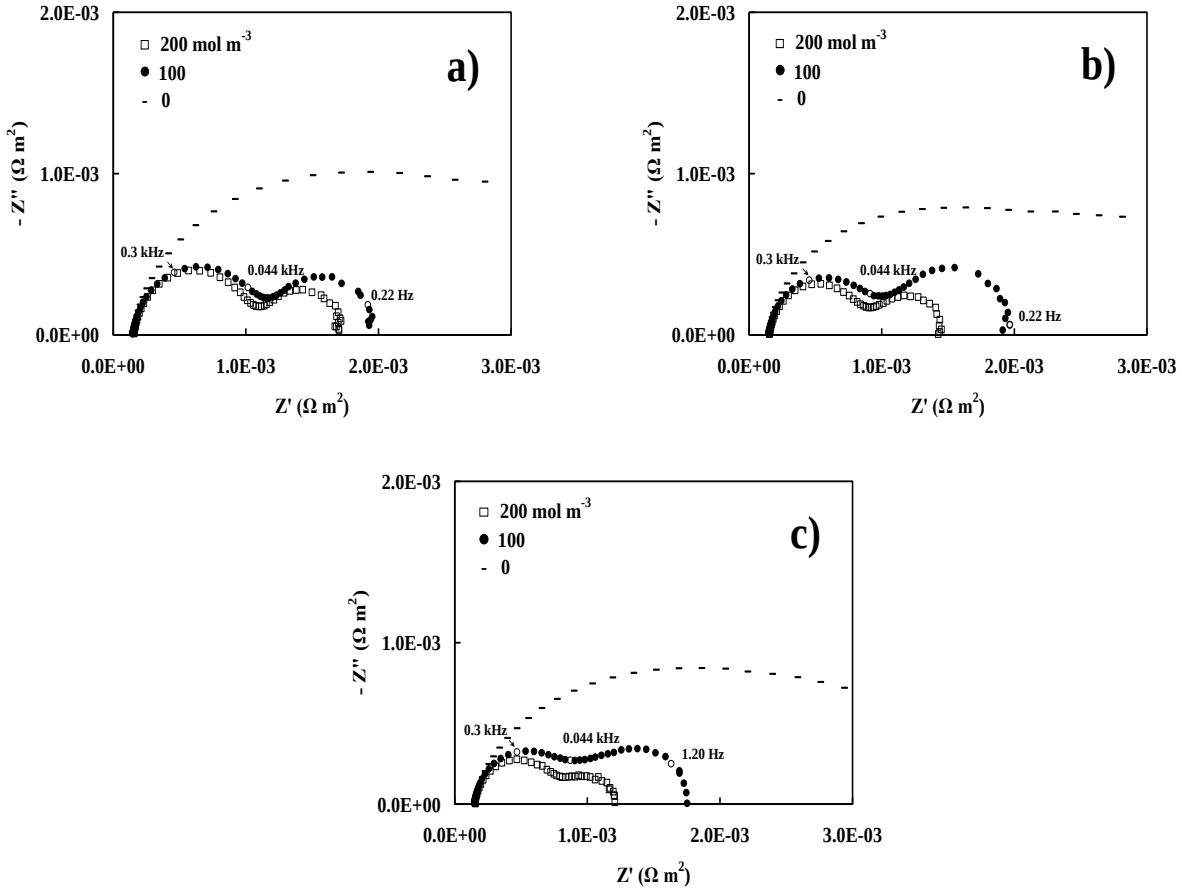

Figure 6.4. Nyquist diagrams obtained at a base potential of a) –0.71, b) -0.76 and c) -0.81 V on a nickel disk rotating at 1000 rpm in 1500 mol m^{-3} Na_2SO_4, 500 mol m^{-3} $B(OH)_3$ solutions at pH 3 containing 0, 100 and 200 mol m^{-3} $NiSO_4$.

Figures 6.4b and 6.4c present the impedance spectra obtained at the same Ni(II) concentrations as in Figure 6.4a, but at the base potentials of –0.76 and –0.81 V, respectively. The same trends evident in Figure 6.4a are observed in these cases as the Ni(II) concentration is increased. As the base potential is made more negative, it has a more significant effect in shrinking the impedance spectra carried out at higher Ni(II) concentrations (see comparisons for 100 and 200 mol m^{-3} in Figures 6.4a and 6.4c, respectively). The electrode potential also has an effect on the relative size of the two impedance loops depending on the Ni(II) concentration. A qualitative comparison of the diagrams in Figure 6.4 with those in Figure 5.4 reveals that the shapes of the spectra are

different from each other. In the case of cobalt deposition, the high frequency loop is generally larger than the lower frequency loop. The size of this latter loop increases as the potential is made more negative. A different trend is observed in the case of nickel deposition, where the two loops tend to be closer in size and have a more flattened shape. Also, both loops shrink as the potential becomes more negative. These variations could reflect changes in the kinetics of the various electrochemical reactions or the rate-controlling steps, reflecting changes in the relative importance of the various steps in the reaction mechanism depending on the potential and concentration.

6.3 Model fitting

The models derived in section 5.3 for the cobalt deposition are used in the current chapter to account for the response of nickel deposition to the EIS and steady-state techniques. The estimation of the kinetic parameters for this model was also carried out using a Matlab® routine to minimize the sum-of-squares error between the experimental data and model predictions obtained by numerical solution of the system using COMSOL Multiphysics® software.

6.3.1 Estimation of the kinetic parameters

Table 5.2 shows the parameters held fixed during the fitting procedure, except for $D_{Ni(II)}$ and D_H. As discussed in the case of the model fitting for cobalt deposition in section 5.4, $D_{Co(II)}$ and D_H were allowed to vary after the best fit values for the kinetic parameters were obtained. In the present analysis of nickel deposition, we follow a different 2-step procedure since the procedure followed in section 5.4 did not produce good fits. In the first step, the model was fit to the experimental data and both the kinetic parameters and diffusion coefficients were allowed to vary. In the second step, $D_{Ni(II)}$ and D_H were fixed at the average values obtained in the first step and only the kinetics parameters were allowed to vary during the fitting. This procedure produced better fits in comparison to those obtained using the procedure adopted in Chapter 5 for cobalt deposition. It should also be noted that it was generally more difficult to attain good fits to the data for nickel than for cobalt deposition. As in the case of the cobalt system, our original intention was to determine one set of kinetic parameters that simultaneously fit the model to all six EIS spectra (see Figure 6.4) obtained

at the different Ni(II) concentrations and base potentials. Repeated attempts to achieve this goal were made by using different initial parameter guesses, search procedures and convergence criteria of the minimization method. Unfortunately, none was able to satisfactorily fit three or more spectra simultaneously with a single set of parameters. Consequently, as in the case of cobalt deposition, we subsequently relaxed the assumption of obtaining a single set of parameters. The values of the kinetic parameters obtained after the second fitting are presented in Table 6.2. The values of C_{dl}, Γ_{Ni} and Γ_{H} (refer to Table 5.2) were held constant at the values obtained in a previous study on nickel deposition since they depend primarily on structural factors and adsorbate-adsorbent interactions [41]. Kinetic parameters for the water reduction (k_{01W}, β_{W}) are not reported in Table 6.2 because the model was found to have little or no sensitivity to their values and so could not be determined with any certainty. A similar situation was found for cobalt deposition (see section 5.4), with the one exception that the model now appears to be somewhat sensitive to the transfer coefficient of the second step of Ni(II) reduction. This observation will be discussed in more detail in section 6.3.3.

Table 6.2. Parameters obtained from the fit of the model to the EIS data at different $NiSO_4$ concentrations using a nickel substrate.

E (V)	[$NiSO_4$] (mol m^{-3})	k_{01Ni} (10^{-8} m s^{-1})	α_{Ni1}	α_{Ni2}	k_{01H} (10^{-9} m s^{-1})	k_{2H} (10^{-2} mol m^{-2} s^{-1})	β_{H}
-0.71	200	2.29	0.17	0.5	1.57	1.70	0.48
	100	1.88	0.20	0.5	1.46	1.80	0.5
-0.76	200	2.30	0.17	0.5	1.84	6.79	0.45
	100	1.74	0.17	0.5	6.13	3.85	0.5
-0.81	200	7.86	0.14	0.47	1.77	2.47	0.5
	100	1.90	0.19	0.47	3.93	2.60	0.49

$k_{01Ni} \approx 10^{-9}$ m^2 s^{-1}, $D_H = 9.18 \times 10^{-9}$ m^2 s^{-1}, $D_{Ni(II)=} = 1.66 \times 10^{-10}$ m^2 s^{-1}

A comparison of the model-fitted and measured EIS spectra obtained at different conditions is presented in Figure 6.5. Particularly good agreement between the model and

experimental data is achieved at the most positive potentials (Figure 6.5a and 6.5b), whereas slight deviations occur at the most negative potentials –0.81 (Figure 6.5c and 6.5d). Although not included here, the fit of the model obtained at 100 mol m^{-3} Ni(II) and lower overpotentials is comparable to those shown in Figure 6.5a and 6.5b. It is worth noting that the experimental spectra obtained at –0.81 V (Figures 6.5c and 6.5d) differs qualitatively from those recorded at –0.71 (Figure 6.5a) and –0.76 V (Figure 6.5b) in that the two loops appear to be merging together. Although not included here, this trend is even more evident in the spectrum when the concentration is lowered further to 50 mol m^{-3} Ni(II). This finding could imply the occurrence of other phenomenon occurring at more negative potentials, i.e. the precipitation of a semi-conductive nickel hydroxide or oxide.

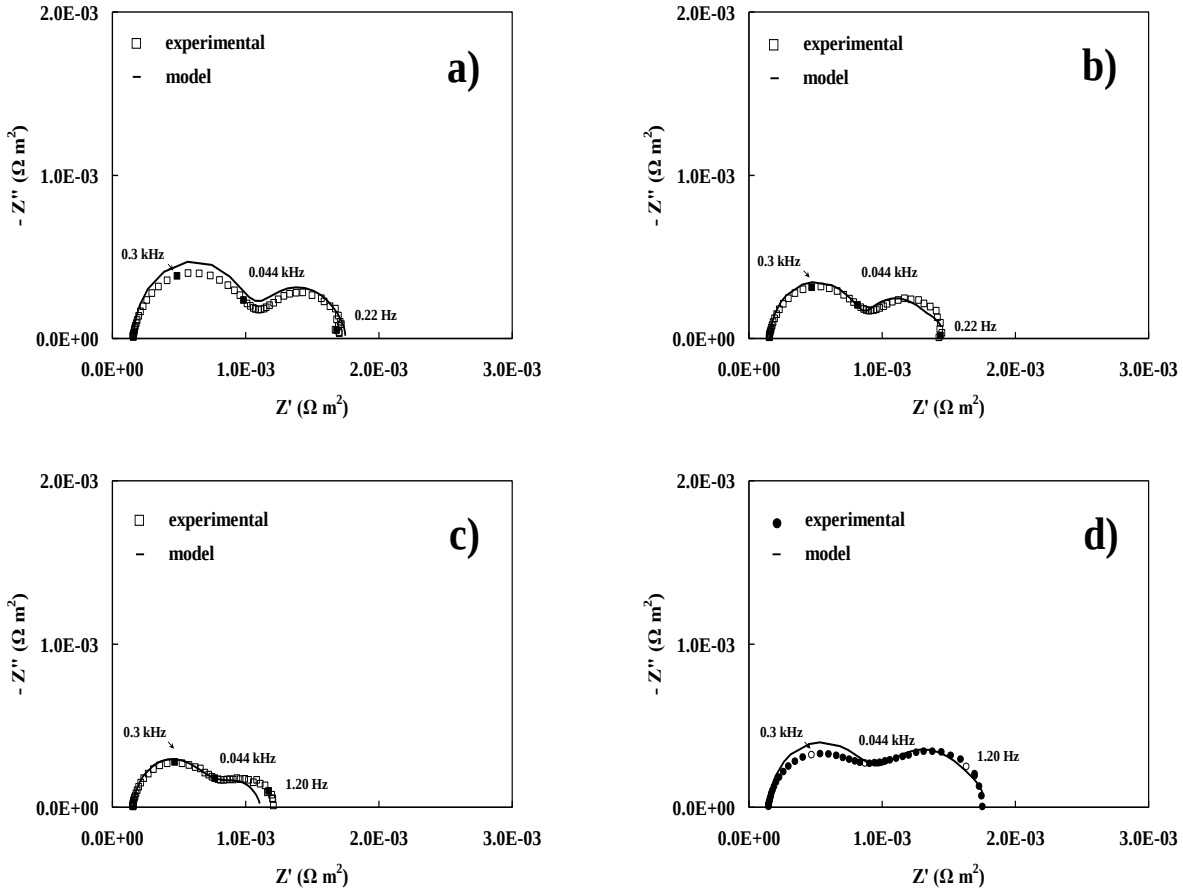

Figure 6.5. Comparison of experimental (symbols) and model-fitted Nyquist diagrams (continuous line) obtained on a cobalt disk rotating at 1000 rpm in solutions at pH 3 containing 1500 mol m^{-3} Na_2SO_4, 500 mol m^{-3} $B(OH)_3$ and a) 200 mol m^{-3} $NiSO_4$ at –0.71 V, b) 200 mol m^{-3} $NiSO_4$ at –0.76 V, c) 200 mol m^{-3} $NiSO_4$ at –0.81 V and d) 100 mol m^{-3} $NiSO_4$ at –0.81 V.

Although a separate set of kinetic parameters was obtained for each experimental condition, the computed impedance was found to be insensitive to a number of the parameters ($k_{02\,Ni}$, $k_{01\,W}$, β_W). Consequently, during the fitting process, the estimate of each of these parameters did not significantly change from iteration to iteration. In the case of the $k_{02\,Ni}$, a reasonable estimate of its value is given in Table 6.2 ($k_{02\,Ni} \approx 10^{-9}$ m^2 s^{-1}) since the model shows some sensitivity to the charge transfer ($\alpha_{Ni\,2}$) associated with the same reaction step. The parameter estimates for the other parameters that are reported in Table 6.2 vary somewhat according to the potential and Ni(II) concentration, but the effect is relatively modest. These parameters are also the ones that most strongly affect the predicted spectra, a result that is not unexpected. Although $\alpha_{Ni\,2}$ was found to be sensitive in the model (unlike $\alpha_{Co\,2}$ in the case of cobalt deposition; refer to section 5.5), its sensitivity is lower than that of $\alpha_{Ni\,1}$ (see Figure 6.9). The observation that $k_{01\,Ni}$ and $\alpha_{Ni\,1}$ vary with experimental conditions is not surprising since it is common for a strong correlation to exist between the fitted parameters appearing in the pre-exponential term and the exponent itself of Arrhenius-type expressions [70]. The insensitivity of the fitting to the values of $k_{01\,W}$ and β_W presumably stems from the fact that water reduction does not occur to any significant extent at the potentials applied during these EIS experiments. Obviously, different experimental conditions are required for these parameters to affect the electrode response more strongly.

Since the values of standard rate constants partially reflect the effects of solvent reorientation on ionic solvation during the charge-transfer process, the observation that they vary with potential and concentration is not unreasonable. A number of studies on this topic have been reported since the seminal theoretical treatment by Marcus on the importance of the metal ion coordination/hydration sphere on electron transfer reactions [71, 75]. Bochmann et al. [67] remarked on the changes in rate constants due to effects related to the nature of the metal and anion adsorption effects. Thus, the potential could also affect standard rate constants due to its effect on anion adsorption on the cathode surface. Bauer [68] concluded that there is no satisfactory theoretical basis to assume that transfer coefficients are independent of the potential. More recently, Sanecki et al. presented kinetic models for several reaction schemes (e.g., E, EC, ECE) that account for the dependence of the transfer coefficient on the potential [76]. The dependence of the measured standard rate

constants and transfer coefficients on the double layer structure has been also recognized and studied by several authors [69, 77, 78]. However, in this study expressions for the standard rate constants and transfer coefficients accounting for these structural changes on the interface as a function of the potential are not considered due to the complexity of the interface.

Following are other observations concerning the parameter values obtained for this model:

1. With one exception, the α_{Ni1} values are always found not to exceed 0.20, indicating a low-intermediate dependence on the applied potential. On the other hand, the transfer coefficients for proton reduction (β_H) and the second step of the nickel reduction (α_{Ni2}) always remain close to 0.5.

2. The values of the rate constants for the first step of nickel deposition (Table 6.2) are of the same order of magnitude as those reported for cobalt deposition (see Table 5.3). However, the transfer coefficients are higher in the case of cobalt deposition. This would explain the higher current density observed in the voltammograms recorded in the presence of $CoSO_4$ (Figure 5.2) in comparison to those obtained in $NiSO_4$ solutions (Figure 6.2) at the same potentials and concentrations.

3. A comparison of the rate constants obtained for H^+ reduction during cobalt (Table 5.3) and nickel (Table 6.2) deposition shows that these parameters are virtually the same for both processes, suggesting that the this reaction is unaffected by the nature of the two metals undergoing deposition.

6.3.2 Comparison of predicted and experimental steady-state polarization curves

Steady-state polarization curves were measured on a nickel electrode in the same supporting electrolyte (1.5 M Na_2SO_4 and 0.5 M $B(OH)_3$ at pH 3) at the different Ni(II) concentrations. These data were obtained by carrying out a series of chronoamperometry experiments at potentials between –0.46 and –0.86 V until steady state was reached. Figure 6.6 shows a plot of the resulting steady-state current densities versus the applied potential at a) 200 and b) 100 mol m^{-3} M Ni(II).

The curves shown in Figure 6.6a resemble those previously reported for Ni(II) reduction in baths at pH 3, but at much higher Ni(II) concentrations ranging from 610 to

1220 mol m^{-3} [44, 45]. As a further check on the validity of the model using the parameters in Table 6.2, we computed steady state current-potential curves for Ni(II) reduction in solutions containing 100 and 200 mol m^{-3} Ni(II) from the model using the parameters in Table 6.2 for comparison with the experimental curves shown in Figure 6.6. As shown in the same Figure, a reasonable agreement between the predicted and measured responses is found in each case.

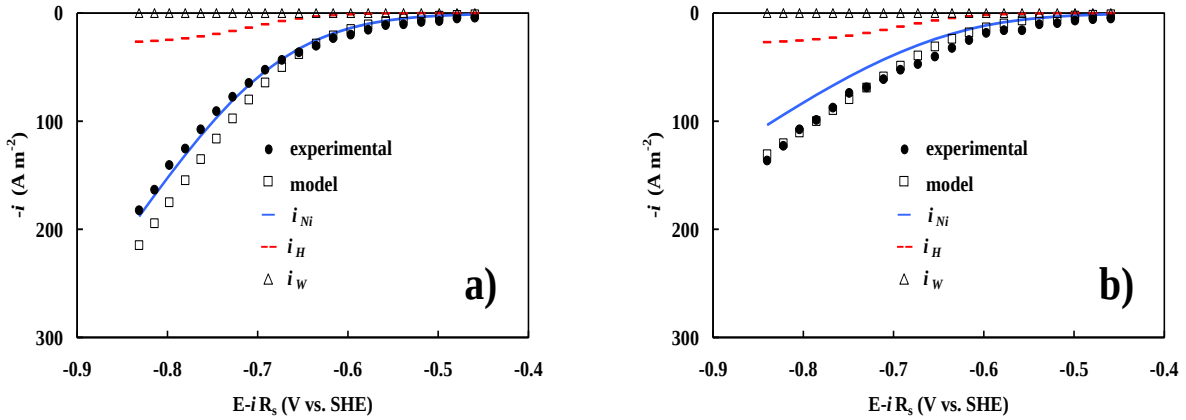

Figure 6.6. Comparison of experimental (black circles) and computed (squares) steady-state polarization curves obtained on a nickel disk rotating at 1000 rpm in solutions at pH 3 containing 1500 mol m^{-3} Na_2SO_4, 500 mol m^{-3} $B(OH)_3$ and a) 200 and b) 100 mol m^{-3} $NiSO_4$. Also shown are the partial current densities for nickel deposition (blue continuous line), H^+ reduction (dashed red continuous line) and water reduction (crossed green continuous line). Curves are generated using parameters listed in Table 6.2.

The model was also used to predict the effect of the potential on several non-measured quantities such as the adsorption density of the $Ni(I)_{ads}$ and H_{ads} intermediates and the surface pH in order to gain further insight into the reaction mechanism. The variation of the interfacial pH with potential under steady state conditions over the range from –0.46 V to –0.86 V at the two Ni(II) concentrations is shown in Figure 6.7. Figure 6.8 shows the effect of potential on the $Ni(I)_{ads}$ and H_{ads} adsorption densities.

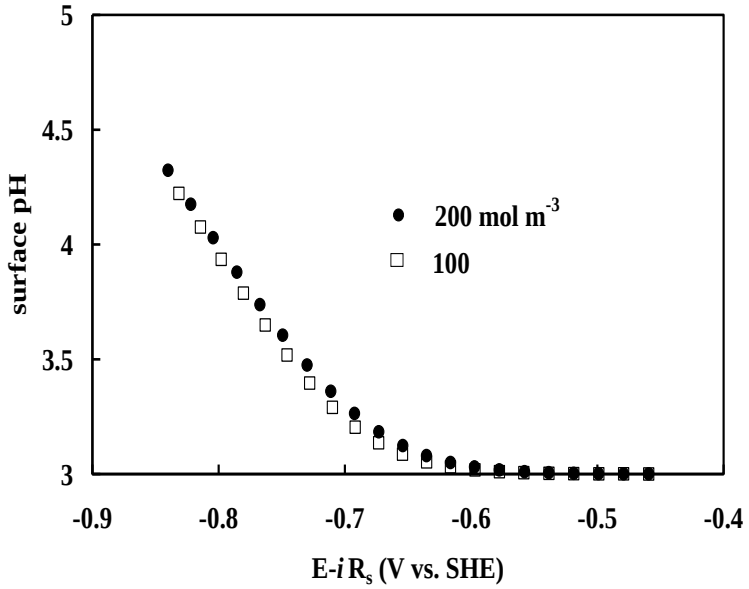

Figure 6.7. Variation of the computed steady state interfacial pH with potential on a nickel disk rotating at 1000 rpm in the presence of 1500 mol m^{-3} Na_2SO_4, 500 mol m^{-3} $B(OH)_3$ and 200 or 100 mol m^{-3} $NiSO_4$ at pH 3. Curves are generated using parameters listed in Table 6.2.

The results in Figure 6.7 show that the interfacial pH increases from 3 to ~4.3 as the electrode potential decreases from –0.46 V to –0.86 V due to the effect of the HER in depleting H^+ at the cathode. These values are somewhat similar to those reported in Figure 5.11 during cobalt deposition, suggesting that the HER proceeds under similar rates in the single cobalt and nickel deposition. On the other hand, the effect of potential on the surface pH shown in Figure 6.7 is different from that obtained during an earlier reported analysis of nickel deposition with a more simplified model in which the buffering effects of $B(OH)_3$ were not taken into account [41]. In this previous study, a linear variation in surface pH 3 to 7 over the same potential range was reported. Undoubtedly, the much higher surface pH predicted in this earlier study is due to the neglect of the homogeneous reactions (i.e. Table 5.1) in the model, which act to mitigate the rise in pH due to the HER.

The results in Figure 6.8 reveal that θ_{Ni} declines as the potential becomes more negative, consistent with the first step of Ni(II) reduction (i.e., reaction (6.1)) becoming increasingly rate-limiting as the overpotential increases. Thus, virtually all $Ni(I)_{ads}$ sites formed are rapidly converted to metallic nickel by the second step (i.e. reaction (6.2)). However, the consumption of Ni(II) species by reaction (6.1) is not as fast as the depletion of

Co(II) species by reaction (5.1), since at the same potential θ_{Co} is significantly lower than θ_{Ni}. H^+ reduction is found not to be controlled exclusively by either its first step or second step, similar to that observed for cobalt deposition.

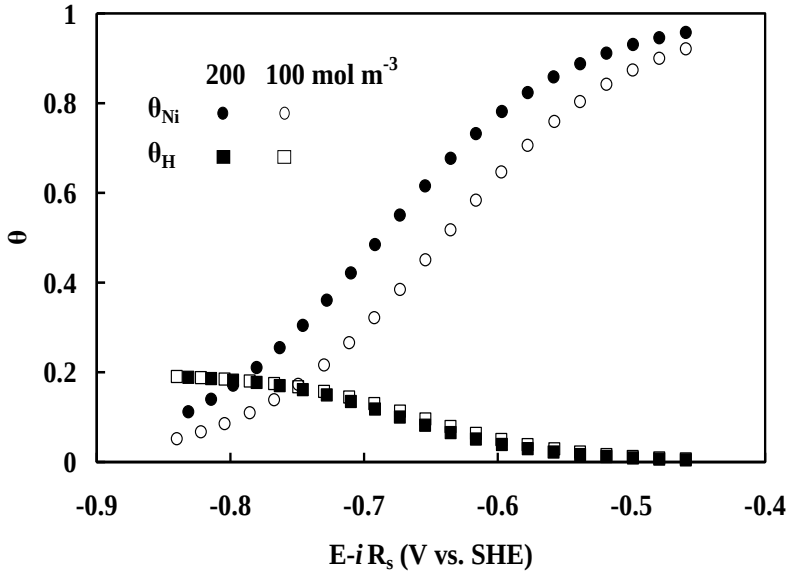

Figure 6.8. Variation of the computed steady state fractional coverages of H_{ads} and $Ni(I)_{ads}$ with potential on a nickel disk rotating at 1000 rpm in the presence of 1500 mol m^{-3} Na_2SO_4, 500 mol m^{-3} $B(OH)_3$ and 200 or 100 mol m^{-3} $NiSO_4$ at pH 3. Curves are generated using parameters listed in Table 6.2.

6.3.3 Sensitivity analysis

If a reaction step is rate-controlling, then the electrode response will be sensitive to changes in variables or parameters associated with this step. On the other hand, if a step does not control the rate, then the electrode response will be insensitive to changes associated with this step. To explore this aspect of the current system, simulations were carried out by varying one parameter at a time, while keeping the others fixed at the values obtained from our model fitting. Figure 6.9 shows the results of this analysis for conditions of –0.71 V and 200 mol m^{-3} $NiSO_4$ (Figure 6.9a-d) and –0.81 V and 100 mol m^{-3} $NiSO_4$ (Figure 6.9e-f). In each case, the sensitivity of the impedance response was determined by decreasing a parameter by 5 % from its previously determined value (Table 6.2), with the others kept fixed.

The sensitivity analysis clearly shows that the change to α_{Ni1} (Figure 6.9a) strongly affect both loops of the computed spectra whereas the change to α_{Ni2} (Figure 6.9b) affects the high frequency loop similarly, but has little effect on the low frequency loop. On the other hand, changes to β_W and k_W (not shown here) have no effect whatsoever under any of the conditions considered. As discussed in Chapter 5 (section 5.5), the rate-controlling step of cobalt deposition is reaction (5.1). However, in the case of nickel deposition, the results presented here are not as clear-cut since the model shows some sensitivity to α_{Ni2} (Figure 6.9b) although the computed electrode responses are affected more strongly by changes to α_{Ni1} (Figure 6.9a). This difference in the two systems may arise from the fact that the sensitivity analysis in the case of nickel deposition has been carried out at more positive potentials (-0.71 V) than for cobalt deposition (-0.86 V, see Figure 5.13). Since satisfactory EIS measurements for nickel deposition could not be carried out at more negative potentials than -0.81 V due to the formation of nickel hydroxides on the electrode, a second sensitivity analysis was carried out at –0.81 V and 100 mol m^{-3} $NiSO_4$ instead (Figure 6.9e-f). As observed in Figure 6.9f, the sensitivity of the computed spectrum to α_{Ni2} decreases significantly at this potential, whereas the sensitivity to α_{Ni1} increases. These trends are consistent with reaction (6.1) becoming progressively more rate-controlling as the potential is made more negative. This result is consistent with the results of the previous section (6.3.2) showing that θ_{Ni} is close to 1.0 at the more positive potentials considered and eventually decreases to ~0.1 as the potential becomes more negative (Figure 6.9b). It also agrees with trends reported for the deposition of other metals [44, 45].

The situation with regard to the HER is similar. The spectra appear to be moderately sensitive to changes to both β_H associated with the first step (Figure 6.9c) and k_{2H} associated with the second step (Figure 6.9d). On the other hand, the model shows much less sensitivity to k_{01H} (not shown). Also, the fractional coverage of H_{ads} species on the electrode surface remains relatively low ($\theta_H \approx 0.2$) at all potentials and Ni(II) concentrations considered in this study, suggesting that the second step of the HER also influences the reaction rate. Thus, the assumption that the HER proceeds as a single 2-electron step, as previously made for other experimental conditions [42, 47, 49], does not appear to be justified for the conditions of this study.

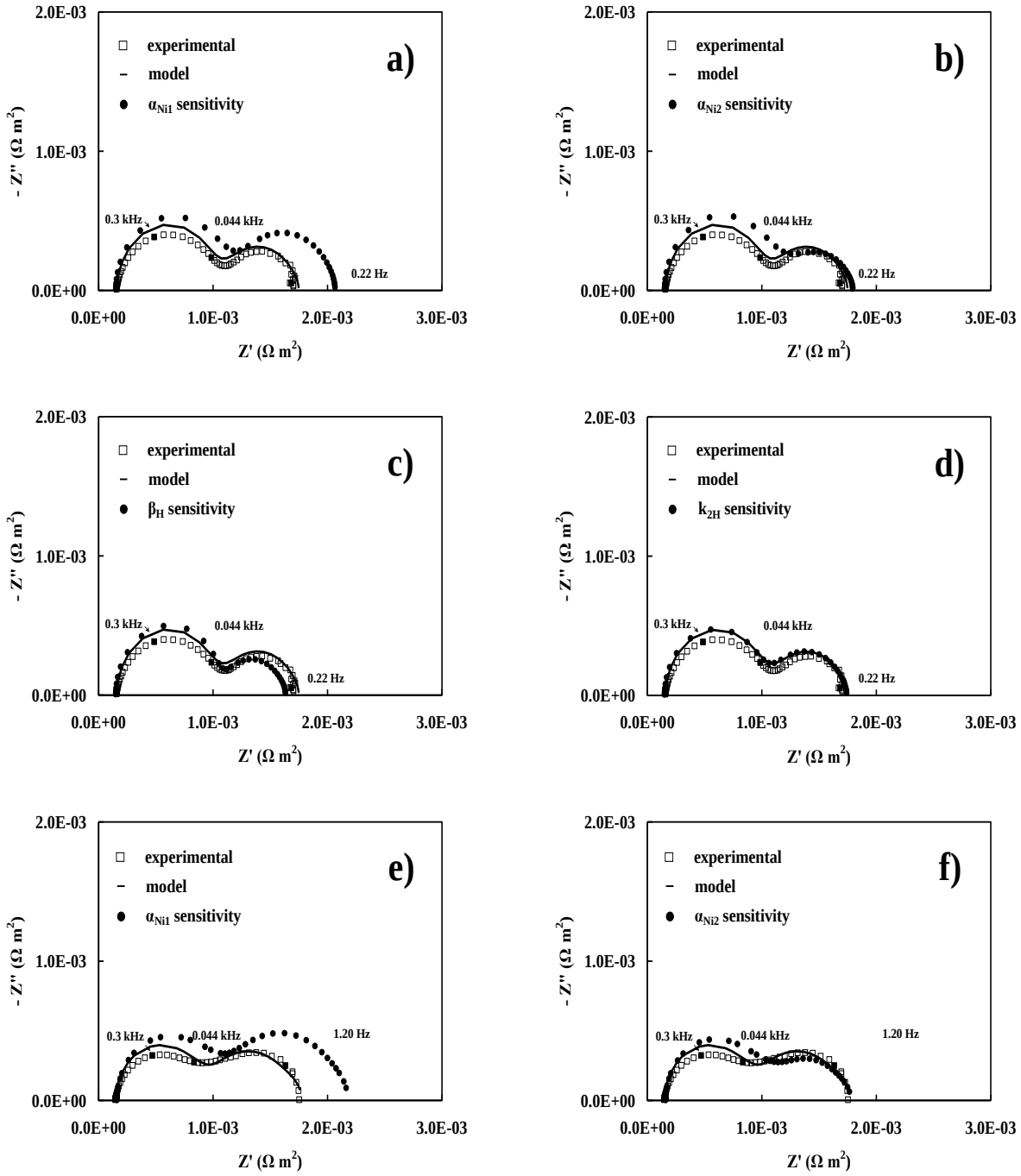

Figure 6.9. Sensitivity analysis performed by computing the effect of decreasing each of the following parameters by 5 %: a) α_{Ni1}, b) α_{Ni2}, c) β_H and d) k_{2H} (black circle) at a base potential –0.71 V and 200 mol m^{-3} $NiSO_4$; and e) α_{Ni1}, f) α_{Ni2} at a base potential –0.81 V and 100 mol m^{-3} $NiSO_4$. Original fitted model (continuous line) and experimental data (squares) are included for comparison.

Chapter 7 Model for LSV Response During Nickel Deposition

7.1 Introduction

In chapter 6, we employed EIS to analyze the dynamics of Ni(II) reduction accounting for the role of the HER. Although EIS is a very effective technique to analyze the dynamics of a complex system such as this one, experimental difficulties at high overpotentials can be experienced due to the formation of bubbles and other interfacial phenomena that cause considerable noise in the electrode response. This is a particular problem at low frequencies where a considerable time is required for the response to stabilize. Not only does this interfere with the measurement of the dynamic response to the imposed signal but it also make it virtually impossible to return to the original steady-state condition before a new frequency is applied. Although linear sweep voltammetry is generally not as sensitive as EIS, it is also less affected by the interferences encountered at higher overpotentials. Therefore, in this chapter, nickel deposition over a wider range of potentials than in the previous chapter is analyzed by means of linear sweep voltammetry. The experiments are conducted on rotating disk working electrodes at several $NiSO_4$ concentrations and scan rates on two different substrates (nickel and copper). The transient model derived in section 5.3 is fit (least-square) to the experimental LSV data in order to estimate the kinetic parameters for the proposed mechanism.

7.2 Results

Figure 7.1 shows linear voltammograms obtained at scan rates of 0.1, 0.05 and 0.005 V s^{-1} on a nickel substrate rotating at 1000 rpm in a solution containing 1500 mol m^{-3} Na_2SO_4, 500 mol m^{-3} $B(OH)_3$ and 200 mol m^{-3} $NiSO_4$ at pH 3. In each case, the scan proceeded from the open circuit potential (OCP) in the negative direction. Interestingly, the scan rate has very little influence on the current density obtained during the reduction processes despite the relatively wide range considered. This observation indicates that the reduction reactions can keep pace with the rate of change of the electrode potential, presumably due to relatively fast kinetics. In such a situation, mass transport effects will

Adapted from J. Vazquez-Arenas, L. Altamirano-Garcia, M. Pritzker, R. Luna-Sanchez and R. Cabrera-Sierra, "Experimental and Modeling Study of Nickel Electrodeposition Including H^+ and Water Reduction and Homogeneous Reactions", Journal of Electrochem. Soc., 158, (2011) D33-D41.

likely play an important role in the electrode response [59]. Important features appearing on these curves are shoulders suggesting that more than one electron transfer reaction occurs over the course of the scans. Deposition of nickel has also been carried out on a copper substrate and also reveals the electrode response not to be strongly influenced by the scan rate (Figure 7.2). Some difference is observed in the potential range from –0.7 to –1.0 V where the current levels off to a more well-defined shoulder when the scan rate is raised to 0.1 V s^{-1}.

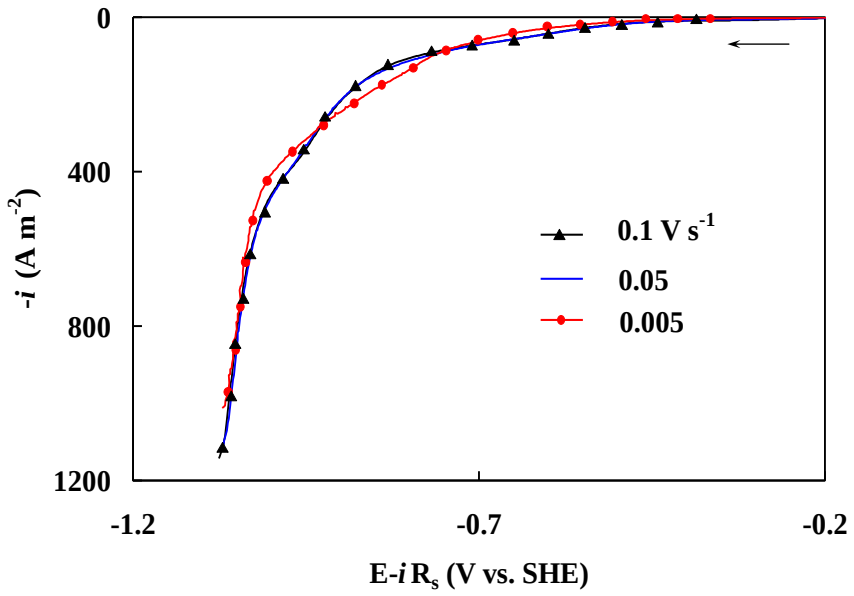

Figure 7.1. Linear voltammograms measured at different sweep rates on a nickel disk electrode rotating at 1000 rpm in solutions containing 1500 mol m^{-3} Na_2SO_4, 500 mol m^{-3} $B(OH)_3$ and 200 mol m^{-3} $NiSO_4$ at pH 3.

Figure 7.3 shows a comparison of two linear sweep voltammograms obtained on nickel and copper substrates at 200 (Figure 7.3a) and 400 mol m^{-3} (Figure 7.3b) $NiSO_4$ concentrations with the same supporting electrolyte (1500 mol m^{-3} Na_2SO_4 and 500 mol m^{-3} $B(OH)_3$ at pH 3). The scans obtained in the presence of the supporting electrolyte (SE) alone without $NiSO_4$ are also included in the insets for comparison. Comparison of the two sets of curves shows that similar trends are observed when the concentration is raised to 400 mol m^{-3} $NiSO_4$. In order to more fully explore the electrode response particularly at low overpotentials, the effect of $NiSO_4$ concentration on the potential scans is examined in closer detail.

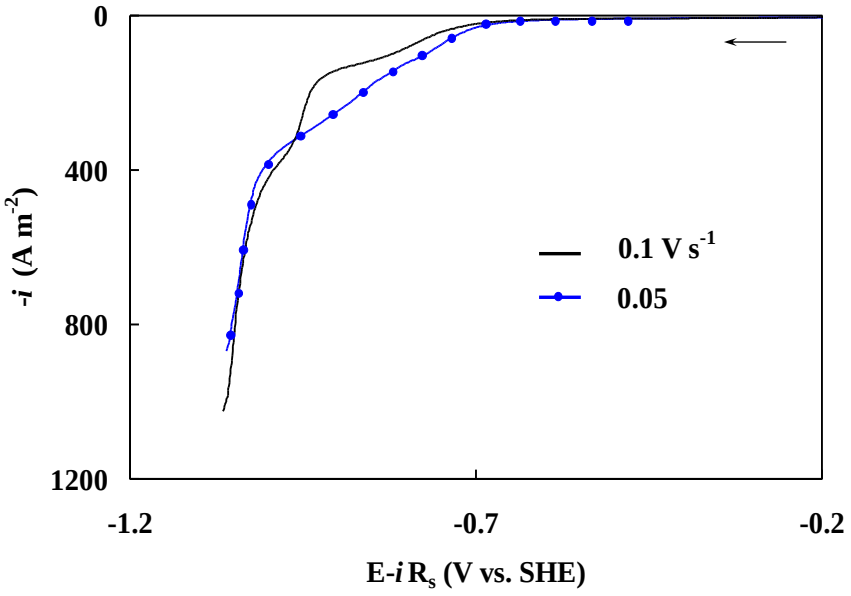

Figure 7.2. Linear voltammograms measured at different sweep rates on a copper disk electrode rotating at 1000 rpm in solutions containing 1500 mol m^{-3} Na_2SO_4, 500 mol m^{-3} $B(OH)_3$ and 200 mol m^{-3} $NiSO_4$ at pH 3.

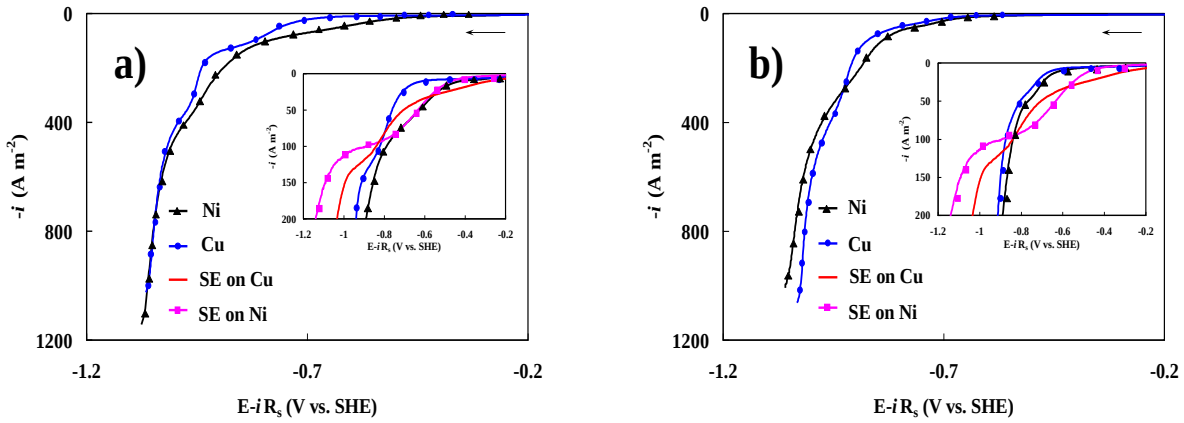

Figure 7.3. Linear voltammograms measured at 0.1 V s^{-1} on nickel and copper disk electrodes rotating at 1000 rpm in solutions containing 1500 mol m^{-3} Na_2SO_4, 500 mol m^{-3} $B(OH)_3$ (SE) and a) 200 or b) 400 mol m^{-3} $NiSO_4$ at pH 3. The insets show the curves obtained in the absence and presence of $NiSO_4$ that are expanded in the lower current region.

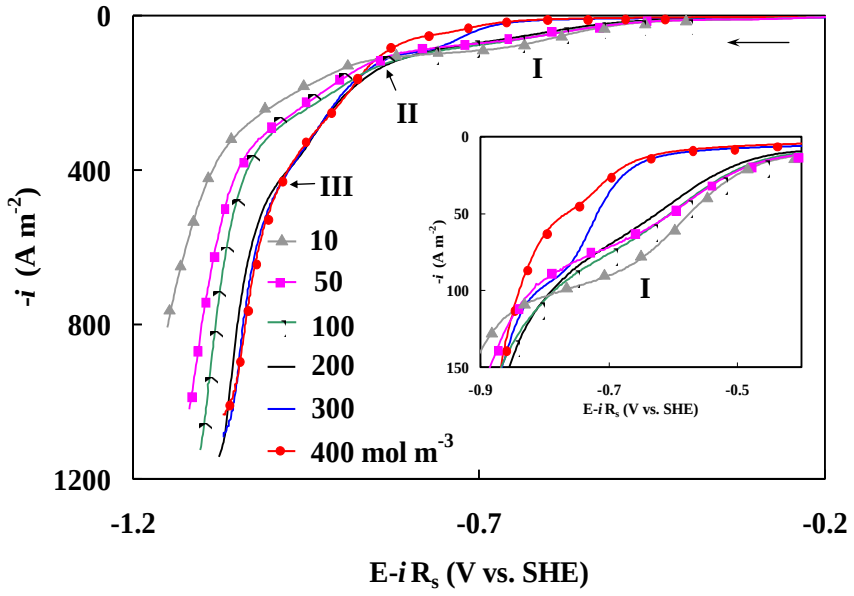

Figure 7.4. Linear voltammograms measured at different $NiSO_4$ concentrations (labeled) on a nickel disk electrode rotating at 1000 rpm in solutions containing 1500 mol m^{-3} Na_2SO_4 and 500 mol m^{-3} $B(OH)_3$ at pH 3. The inset shows an expanded view of the curves in the lower current region.

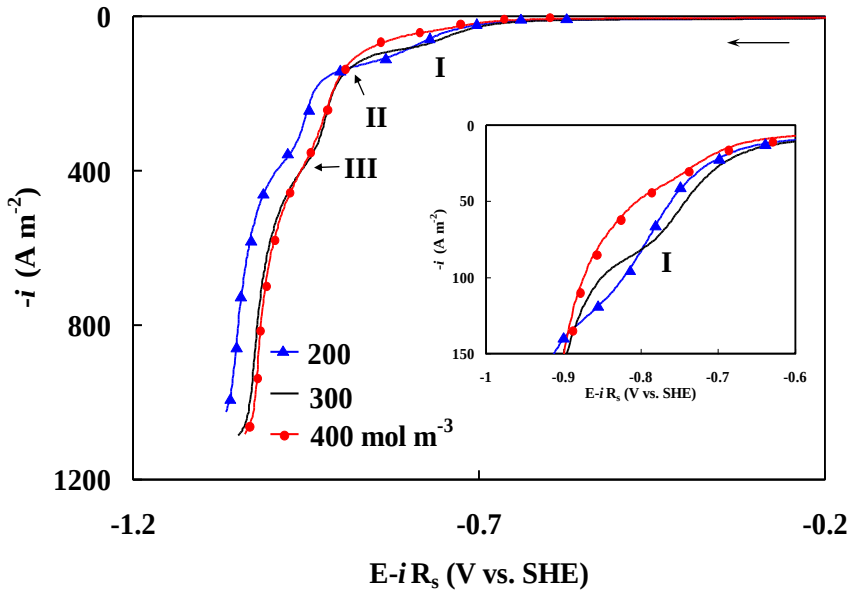

Figure 7.5. Linear voltammograms measured at different $NiSO_4$ concentrations (labeled) on a copper disk electrode rotating at 1000 rpm in solutions containing 1500 mol m^{-3} Na_2SO_4 and 500 mol m^{-3} $B(OH)_3$ at pH 3. The inset shows an expanded view of the curves in the lower current region.

Figure 7.4 presents the scans obtained at more $NiSO_4$ concentrations in the range from 10 to 400 mol m^{-3} on a nickel substrate. Scans obtained on a copper electrode are presented in Figure 7.5. Plateaus or shoulders appear in these curves and lead to three current rise regions labelled as I, II and III. Regardless of the substrate, the current rise in region I which appears at the lowest overpotential becomes more suppressed as the $NiSO_4$ concentration rises. Such a trend is particularly obvious when deposition is carried out on nickel (inset to Figure 7.4). Region I cannot be reasonably ascribed to Ni(II) reduction since this would require it to become more prominent as the $NiSO_4$ concentration increases. Instead, it is assigned to H^+ reduction (reactions 5.3 and 5.4) which has a more positive Nernst potential than does Ni(II) reduction. This conclusion is also supported by the fact that region I also appears in the scans obtained in the absence of Ni(II) (insets to Figures 7.3a and 7.3b).

The effect of Ni(II) on H^+ reduction can be clearly seen by comparing the scans in the insets of Figures 7.3a and 7.3b obtained on a nickel surface depending on whether or not Ni(II) is present in solution. The current obtained in a 200 mol m^{-3} $NiSO_4$ solution is virtually identical to the current obtained in the absence of Ni(II) throughout region I up to a potential of about –0.8 V, indicating that H^+ reduction is unaffected under these conditions. However, when the $NiSO_4$ concentration is raised to 400 mol m^{-3}, the current in region I is greatly suppressed (Figure 7.3b). The curves in the inset to Figure 7.4 show that this process is strongly inhibited even when the $NiSO_4$ concentration has reached 300 mol m^{-3}. Presumably, the $Ni(I)_{ads}$ intermediate out-competes H_{ads} species for available sites on the electrode surface at these higher $NiSO_4$ concentrations. Furthermore, the results reveal that this effect of Ni(II) is affected by the nature of the substrate. As shown in the insets to Figures 7.3a and 7.3b, the presence of 200 mol m^{-3} Ni(II) is sufficient to strongly inhibit H^+ reduction when it is carried out on a copper electrode. An explanation for this difference becomes evident upon comparison of the curves obtained on the two substrates in the absence of Ni(II) (Figure 7.3). Although the current measured on a nickel surface is lower at the start of the scan, its rises more steeply with potential and becomes larger when the potential reaches –0.6 V, indicating that nickel is a better catalyst for H^+ reduction than copper. This observation is not surprising since a nickel surface is well known to be a good catalyst for this reaction [48].

Once the potential is decreased to about −0.85 V during the scans, the magnitude of the current becomes much more sensitive to the $NiSO_4$ concentration and increases as the concentration rises, unlike the situation at lower overpotentials (Figures 7.4 and 7.5). This effect is particularly strong at lower $NiSO_4$ concentration. However, once a 300 mol m^{-3} concentration is reached, the amount of $NiSO_4$ present no longer has an effect on the current in this region. The current wave in this region denoted as II is attributed to Ni(II) reduction. It is interesting to note from comparison of Figures 7.4 and 7.5 that the current rise in region II is steeper on a copper substrate than a nickel surface.

As the scan proceeds further, the current density rises even more steeply well above the limiting current values for both H^+ and Ni(II) reduction. This transition is marked by another inflection point that reflects the onset of water reduction (reactions 5.4 and 5.5) and region III. Region III is found to begin when the current density reaches approximately 400 A m^{-2} regardless of the conditions whereas the potential for its onset varies depends on the $NiSO_4$ concentration. Since water reduction does not become mass–transport controlled, the current continues to rise steeply until the end of the scan.

7.3 Model fitting and discussion

A comparison between the model-fitted and experimental voltammograms at concentrations of 200, 100, 50 and 10 mol m^{-3} $NiSO_4$ is shown in Figures 7.6 – 7.9, respectively. Each scan proceeds from the OCP to the same final potential of −1.08 V. During the fitting procedure, the parameters shown in Table 5.2 were held fixed. Preliminary analysis showed that the fitted value of C_{dl} always remained very close to 0.65 F m^{-2} regardless of the conditions, similar to what was obtained from the EIS analysis of the nickel deposition (see Table 5.2). Consequently, C_{dl} was kept fixed at this value during the fitting for the other parameters. The fitting of the model to the experimental data yields the parameter estimates reported on Table 7.1. As observed in Figures 7.6–7.9, good agreement between the fitted and experimental LSV curves is achieved at the four $NiSO_4$ concentrations. The original intention was to fit the model simultaneously to the four LSV curves to obtain a single set of kinetic parameters. Numerous attempts to achieve this goal were made (e.g., use of lower tolerances and different search methods), but none succeeded. A single set of parameters can yield a good fit of the model to the experimental data at the two highest $NiSO_4$ concentrations, but the agreement becomes much poorer when the experimental data for 10 mol m^{-3} are included.

The best results are obtained by fitting the model separately for each experiment. As reported in chapters 5 and 6 on nickel and cobalt deposition, the same result is obtained when fitting similar models to EIS spectra.

Table 7.1. Kinetic parameters obtained from fitting the model to experimental LSV data at different $NiSO_4$ concentrations using a nickel substrate.*

$[NiSO_4]$(mol m^{-3})	k_{01Ni} (10^{-10} m s^{-1})	α_{Ni1}	k_{01H} (10^{-9} m s^{-1})	k_{2H} (10^{-2} mol m^{-2} s^{-1})	β_H	k_{0W} (10^{-12} mol m^{-2} s^{-1})	β_W
200	3.61	0.28	1.12	1.22	0.5	2.66	0.5
100	5.07	0.28	1.20	0.96	0.5	3.53	0.5
50	5.22	0.30	1.02	1.06	0.5	2.38	0.5
10	7.76	0.47	1.91	0.47	0.5	5.77	0.5

* C_{dl} 0.65 F m^{-2}

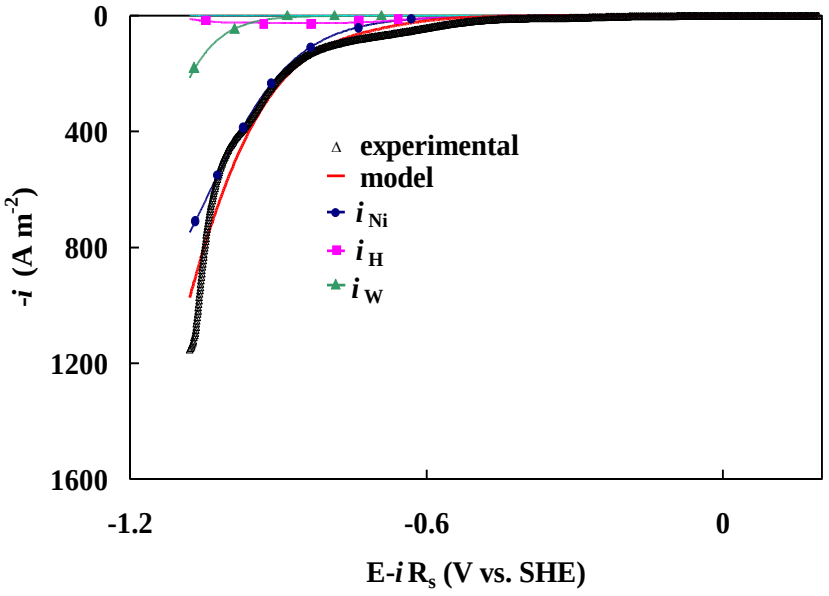

Figure 7.6. Model-fitted (red continuous line) and experimental linear voltammograms (triangles) measured at 0.1 mV s^{-1} on a nickel disk electrode rotating at 1000 rpm in solutions containing 1500 mol m^{-3} Na_2SO_4, 500 mol m^{-3} $B(OH)_3$ and 200 mol m^{-3} $NiSO_4$ at pH 3. Also shown are the computed partial current densities i_{Ni} (blue continuous line), i_H (magenta continuous line) and i_W (green continuous line). Computed curves are generated using parameters listed in Tables 5.2 and 7.1.

On the other hand, all steady state polarization curves for each metal system over the range of dissolved metal concentrations from 10 mol m^{-3} to 200 mol m^{-3} could be fit with a single set of kinetic parameters. This difference is partly due to the fact that transient techniques such as EIS (in particular) and LSV are inherently more sensitive for investigating electrode responses than steady state methods.

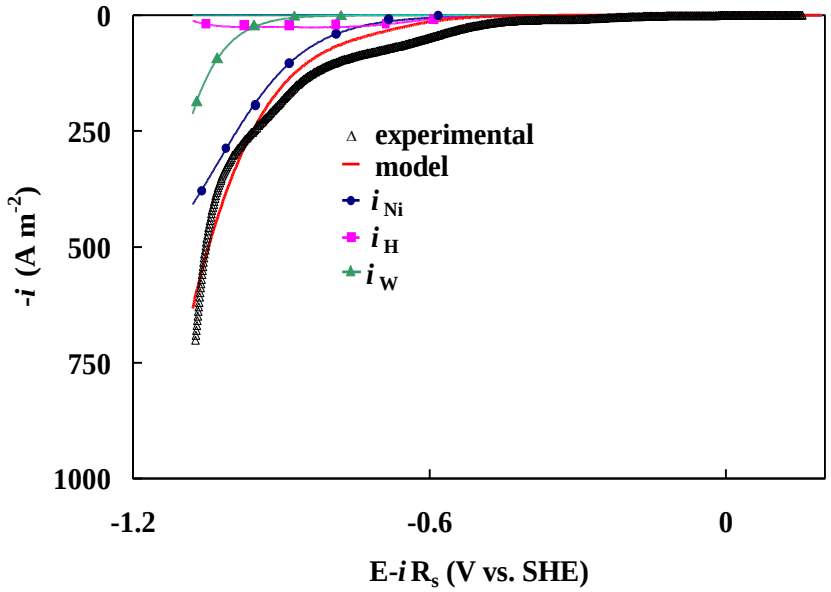

Figure 7.7. Model-fitted (red continuous line) and experimental linear voltammograms (triangles) measured at 0.1 mV s^{-1} on a nickel disk electrode rotating at 1000 rpm in solutions containing 1500 mol m^{-3} Na_2SO_4, 500 mol m^{-3} $B(OH)_3$ and 100 mol m^{-3} $NiSO_4$ at pH 3. Also shown are the computed partial current densities i_{Ni} (blue continuous line), i_H (magenta continuous line) and i_W (green continuous line). Computed curves are generated using parameters listed in Tables 5.2 and 7.1.

The model was also fit to the experimental LSV curves obtained on a copper working electrode to examine the influence of substrate on the kinetics of nickel deposition. As shown in Table 7.2, the parameter values obtained in a solution containing 200 mol m^{-3} $NiSO_4$ are essentially identical to those obtained under the same conditions on a nickel substrate (Table 7.1). The absence of an effect could be partly due to the fact that the substrates are already covered by a nickel deposit during a large portion of the scans.

Table 7.2. Kinetic parameters obtained from fitting the model to experimental LSV data at different $NiSO_4$ concentrations using a copper substrate.*

$[NiSO_4]$ (mol m^{-3})	k_{01Ni} (10^{-10} m s^{-1})	α_{Ni1}	k_{01H} (10^{-9} m s^{-1})	k_{2H} (10^{-2} mol m^{-2} s^{-1})	β_H	k_{0W} (10^{-12} mol m^{-2} s^{-1})	β_W
200	3.61	0.28	1.12	1.23	0.5	2.67	0.5

* C_{dl} 0.65 F m^{-2}

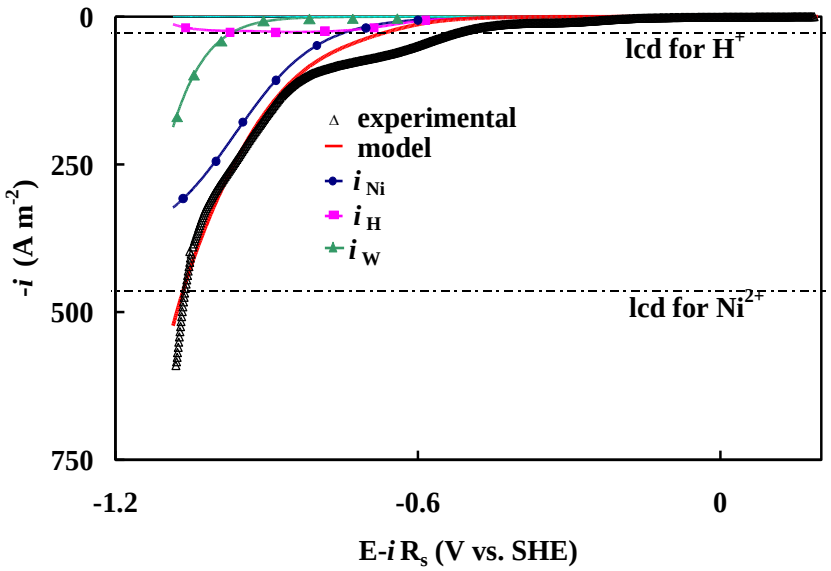

Figure 7.8. Model-fitted (red continuous line) and experimental linear voltammograms (triangle) measured at 0.1 V s^{-1} on a nickel disk electrode rotating at 1000 rpm in solutions containing 1500 mol m^{-3} Na_2SO_4, 500 mol m^{-3} $B(OH)_3$ and 50 mol m^{-3} $NiSO_4$ at pH 3. Also shown are the computed partial current densities i_{Ni} (blue continuous line), i_H (magenta continuous line) and i_W (green continuous line). Computed curves are generated using parameters listed in Tables 5.2 and 7.1.

As shown in chapters 5 and 6, very small changes in some kinetic parameters can significantly alter the model-predicted EIS spectra. A sensitivity analysis (not shown) was conducted to evaluate the rate-controlling step and the certainty of the kinetic parameters reported in Table 7.1 at $NiSO_4$ concentrations of 200 and 10 mol m^{-3}. During this evaluation, one kinetic parameter at a time was decreased by 5 % from its value obtained from the fitting procedure, while the other parameters were fixed at their best-fit levels. Results from this

analysis showed that the model is most sensitive to the transfer coefficient $\alpha_{Ni\,1}$ of the first step of nickel deposition, followed by the transfer coefficients β_W and β_H for water and H^+ reduction. The model is also somewhat sensitive to the rate constants for H^+ and water reduction, including the second step of H^+ reduction (i.e., reaction 5.4). Unlike Ni(II) reduction where the first step is clearly rate-determining, the rate of H^+ reduction appears to be sensitive to the rates of both of its steps. The findings concerning the rate-determining steps for Ni(II) and H^+ reduction are similar to those obtained in Chapter 6 for the EIS studies on nickel deposition. However, on the basis of the LSV technique the second step (i.e. the parameter $\alpha_{Ni\,2}$) is not found to be as sensitive as indicated using the EIS analysis. This could be due to the fact that the LSV scans in this study extend to more negative potentials than those applied during the EIS experiments. As observed from Figure 6.8, the first step of Ni(II) reduction (i.e., reaction (6.1)) becomes increasingly rate-limiting as the overpotential increases.

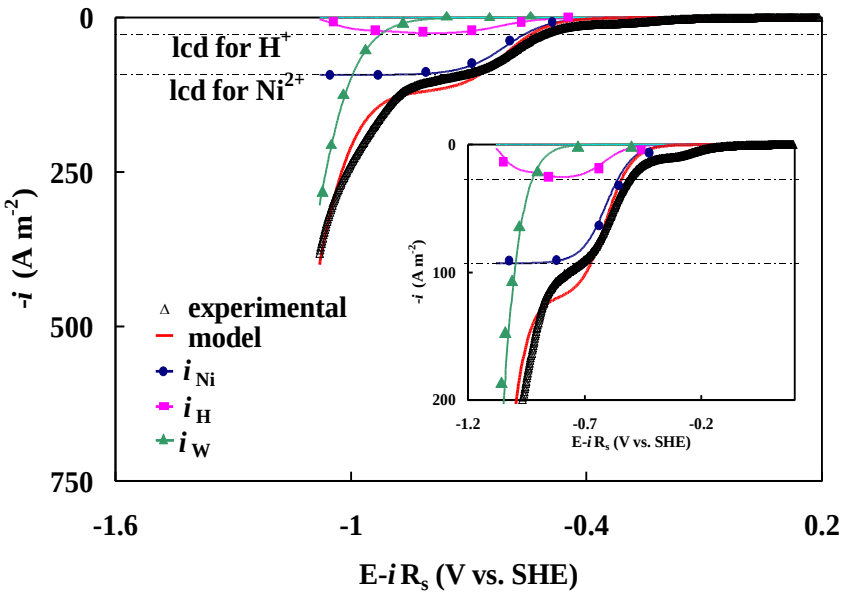

Figure 7.9. Model-fitted (red continuous line) and experimental linear voltammograms (triangle) measured at 0.1 V s^{-1} on a nickel disk electrode rotated at 1000 rpm in solutions containing 1500 mol m^{-3} Na_2SO_4, 500 mol m^{-3} $B(OH)_3$ and 10 mol m^{-3} $NiSO_4$ at pH 3. Also shown are the computed partial current densities i_{Ni} (blue continuous line), i_H (magenta continuous line) and i_W (green continuous line). Computed curves are generated using parameters listed in Tables 5.2 and 7.1.

The results shown in Figures 7.6 – 7.9 indicate that i_W begins to become significant only at potentials between –0.9 and –1.0 V during the scans in the case of nickel deposition. The sensitivity analysis, however, indicates that once water reduction begins, the value of β_W has a very strong influence on the computed electrode response and, in fact, more than does β_H, particularly at lower $NiSO_4$ concentrations. This is not surprising since H^+ reduction is already mass transfer-limited and so not influenced by kinetic factors during a large portion of the scan.

As shown in Table 7.1, the sets of parameters obtained for 200, 100 and 50 mol m^{-3} $NiSO_4$ are reasonably close to one another, but differ somewhat from those for 10 mol m^{-3}, particularly α_{Ni1}. It is interesting to note that it is the influence of α_{Ni1} that mainly prevents all the LSV curves being fit with a single set of kinetic parameters. Since a decrease of the parameters associated with the second step of Ni(II) reduction by 5% has no noticeable effect on the shape of the LSV (not shown here), the estimates of these values are known with much less certainty than the others and so are not reported in Table 7.1. This lower sensitivity stems from the fact that the second step has much more facile kinetics than the first step and so does not influence the rate of Ni(II) reduction and the electrode response. The concentration and potential dependence of the kinetic parameters suggests that the model in its present form is not entirely complete and does not explicitly capture all aspects of the electrode response during nickel deposition. Based on previous findings reported in Chapter 6, a single set of parameters can fit this model to steady state polarization curves very well, the proposed mechanism (reactions 6.1, 6.2, 5.3-5.5) is likely adequate to describe the electrode response of this system. If this is correct, the most probable explanation for the observed variation of the kinetic parameters is that this system does not obey classical Butler-Volmer kinetics. The concentration and potential (in the case of EIS) dependence of the kinetic parameters likely reflects the dynamic changes of the interfacial structure in response to the time-varying input signals during EIS and LSV experiments [67-69]. The variation of transfer coefficients and rate constants with potential and electrolyte composition has been the subject of many theoretical and experimental studies, although the focus has primarily been on outer-sphere redox couples rather than on reactions such as metal deposition that involve adsorbed intermediates [67-69].

The plots in Figures 7.6 – 7.9 also present the variation of the partial current densities for Ni(II), H^+ and water reduction during the scans, as computed by the fitted model. The

contribution of the capacitive current is negligible in all cases and so cannot be observed in Figures 7.6 – 7.9. The order in which the model predicts the three reactions to become significant (reduction of H^+, then Ni(II) and finally water) agrees with what was concluded earlier based on the LSV curves (Figures 7.1 – 7.5). The contribution of H^+ reduction to the current is always small due to the relatively low bulk H^+ concentration. It is also interesting to note that i_H is observed to decline from its limiting value near the end of each of the scans in Figures 7.6 – 7.9. As the contribution from H^+ reduction diminishes, i_W becomes increasingly more important. The model also indicates that current due to water reduction exceeds that due to H^+ reduction when the electrode is strongly polarized to more negative potentials than –0.96 V. These findings are consistent with those of a previous modeling study carried out to analyze these two reactions in the absence of metal deposition [49]. The modeling presented in this chapter shows that the extent of water reduction is not influenced by the metal concentration when the $NiSO_4$ concentration is 50 mol m^{-3} or more. However, with reduction of the $NiSO_4$ concentration to 10 mol m^{-3}, the situation changes and i_W is enhanced throughout the scan (Figure 7.9).

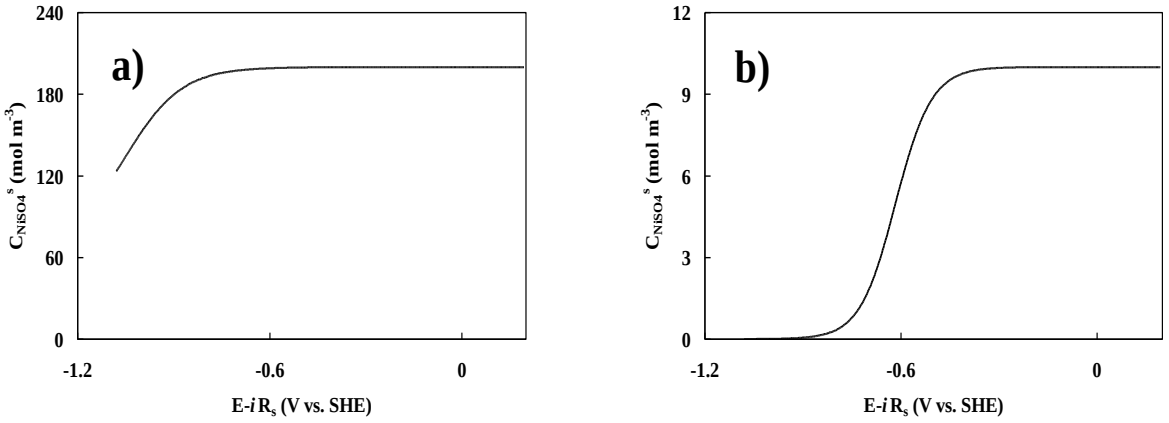

Figure 7.10. Variation of surface Ni(II) concentration during LSV scans operated at 0.1 mV s^{-1} as computed by the fitted model for a nickel disk electrode rotating at 1000 rpm in a solution at pH 3 containing 1500 mol m^{-3} Na_2SO_4, 500 mol m^{-3} $B(OH)_3$ and a) 200 or b) 10 mol m^{-3} $NiSO_4$. Curves are generated using parameters listed in Tables 5.2 and 7.1.

Further insight can be gained by computing the variation of non-measurable quantities such as the surface pH, fractional surface coverage of the adsorbed intermediates and surface concentrations over the course of the scans. Figures 7.10a and 7.10b depict the

variation of the surface concentration $C^{s}_{Ni(II)}$ of Ni(II) in solutions containing 200 and 10 mol m^{-3} $NiSO_4$, respectively, while Figures 7.11a and 7.11b present the concentration profiles for Ni(II) in the boundary layer at different potentials during the scans for the same solutions. These sets of results correspond to the LSV curves presented in Figures 7.6 and 7.9. The surface concentration has dropped to approximately 60 % of the bulk value by the end of the scan at the highest $NiSO_4$ concentration (Figures 7.10a and 7.11a), indicative of a system under mixed kinetic–mass transfer rate control. A similar situation arises for the cases of 100 and 50 mol m^{-3} $NiSO_4$ (not shown). On the other hand, the plots shown in Figures 7.10b and 7.11b clearly indicate that the system at 10 mol m^{-3} $NiSO_4$ has become mass transfer–limited during the course of the scan.

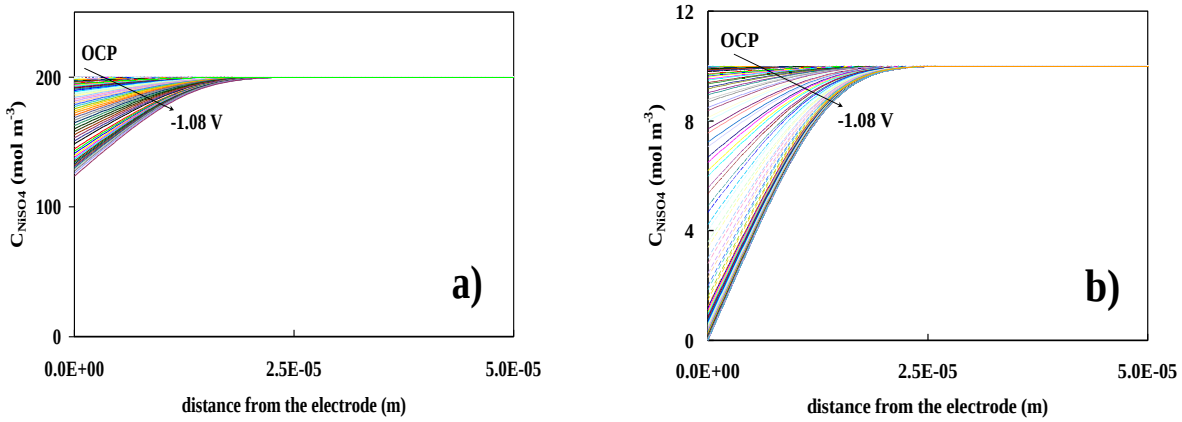

Figure 7.11. Ni(II) concentration profiles across the boundary layer at different potentials during LSV scans operated at 0.1 V s^{-1} as computed by the fitted model for a nickel disk electrode rotating at 1000 rpm in a solution at pH 3 containing 1500 mol m^{-3} Na_2SO_4, 500 mol m^{-3} $B(OH)_3$ and a) 200 or b) 10 mol m^{-3} $NiSO_4$. Curves are generated using parameters listed in Tables 5.2 and 7.1.

The variation of the fractional surface coverages of the intermediates $Ni(I)_{ads}$ and H_{ads} on the electrode surface during the scans are shown in Figures 7.12a and 7.12 b, respectively, for 200 and 10 mol m^{-3} $NiSO_4$. At the lower $NiSO_4$ concentration, θ_{Ni} rises to a maximum of ~ 0.03 at a potential of about –0.72 V before decreasing gradually over the remainder of the scan. This trend can be explained by considering the effect of potential on the rate of reaction (6.1) that produces $Ni(I)_{ads}$ sites and the rate of reaction 6.2 that consumes them. The rate of reaction (6.1) depends on the potential, θ_{Ni}, θ_{H} and $C^{s}_{Ni(II)}$, but the rate of reaction (6.2)

depends only on the potential and θ_{Ni}. During the early part of the scan, $C^{s}_{Ni(II)}$ remains close to $C^{b}_{Ni(II)}$ (Figure 7.11b), whereas θ_{Ni} and θ_{H} are both very small and so have very little effect on the rate of reaction (6.1). Consequently, the rate of reaction (6.1) increases as the scan proceeds primarily due to the influence of the potential. The rate of reaction (6.2) also increases at the same time, but is initially very low since it is proportional to θ_{Ni}. Thus, reaction 6.1 occurs at a faster rate than reaction (6.2) during the early part of the scan and causes θ_{Ni} to rise. However, this situation begins to change as the scan proceeds and $C^{s}_{Ni(II)}$ continues to decrease and both θ_{Ni} and θ_{H} increase, which are trends that impede reaction (6.1) and promote reaction (6.2). At a point during the scan when $C^{s}_{Ni(II)}$ becomes very small and i_{Ni} approaches its limiting value, the rates of reactions (6.1) and (6.2) become equal to each other and θ_{Ni} reaches a maximum (Figure 7.12). Thereafter, reaction (6.2) occurs faster than reaction (6.1) and θ_{Ni} decreases. Although not shown here, when deposition is carried out at 50 or 100 mol m^{-3} $NiSO_4$, a similar maximum is observed during the scan, but shifted toward larger θ_{Ni} values and more negative potentials. The behavior observed in Figure 7.12a for the case of 200 mol m^{-3} $NiSO_4$ differs because the end of the scan at –1.2 V is reached before a maximum can appear.

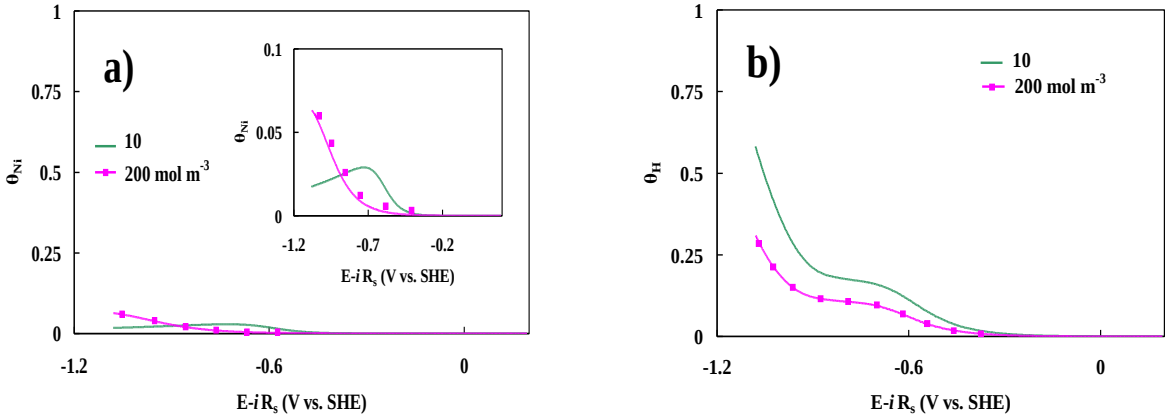

Figure 7.12. Variation of a) θ_{Ni} and b) θ_{H} during LSV scans operated at 0.1 V s^{-1} as computed by the fitted model for a nickel disk electrode rotating at 1000 rpm in solutions at pH 3 containing 1500 mol m^{-3} Na_2SO_4, 500 mol m^{-3} $B(OH)_3$ and 200 and 10 mol m^{-3} $NiSO_4$. Curves are generated using parameters listed in Tables 5.2 and 7.1.

Figure 7.12b shows that θ_H reaches larger levels particularly at higher overpotentials in a solution containing 10 mol m^{-3} $NiSO_4$ than one containing 200 mol m^{-3} $NiSO_4$ since H^+ and water reduction can compete more favorably with Ni(II) reduction. This effect is consistent with the observation above concerning Figure 7.9 that i_W is always higher for a scan obtained at 10 mol m^{-3} $NiSO_4$ than at 200 mol m^{-3} $NiSO_4$. It is also noteworthy that the surface coverage of H_{ads} is always higher than that of $Ni(I)_{ads}$. This supports the proposal that the rates of H^+ and water reduction are not controlled by a single reaction step but by a combination of reactions 5.3-5.5, as indicated in previous studies [41, 51]. A comparison of Figure 7.12a and 7.12b reveals that the rise of θ_H during the scans starts at more positive potentials than that of θ_{Ni} at all $NiSO_4$ concentrations. Another interesting feature of the plots in Figure 7.12b is the sharp transition from the plateau in θ_H to the steeply rising portion at high overpotentials which marks the point where water reduction begins to become dominant over H^+ reduction.

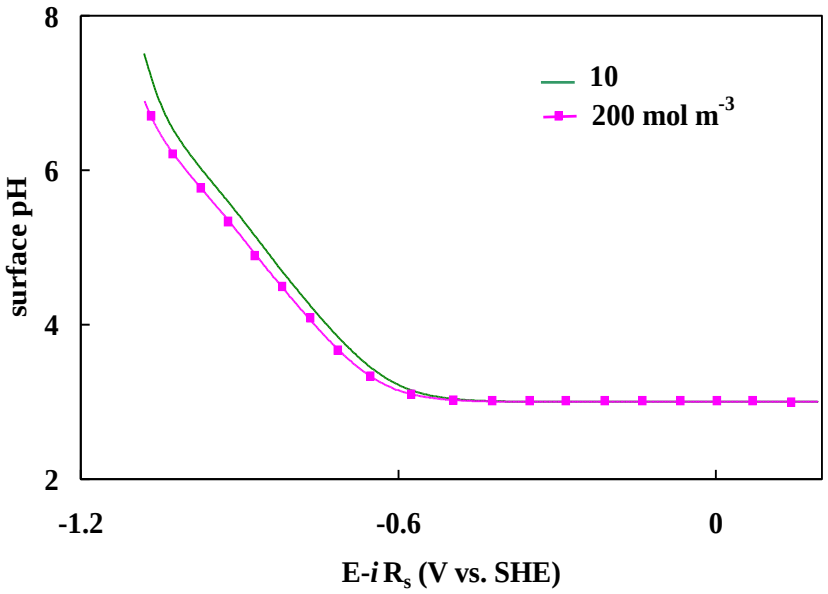

Figure 7.13. Variation of the surface pH during LSV scans operated at 0.1 mV s^{-1} as computed by the fitted model for a nickel disk electrode rotating at 1000 rpm in solutions at pH 3 containing 1500 mol m^{-3} Na_2SO_4, 500 mol m^{-3} $B(OH)_3$ and 200 and 10 mol m^{-3} $NiSO_4$. Curves are generated using parameters listed in Tables 5.2 and 7.1.

Figure 7.13 shows that the variation of the surface pH during the scans is affected only to a small extent by the $NiSO_4$ concentration. At any given potential, the surface pH is always slightly higher at the lower $NiSO_4$ concentration, which is understandable given that the role of HER is enhanced at lower $NiSO_4$ concentrations. Similar behavior is observed with respect to θ_H in Figure 7.12b. The rise of the pH in the vicinity of the electrode due to H^+ and water reduction is mitigated somewhat by the addition of $B(OH)_3$ which undergoes hydrolysis by borate dissociation (refer to Table 5.1) to release H^+ ions. The role of this reaction during the scans is revealed in Figures 7.14a and 7.14b which show that more $B(OH)_3$ is converted by hydrolysis to $B_3O_3(OH)_4^-$ as the potential becomes more negative or the $NiSO_4$ concentration is lowered. By the end of the scan, the surface concentration of $B(OH)_3$ has dropped by about 18% relative to its initial value when 200 mol m^{-3} $NiSO_4$ is present and 26 % when 10 mol m^{-3} is present, while the surface concentration of $B_3O_3(OH)_4^-$ has risen to 50 and 150 mol m^{-3}, respectively.

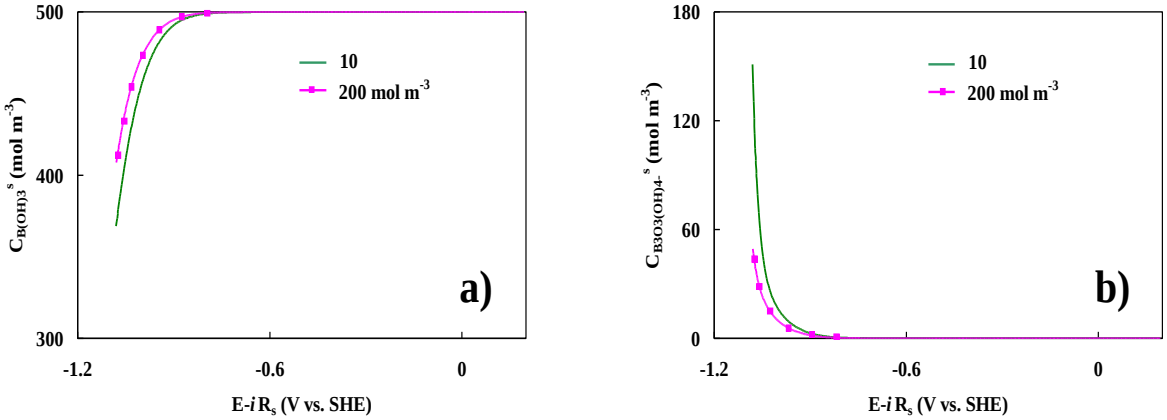

Figure 7.14. Variation of the surface concentrations of a) $B(OH)_3$ and b) $B_3O_3(OH)_4^-$ during LSV scans operated at 100 mV s^{-1} as computed by the fitted model for a nickel disk electrode rotating at 1000 rpm in solutions at pH 3 containing 1500 mol m^{-3} Na_2SO_4, 500 mol m^{-3} $B(OH)_3$ and 200 and 10 mol m^{-3} $NiSO_4$. Curves are generated using parameters listed in Tables 5.2 and 7.1.

7.3.1 Comparison of the kinetic parameters obtained by different techniques

As observed from a comparison of Tables 6.2 and 7.1, the kinetic parameters for nickel deposition as determined by EIS and LSV differ considerably from each other. This variation may be attributed to re-organization effects of the solvent and other molecules

adsorbed on the surface of the electrode [109-111]. As mentioned previously, these structural changes on the interface can cause the charge-transfer coefficients and rate-constants to vary with potential and concentration. Thus, since the electrode surface is perturbed differently during EIS and LSV experiments, it should not be surprising to find that the kinetic parameters obtained to differ depending on which of these techniques is being modeled. Furthermore, it has been reported in the literature that higher rate constants are obtained from EIS when the measurements are performed at near-zero current than when they are obtained from LSV where the current is varied over a much wider range of values [110-112]. This agrees with the trend observed in the present study that the rate constants obtained from EIS (Table 6.2) are higher than those obtained from LSV (Table 7.1).

In addition, the kinetic parameters obtained for single nickel (Table 6.2) and cobalt deposition (Table 5.3) using EIS are closer to each other than those obtained for single nickel deposition with LSV and EIS. Thus, it appears that the application of a small excitation signal to the system may be more reliable than measurements involving large potential sweeps [113] since the re-organization of the solvent molecules at the interface due to a small-amplitude periodic potential is smaller in scale than when a much larger-amplitude potential ramp is applied during LSV.

The modification in the kinetic parameters of the nickel deposition between the steady-state and transient techniques conducts to a variation in the behavior of some of the variables of the model. Figure 6.8 predicts that under steady-state conditions, the surface coverage for $Ni(I)_{ads}$ species will decay from a value close to 1 as the potential becomes more negative, whereas Figure 7.12 shows that this variable will increase up to a maximum before decaying as the potential is made more negative. The first situation stems from the fact that under steady state conditions the consumption of $Ni(I)_{ads}$ species at low overpotential is slower than its formation so that a considerable area of the electrode is becomes covered ($\theta_{Ni} \approx 1$). However, the surface coverage will always decay as the system approaches mass transport-limiting conditions because it is determined by the surface concentration which continually shrinks as the potential becomes more negative. In modeling LSV, an initial value of θ_{Ni} must be specified. Since the condition of a bare surface ($\theta_{Ni} = 0$) at the start of a LSV scan was adopted during the modeling of this technique, an increase is observed once that the reduction starts as a consequence of the formation of $Ni(I)_{ads}$ species on the surface of the electrode. This leads to the appearance of a maximum in its value at intermediate

overpotentials and a subsequent decline at higher overpotentials due to the promotion of the second step of nickel deposition. Thus, the initial state and history of the electrode can have a significant effect on the responses obtained during steady-state and transient techniques.

Chapter 8 Anomalous Behavior of Ni-Co Alloy Electrodeposition Under Different Conditions of pH, Current and Electrolyte Composition

8.1 Introduction

Interest in the formation of Ni-Co alloy coatings by electrochemical methods has been strong for many years due to their excellent magnetic properties, hardness, light weight, wear, versatility, abrasion and corrosion resistance [13, 17, 18, 26 27, 79-82]. The use of electroplating to produce these alloys is attractive due to its low cost, flexibility (e.g. deposition as single layer or multi-layer coatings on planar and non-planar substrates), efficiency (i.e. better properties of the alloys in comparison with conventional metallurgical procedures) and ease of high volume production in contrast with other methods such as sputtering and chemical vapor deposition [26, 79].

An important aspect of this system is that alloys of any composition can be formed since the two metals form solid solutions over the whole concentration range [83]. Indeed, this feature enables the variation of properties such as corrosion resistance over a wide range of compositions to be explored. However, alloys with a high Ni content are difficult to form electrochemically due to the anomalous nature of alloy formation under typical conditions [2]. As a result, Co is preferentially co-deposited even when Ni is present at higher concentrations in solution although Ni is considered to be the more noble component. Several experimental and theoretical studies have been conducted to analyse this anomalous behaviour [13-20, 81], although a significantly larger number of experimental papers on other aspects of this system are also found in the literature.

Among the iron-group metal alloys (e.g. Fe-Ni, Fe-Co, Ni-Co), the Fe-Ni system has probably been more widely studied [15, 42, 84-89] than the others. Due to the similarity in the behaviour of these alloys, the results obtained for the Fe-Ni system have also generally been considered to be applicable to Ni-Co co-deposition. One of the earliest studies on the co-deposition of iron-group metals was carried out by Dahms and Croll [90]. They suggested that the anomalous behaviour observed in the co-deposition of Fe-Ni alloys was due to the

Submitted to Electrochimica Acta, J. Vazquez-Arenas and M. Pritzker, "Anomalous Behavior of Ni-Co Alloy Electrodeposition Under Different Conditions of pH, Current and Electrolyte Composition".

formation of an intermediate ferrous hydroxide species ($Fe(OH)_{2ads}$) when the hydrogen limiting current density was exceeded. They proposed that this species inhibited nickel deposition by blocking the surface of the electrode without affecting Fe^{2+} reduction [90]. However, later, Andricacos et al [91] showed that anomalous behaviour can occur even at current densities well below the limiting current density for hydrogen evolution and at much lower surface pHs than would be expected based on the solution thermodynamics for the formation of $Fe(OH)_2$.

More recent mechanisms are based on the competition between adsorbed species (i.e. hydroxides) on the surface of the electrode as a result of the hydrolysis of the metallic cations and the rise in surface pH due to hydrogen evolution [84, 85]. The formation of these species at the electrode/solution interface can be expressed by the following reactions:

$$Me^{2+} + OH^- = Me(OH)^+ \quad (8.1)$$

$$Me(OH)^+ = Me(OH)^+_{ads} \quad (8.2)$$

$$Me(OH)^+_{ads} + 2e^- = Me + OH^- \quad (8.3)$$

$$2H_2O + 2e^- = H_2 + 2OH^- \quad \text{(cathodic side reaction)} \quad (8.4)$$

where Me^{2+} represents either Co^{2+}, Ni^{2+} or Fe^{2+}. The forward direction of reaction (8.3) favours the continuous formation of OH^-, which directly enhances the adsorption of $Me(OH)^+_{ads}$ by reaction (8.2). The anomalous behaviour is explained by considering that the less noble metal hydroxide $Co(OH)^+$ can adsorb more rapidly than $Ni(OH)^+$ and deposit at a faster rate via reaction (8.3) [84, 85].

Bai and Hu [84, 85] found using cyclic voltammetry that the anomalous behaviour of Ni-Co alloys is suppressed when the coatings are formed at lower pH (e.g. 2.0) and deposition is followed by anodic polarization to dissolve some of the deposited metals. They suggested that this is possible due to inhibition of $Me(OH)^+_{ads}$ and hydroxide formation which enables normal co-deposition of free metal ions to occur. However, recent modeling studies have revealed that the concentrations of $Ni(OH)^+$ and $Co(OH)^+$ during single metal deposition are extremely low, making deposition via these ions less likely [41, 51, 66]. On the other hand, the same authors reported that the system exhibited more anomalous behaviour when the solution pH was raised, an expected result due to the more favourable conditions for the formation of hydroxides and $Me(OH)^+$ [84, 85]. Based on this reasoning,

they propose that the order in which metals are deposited in these alloy systems should follow in the same order as the equilibrium constants for the formation of $Me(OH)^+$ by reaction (8.1), i.e.., Fe > Co > Ni [84]. However, the differences between the values of the equilibrium constants among the elements involved in anomalous co-deposition are not significant [92]. Consequently, it does not appear that differences in the thermodynamics of the generation of bulk $Me(OH)^+$ are the key factors to account for the anomalous behaviour of these alloys. Moreover, it is difficult to determine if the observed anomalous behaviour is consistent with thermodynamic predictions since no data are available for adsorbed surface species. As stated previously, anomalous co-deposition can occur at much lower surface pH values than those needed for the formation of the bulk metal hydroxides [87, 91].

Sasaki and Talbot [93] stressed the importance of $Me(OH)^+$ in the formation of iron-group alloys and their incorporation in the electrodeposition mechanism. In addition, another factor not considered by these authors [93] as well as by the authors in references [84, 94] is that soluble metal sulphates and chlorides are the predominant species in the chloride and sulphate baths used in these studies and not Fe^{2+}, Ni^{2+}, $Fe(OH)^+$ and $Ni(OH)^+$ [41, 51, 53, 66, 95, 96]. For these reasons, the importance of metal hydrolysis is unclear and may not be responsible for the anomalous behaviour.

On the other hand, Matlosz [43] proposed a predictive model for the co-deposition of Fe-Ni alloys based on a preferential surface coverage of the adsorbed iron-intermediate species, inhibiting the more noble nickel due to differences in kinetics of electrosorption. This model considers the formation of adsorbed monovalent intermediates via consecutive 1-electron transfer steps and hydrolysis of Fe^{2+} and Ni^{2+}. Calculations conducted in this study suggested that changes in surface pH are not required for iron-rich anomalous deposits and that the hydroxide concentration at the electrode surface does not change the reaction mechanism. Matlosz [43] showed that normal deposition in which nickel deposition is not inhibited occurs at low overpotentials, whereas more iron-rich deposits are produced at higher overpotentials. He also suggested that the kinetics of Ni^{2+}, Fe^{2+} and H^+ reduction are essentially uncoupled and may be treated separately. However, this suggestion is not likely true since at the very least the adsorbed intermediates associated with these reactions must compete for sites on the electrode surface. In addition, Matlosz made the simplifying assumption that the surface pH independent of potential and did not include water reduction in the reaction mechanism.

However, more recently Gomez et al [15] reported on the basis of galvanostatic experiments in a chloride bath at pH 3 on a vitreous carbon substrate that a higher overpotential is required to deposit nickel onto cobalt than is needed to deposit cobalt onto cobalt or nickel surfaces. They proposed that the anomalous behaviour occurs due to the sequence of the following two steps: i) nickel is first deposited from Ni(II) species and then ii) Co(II) adsorbs onto the deposited nickel sites and is subsequently reduced to its metallic form. Inhibition of nickel deposition takes place as a result of Co(II) adsorption. At the same time, cobalt deposition is catalyzed on the existing nickel sites.

A model that better captures all these phenomena occurring during co-deposition of iron-group metals was provided by Zech et al. [42, 88, 89]. They compared the experimentally determined partial current densities of the metals co-depositing during alloy formation with those obtained during single metal deposition. They suggested that not only do inhibiting effects (i.e. Ni is inhibited by Fe^{2+} and Co^{2+} ions) occur, but also acceleration of the deposition of the less noble metal occurs, i.e. iron deposition rate is enhanced by Co^{2+} and Ni^{2+} ions [42, 89]. The inhibiting effect is generally stronger when the reaction rate of the less noble metal is kinetically controlled and diminishes as the limiting current is reached. With these findings in mind, they derived a model accounting for both the acceleration of the co-deposition of the less noble component and the inhibition of the more noble one [89]. The model accounts for three parallel pathways for metal deposition involving 1-electron transfer steps. These pathways lead to the following adsorbed intermediates on the electrode surface: $Co(I)_{ads}$, $Ni(I)_{ads}$ and a mixed intermediate species containing both metal ions (i.e. $NiCo(III)_{ads}$) in a partly reduced state. The first two intermediates are the same species that form during single metal deposition. In this model, the mixed intermediate plays the key role in explaining the anomalous behaviour by providing an additional pathway for the deposition of metallic cobalt. The model also included side reactions due to H^+ and water reduction and mass transport effects due to diffusion. To our knowledge, this is the most comprehensive model describing the anomalous behaviour.

However, as stressed by these authors [89], some gaps with regard to prediction of the alloy composition still exist that cannot be properly addressed by their model. This problem may arise from uncertainties surrounding the role played by the HER. From previous studies on single metal deposition (i.e. Co, Ni, Fe), it is known that the formation of HER likely involves an adsorbed species (i.e. H_{ads}) which is not considered in the model of Zech et al. [89]. Given the importance of the competition between the different adsorbed species, the

inclusion of H_{ads} may be important and so its effects should be considered. Consequently, the possibility exists that some other phenomenon not considered by Zech et al. (e.g., differences in preference for the electrode surface among the various intermediates [43] or differences in charge-transfer rates) may be a more important factor for anomalous co-deposition than an additional pathway involving the $NiCo(III)_{ads}$ mixed intermediate. In addition to this, the buffering effects generated by the addition of boric acid (i.e. typically added to iron-group metal baths) have not been studied and modelled during the co-deposition of these alloys. In single metal deposition [41, 51, 66, 95, 96], these effects have been found to be very important since the models overestimate the surface pH when this effect is not included. Presumably, this situation also arises in alloy systems and so should be considered in the analysis. In terms of mass transport, convective effects should be also included in the model since experiments are usually conducted under stirred conditions on rotating disk electrodes, something which has not usually been considered in previous models [94].

Therefore, we have conducted a series of experiments in order to gain a better understanding of the anomalous behaviour during the codeposition of Ni-Co alloys. In this chapter, we describe the results of electrodeposition experiments of Ni-Co alloys under dc conditions to elucidate the role of the buffer, the Co/Ni concentration ratio in the bulk solution, pH, current efficiency, etc. In the next chapter, information gained from the current study and previous ones reported in the literature will be used to formulate a more comprehensive model than has previously been presented for this system to include more detailed kinetics, homogeneous reactions (i.e., water dissociation, boric acid hydrolysis) and mass transport by diffusion and convection.

8.2 Results

8.2.1 Linear sweep voltammetry

Figure 8.1 shows linear sweep voltammograms obtained at a scan rate of 0.1 V s^{-1} and a rotation speed of 1000 rpm in a solution containing 1500 mol m^{-3} Na_2SO_4, 500 mol m^{-3} $B(OH)_3$ and different concentrations of $CoSO_4$ and $NiSO_4$ listed in Table 8.1. The experiment performed in the presence of the supporting electrolyte only (i.e. labelled SE) is also included for comparison. In each case, the scan proceeded from the open circuit potential (OCP) to more negative potentials. As observed in all the cases shown in this figure

including when the solution contains SE alone, measurable current density is observed when the potential reaches approximately –0.5 V during the scans. Since H^+ reduction is considered to be more noble than the other processes (i.e. more positive Nernst potential) and is the only expected reaction at low overpotentials in the presence of SE alone, the current in this low overpotential region is assigned to H^+ reduction and labeled as region I.

Table 8.1. $CoSO_4$, $NiSO_4$ and $B(OH)_3$ concentrations and pH of the baths to co-deposit Ni-Co alloys using a 1500 mol m^{-3} Na_2SO_4 supporting electrolyte.

Bath No.	$[CoSO_4]$ (mol m^{-3})	$[NiSO_4]$ (mol m^{-3})	$[B(OH)_3]$ (mol m^{-3})	pH
SE	0	0	500	3.0
1	18	100	500	3.0
2	18	200	500	2.0
3	18	200	500	3.0
4	18	200	500	4.0
5	18	200	0	3.0
6	18	200	250	3.0
7	18	300	500	3.0
8	18	400	500	3.0
9	170	1300	500	3.0
10	0	10	500	3.0
11	0	50	500	3.0
12	0	100	500	3.0
13	0	200	500	3.0
14	0	300	500	3.0
15	0	400	500	3.0
16	10	0	500	3.0
17	50	0	500	3.0
18	100	0	500	3.0
19	200	0	500	3.0

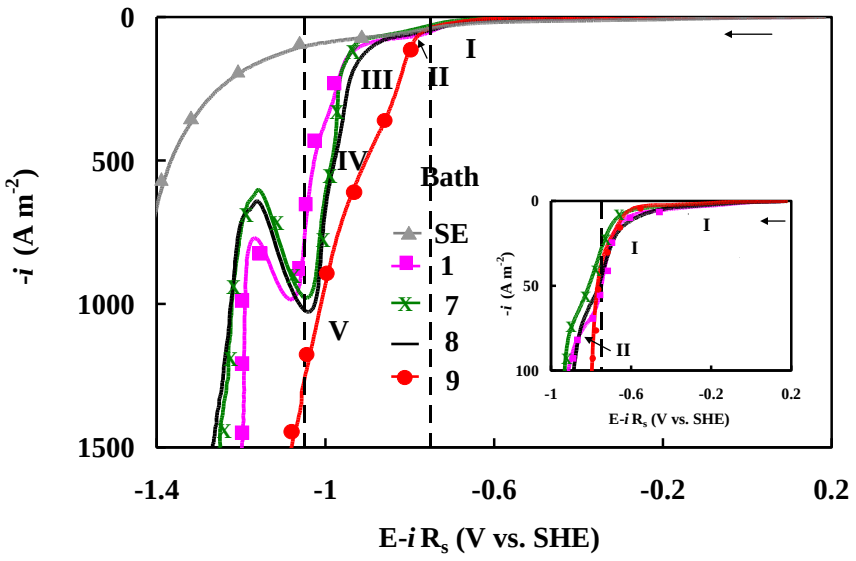

Figure 8.1. Linear voltammograms measured at 100 mV s^{-1} on copper disk electrodes rotating at 1000 rpm in solutions containing 1500 mol m^{-3} Na_2SO_4, 500 mol m^{-3} $B(OH)_3$ (SE) and different concentrations of $NiSO_4$ and $CoSO_4$ (bath) reported in Table 8.1 at pH 3.

When the potential reaches ~ –0.6 V, an additional current rise is observed (labelled region II) for bath 9 only, which contains the highest $NiSO_4$ concentration (1300 mol m^{-3}) among the experiments considered in Figure 8.1. This process is not likely a continuation of H^+ reduction or a double layer charging effect since it is not observed in the voltammogram recorded in SE alone. Therefore, it is likely that region II arises mostly due to the onset of Ni(II) reduction. This assignment is confirmed by the electrode responses shown in Figure 8.2 for LSVs obtained in solutions containing a range of $NiSO_4$ concentrations, but without any $CoSO_4$ (i.e., baths 11, 12 and 13). As shown, all the curves exhibit a strong overlap in region II [96].

Surprisingly, very little evidence for region II appears in the scans in Figure 8.1 when the solutions contain only 100, 300 or 400 mol m^{-3} $NiSO_4$. This might be due to inhibition of Ni(II) reduction due to the presence of Co(II), as has been previously proposed by other authors [15, 88, 89].

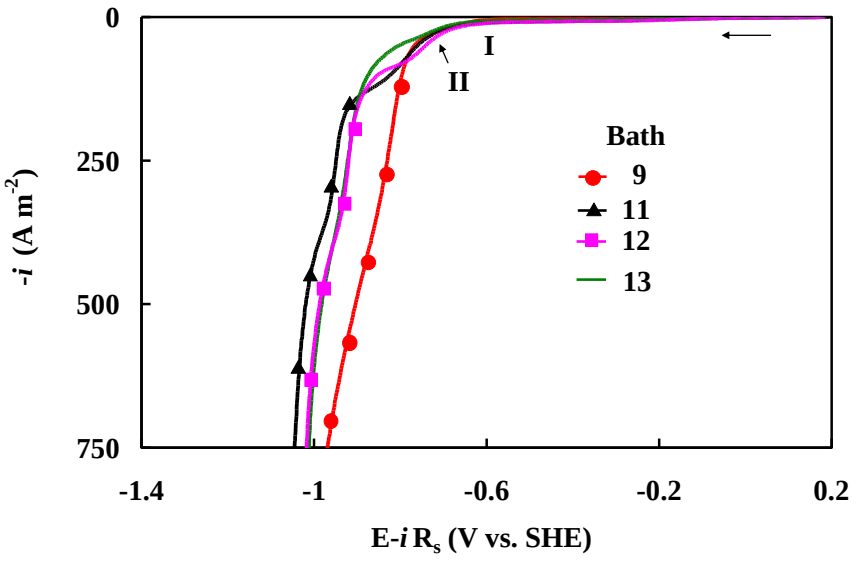

Figure 8.2. Linear voltammograms measured at 100 mV s^{-1} on copper disk electrodes rotating at 1000 rpm in solutions containing 1500 mol m^{-3} Na_2SO_4, 500 mol m^{-3} $B(OH)_3$ and different concentrations of $NiSO_4$ and $CoSO_4$ (bath) reported in Table 8.1 at pH 3.

To explore this phenomenon further, single metal deposition of nickel and cobalt was conducted onto substrates of the same and different metal type, i.e. Co deposition onto Co and Ni and Ni deposition onto Ni and Co. Figure 8.3 shows the LSV scans obtained on Co or Ni substrates obtained in solutions containing 10 and 50 mol m^{-3} $CoSO_4$ and $NiSO_4$, respectively (refer to Table 8.1). Figure 8.4 shows the results of similar experiments carried out in 100 and 200 mol m^{-3} $CoSO_4$ and $NiSO_4$ solutions deposited onto nickel or cobalt. Comparison of the curves at lower metal concentrations (Figure 8.3) indicates that below about –0.85 V the current for Ni(II) reduction (baths 10 and 11) exceeds that for Co(II) reduction (baths 16 and 17). However, at some point later during the scans, the rate of Co(II) reduction becomes more substantial and a cross-over is observed whereby the current density for cobalt deposition overtakes that of nickel deposition. At higher metal concentrations (Figure 8.4), the onset of the two reactions during the scans is now observed at similar potentials. The current for Ni deposition is similar to that for Co at low overpotentials, but falls behind once higher overpotentials are reached (i.e., baths 12 and 13). A comparison of the voltammograms shown in Figure 8.4 for single metal deposition reveals that the deposition on cobalt onto cobalt occurs faster than that of nickel onto nickel at the same metal concentrations, particularly at high overpotential (compare bath 18 with 12 and bath 19

with 13). These findings indicate that the preferential depositon of Co over that of Ni is not unique to the alloy system and also occurs in the single metal systems. As a result, the anomalous behavior observed in the alloy system may not necessarily arise from interactions between the two metals, as has been proposed [15, 42, 88, 89]. This opens up the possibility of other causes of the anomalous behavior such as the inherently faster kinetics of Co(II) reduction in comparison to that of Ni(II) or the preferential surface coverage by $Co(I)_{ads}$ relative to that by $Ni(I)_{ads}$ on the electrode [43].

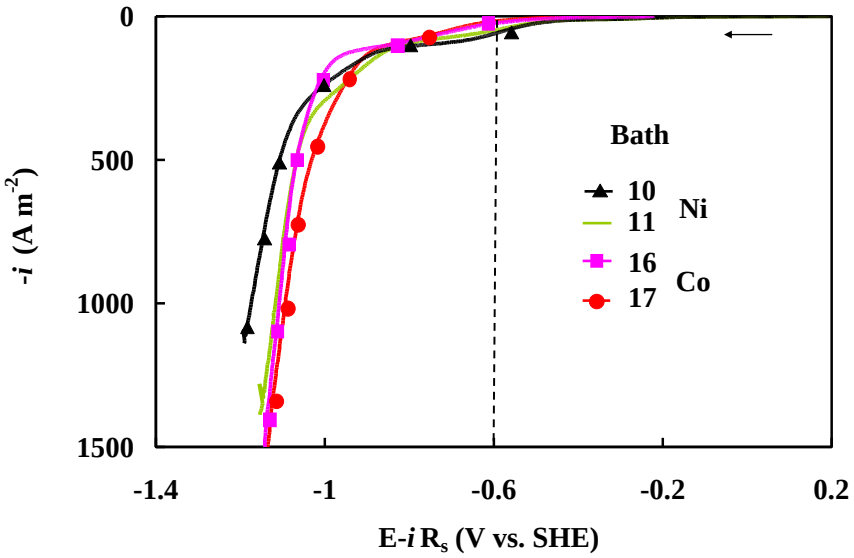

Figure 8.3. Linear voltammograms measured at 100 mV s^{-1} on nickel (baths 10 and 11) and cobalt (baths 16 and 17) disk electrodes rotating at 1000 rpm in solutions containing 1500 mol m^{-3} Na_2SO_4, 500 mol m^{-3} $B(OH)_3$ and different concentrations of $NiSO_4$ and $CoSO_4$ reported in Table 8.1 at pH 3.

Another interesting comparison regarding the curves in Figure 8.4 involves the response for Co deposition from a 200 mol m^{-3} $CoSO_4$ solution (i.e., bath 19) depending on the nature of the substrate. Higher current is observed throughout the scan when cobalt is deposited onto a cobalt substrate than when it is deposited onto a nickel substrate. This observation suggests that cobalt deposition is slightly inhibited by the presence of metallic nickel on the electrode. On the other hand, the scans in Figure 8.4 show that nickel deposition from a 200 mol m^{-3} $NiSO_4$ is not strongly affected by the nature of the substrate. Overall, these results clearly indicate that the nature of the substrate does not play a critical role in anomalous co-deposition.

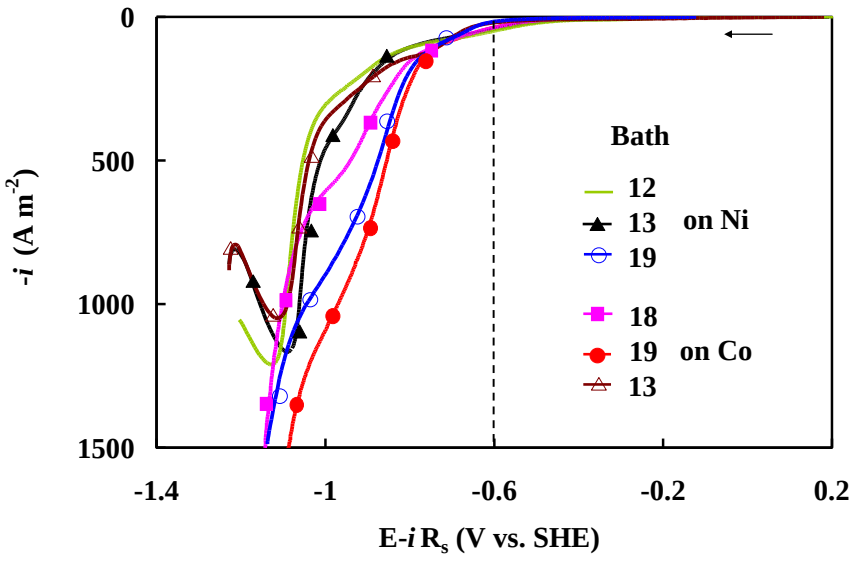

Figure 8.4. Linear voltammograms measured at 100 mV s^{-1} on nickel (baths 12 and 13) and cobalt (baths 18 and 19) disk electrodes rotating at 1000 rpm in solutions containing 1500 mol m^{-3} Na_2SO_4, 500 mol m^{-3} $B(OH)_3$ and different concentrations of $NiSO_4$ and $CoSO_4$ reported in Table 8.1 at pH 3.

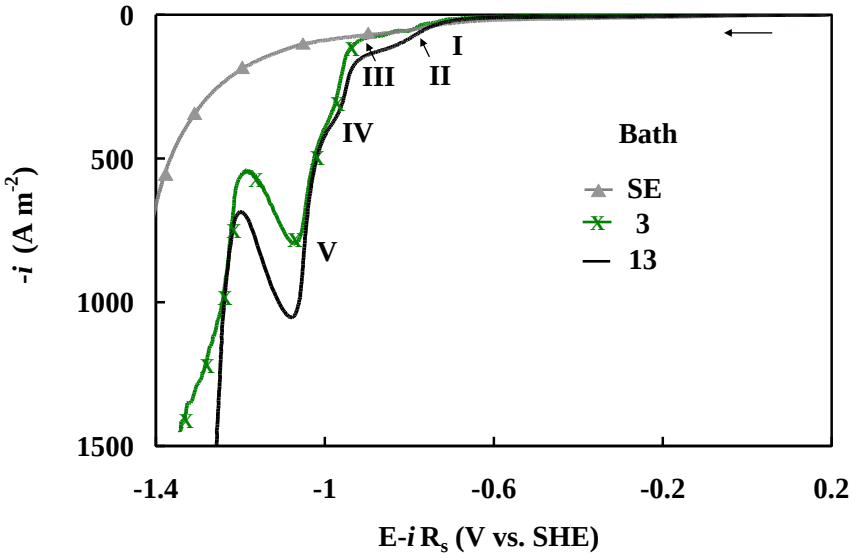

Figure 8.5. Linear voltammograms measured at 100 mV s^{-1} on copper disk electrodes rotating at 1000 rpm in solutions containing 1500 mol m^{-3} Na_2SO_4, 500 mol m^{-3} $B(OH)_3$ (SE), 200 mol m^{-3} $NiSO_4$ (bath 13), and 200 mol m^{-3} $NiSO_4$ + 18 mol m^{-3} $CoSO_4$ (bath 3) at pH 3.

In order to further explore the origin of anomalous co-deposition, we compared the scans obtained on copper disks at different $NiSO_4$ concentrations both in the presence and absence of $CoSO_4$ in solution. The results of these experiments are shown in Figures 8.5 – 8.7 for 200, 300 and 400 mol m^{-3} $NiSO_4$, respectively. In each case, the $CoSO_4$ concentration is set to either 18 or 0 mol m^{-3}. The current density in the vicinity of –0.85 V is always higher in the absence of $CoSO_4$, providing additional support that nickel deposition is inhibited by the presence of Co(II) in solution. The fact that the Co(II) level is less than 10% that of Ni(II) in each case reveals the strength of its inhibitory effect. Comparison of Figures 8.5 – 8.7 reveals that this effect is larger at $NiSO_4$ concentrations of 200 and 300 mol m^{-3} than at 400 mol m^{-3}. Presumably, enough Ni(II) is present at the electrode/solution interface at the highest concentration to counteract the effect of the much lower Co(II) level. This effect of the Co(II) concentration on Ni(II) deposition could be due to any one of the three factors mentioned above (i.e., differences in surface coverage by adsorbed intermediates, catalysis of Co(II) reduction, differences in charge transfer rates).

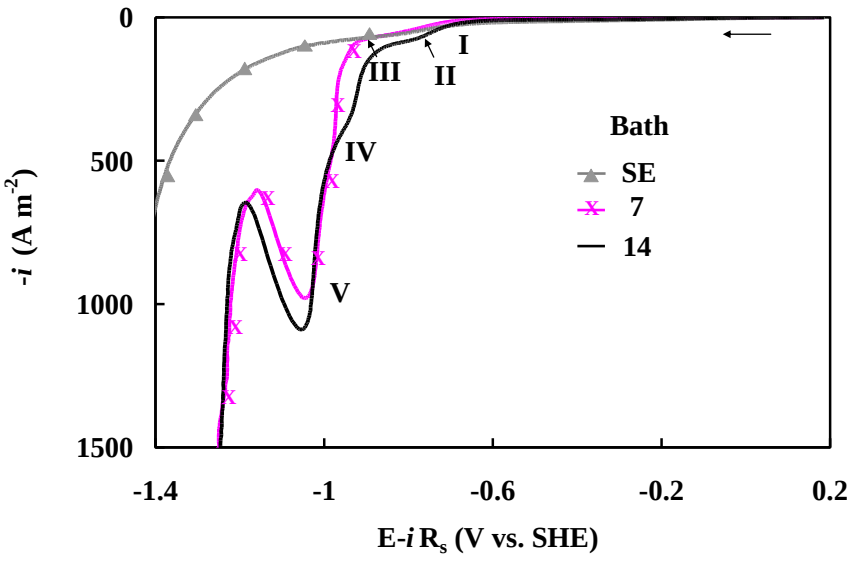

Figure 8.6. Linear voltammograms measured at 100 mV s^{-1} on copper disk electrodes rotating at 1000 rpm in solutions containing 1500 mol m^{-3} Na_2SO_4, 500 mol m^{-3} $B(OH)_3$ (SE), 300 mol m^{-3} $NiSO_4$ (bath 14), and 300 mol m^{-3} $NiSO_4$ + 18 mol m^{-3} $CoSO_4$ (bath 7) at pH 3.

It is difficult at this point to evaluate each of these possibilities from experiments. The best approach is probably to make use of a physicochemical model that discriminates the impact of these three effects on the electrode response and the anomalous behavior. This is one of the main questions to be addressed by the model that will be presented in Chapter 9. At this point, we assign the region denoted as III in the curves obtained in solutions containing both dissolved Ni(II) and Co(II) to the acceleration of cobalt co-deposition and/or the inhibition of nickel deposition.

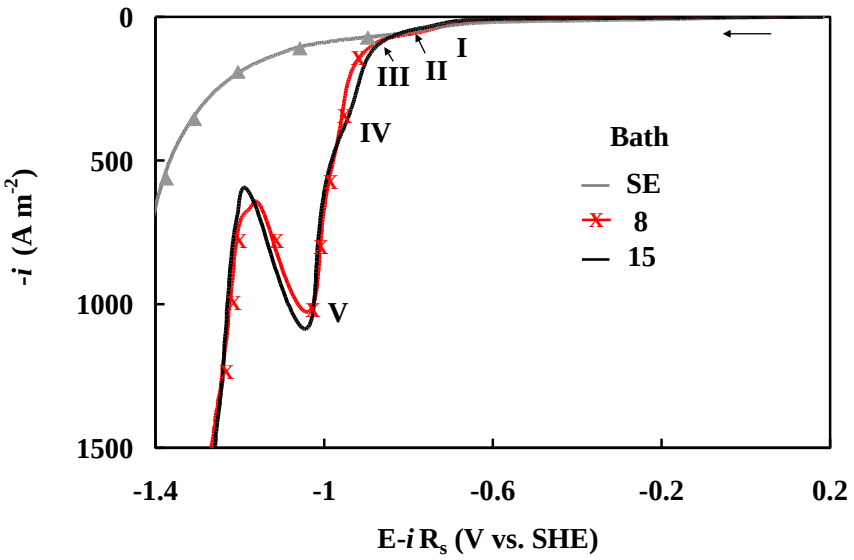

Figure 8.7. Linear voltammograms measured at 100 mV s^{-1} on copper disk electrodes rotating at 1000 rpm in solutions containing 1500 mol m^{-3} Na_2SO_4, 500 mol m^{-3} $B(OH)_3$ (SE), 400 mol m^{-3} $NiSO_4$ (bath 15), and 400 mol m^{-3} $NiSO_4$ + 18 mol m^{-3} $CoSO_4$ (bath 8) at pH 3.

As the scan proceeds further to ~ –1 V, the current density rises even more steeply well above the limiting current values for H^+, Co(II) and Ni(II) reduction. This transition is marked by another inflection point that reflects the onset of water reduction that we denote as region IV [96]. The potential for its onset varies depending on the $NiSO_4$ and $CoSO_4$ concentrations. As the potential becomes even more negative, the current continues to rise until the appearance of a peak whereupon the cathodic current drops. This peak is denoted as V in the scans. Since the electrode is being rotated, a constant flux of species from the bulk solution to the surface of the electrode can be maintained. Thus, the appearance of peak V is not likely related to the mass transport of any of the electroactive species becoming limiting.

Therefore, we suggest that this process is due to the formation of a passivating film (e.g. hydroxides, oxides) on the surface of the electrode, which partially blocks the cathodic reactions. However, once the potential becomes more negative than approximately –1.16 V, it appears that this layer completely or partially breaks down and the surface becomes re-activated. The steepness of the current rise in this last portion of the scan is comparable to that observed just before the appearance of peak V. It is significant that the features on the scan between –1.0 and –1.2 V that include peak V followed by the drop in current and then the re-activation are bypassed entirely at the highest $NiSO_4$ concentration of 1300 mol m^{-3} (see bath 9 in Figure 8.1). The limiting current density for Ni(II) reduction based on the Levich equation at this concentration is estimated to be ~12078 A m^{-2} which is much higher than the current densities of 700 – 1000 A m^{-2} corresponding to peak V. Thus, depletion of Ni(II) at the electrode surface should not be complete when this portion of the scan is reached. As shown in a previous study [96], water reduction tends to occur to a significant extent only once the other reduction reactions have reached mass transfer-limiting conditions. Consequently, it is reasonable to expect that not much water reduction has occurred when an electrode potential of –1.0 V is reached during the scan in bath 9. This suggests that the formation of the passivating film occurs rapidly once water reduction begins and OH^- ions are released at the electrode surface. It is also important to note that when single metal deposition is conducted peak V appears in the scans obtained in intermediate-to- high $NiSO_4$ solutions, but not in $CoSO_4$ solutions (Figure 8.4). This observation suggests that the passivating film is some sort of nickel oxide or hydroxide and does not contain cobalt, but can still form in the Ni-Co alloy system when Co(II) is also present in solution.

The influence of bulk pH values of 2, 3 and 4 on the electrode response is shown in Figure 8.8 for a bath containing 200 mol m^{-3} $NiSO_4$ and 18 mol m^{-3} $CoSO_4$. Not surprisingly, the current density associated with H^+ reduction (i.e. process I) is larger at pH 2 than at the higher values. Also included on this plot are the limiting current densities estimated using the Levich equation and $D_{H+} = 9.312 \times 10^{-9}$ m^2 s^{-1} for pH values of 2 and 3. Examination of Figure 8.8 not surprisingly indicates that H^+ reduction overlaps metal deposition more strongly during the scans at pH 2 than at pH 3. On the basis of the calculated limiting current density at pH 2, H^+ reduction becomes mass transport-controlled at potentials where the current for Ni(II) and Co(II) reduction becomes significant. On the other hand, the shape of the curves in the regions II, III and V attributed to Ni(II), Co(II) and water reduction also are influenced by the pH. This finding is consistent with what has been previously reported for

single nickel and cobalt deposition [95, 96], presumably since H^+ and water reduction affect the adsorption of the other species present at the electrode/solution interface and the change of the surface pH affects the formation of oxides or hydroxides of the metals being deposited. Therefore, it is not completely correct to assume that H^+ and water reduction do not affect the co-deposition of the Ni-Co alloy, as has often been done in previous studies [42, 66, 88, 89, 95, 96]. As shown in Figure 8.8, the pH affects the electrode response in the vicinity of peak V. Peak V shifts toward more negative potentials and becomes smaller as the pH is lowered, suggesting that this change slows down water reduction

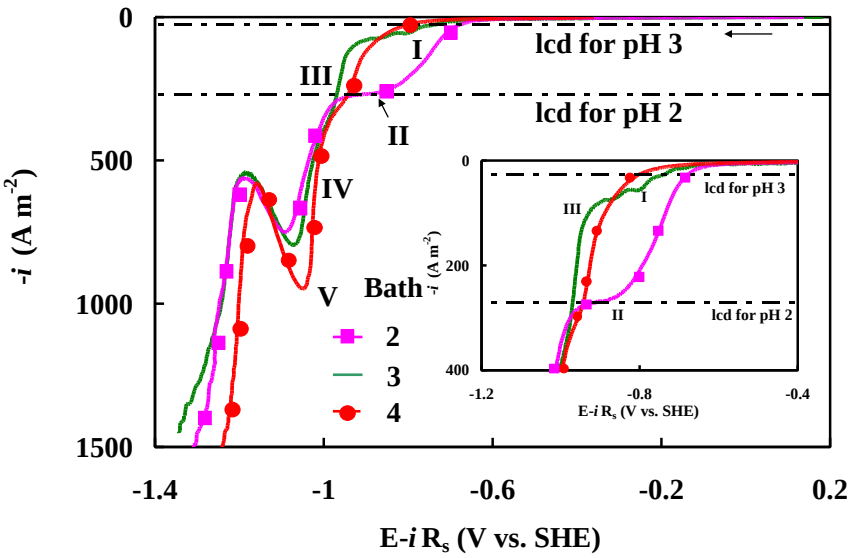

Figure 8.8. Linear voltammograms measured at 100 mV s^{-1} on copper disk electrodes rotating at 1000 rpm in solutions containing 1500 mol m^{-3} Na_2SO_4, 500 mol m^{-3} $B(OH)_3$, and 200 mol m^{-3} $NiSO_4$ + 18 mol m^{-3} $CoSO_4$ at different pH values: 2 (bath 2), 3 (bath 3) and 4 (bath 4).

The influence of boric acid ($B(OH)_3$) at concentrations of 0 (bath 5) and 250 mol m^{-3} (bath 6), with the concentrations of the other components maintained constant at 200 mol m^{-3} $NiSO_4$, 18 mol m^{-3} $CoSO_4$ and pH 3 is presented in Figure 8.9. As observed from this figure, the reduction processes I – IV described above are observed in both experiments. However, the appearance of peak V followed by the drop in current and then re-activation is exhibited only in the voltammogram obtained in the presence of $B(OH)_3$ and not at all when the buffering agent is absent. In the absence of boric acid, the current increases sharply at a potential of about –1.0 V similar to that observed in the presence of boric acid, but only until

a current density of about 270 A m^{-2} is reached, whereupon an abrupt flattening of the current rise occurs. The rise in current with potential gradually steepens until it once again coincides with that obtained in the presence of boric acid at a potential of about –1.2V. The differences in the electrode responses over the potential range from –1.0 to –1.2 V suggest that the film forms earlier during the scan in the absence of boric acid than in its presence and more strongly suppresses the current over the next 0.2 V of the scan. On the other hand, in the presence of boric acid, the current is able to continue rising steeply well beyond the level reached in absence of the buffer. However, soon thereafter, a film begins to form and suppress the electrode response, leading to the appearance of peak V. Over the next 0.1 V or so of the scan, this film continues to grow and cause the current to drop until it reaches the same level obtained in the absence of boric acid. Almost immediately thereafter, the film breaks down and the electrode becomes re-activated. It should be noted that the film formed during these scans is never completely passivating and always is able to permit the passage of a significant amount of current.

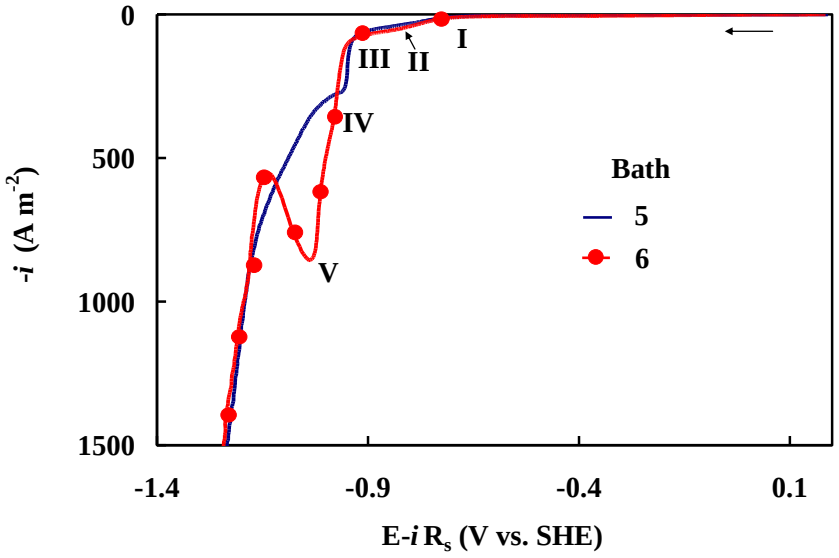

Figure 8.9. Linear voltammograms measured at 100 mV s^{-1} on copper disk electrodes rotating at 1000 rpm in solutions containing 1500 mol m^{-3} Na_2SO_4, 200 mol m^{-3} $NiSO_4$ + 18 mol m^{-3} $CoSO_4$, and 0 (bath 5) and 250 (bath 6) mol m^{-3} $B(OH)_3$ at pH 3.

The role of boric acid is to mitigate the rise of the surface pH due to H^+ and water reduction through the following hydrolysis reaction [65, 95, 96]:

$$3B(OH)_3 \rightleftharpoons B_3O_3(OH)_4^- + H^+ + 2H_2O \qquad (8.1)$$

Therefore, the resulting current density in the presence of this buffering agent is bigger because of the continuous generation of H^+ in the interfacial region which can subsequently be reduced. The importance of reaction (8.1) also stems from the fact that the precipitation of oxide and hydroxide species will more readily occur if $B(OH)_3$ is not present in solution (i.e. bath 5). These compounds can be poorly conducting and block the reduction of incoming species and lower the current density than that observed in the absence of these blocking layers (i.e. bath 6). If the potential is made more negative than the region of process V, both voltammograms in Figure 8.9 show similar behavior and a very steep increase in current. This finding suggests that the surface oxides eventually break down at high enough overpotentials to leave the electrode surfaces in similar states regardless whether or not boric acid is present.

8.2.2 Steady state cathodic polarization curves

Figure 8.10 shows steady state cathodic polarization curves in solutions containing 1500 mol m^{-3} Na_2SO_4, 500 mol m^{-3} $B(OH)_3$ at pH 3 and different $NiSO_4$ and $CoSO_4$ concentrations (see Table 8.1 for bath compositions). These curves were obtained by sampling the steady-state potential attained during galvanostatic experiments in which different current density values were applied to the cell. Thus, each data point on the plots represents a measurement obtained from a separate experiment. In each case, enough time was allowed to ensure that a total charge of 1.5 C had been passed when the potential was measured. As observed on these plots, the higher the $NiSO_4$ concentration, the higher the current density is at the same potential. This finding is consistent with the fact that the reaction rate increases with the bulk concentration of the electroactive species, therefore increasing its reduction rate when this value is higher (i.e. bath 9).

For the purposes of analysis of these polarization curves, we break them down into three zones: low overpotentials, low-intermediate overpotentials and high overpotentials. The breakdown of the reduction of Ni(II) and Co(II) into these three regions is indicated with dashed lines in Figure 8.10. These regions can only be roughly estimated since the values of the surface concentrations are unknown. The first region has been taken to cover the low overpotential portion until the current begins to rise steeply. The second region spans the part of the curve where the current rises most steeply. The start of the third region has been

chosen to coincide with the potential where the current begins to level off. The approximate potentials where processes I-V described previously occur are also shown on the plot. In the low overpotential region, H^+ reduction starts and the first nuclei of nickel and cobalt are co-deposited. The low-intermediate overpotential region is characterized by the massive occurrence of reactions II and III as a consequence of their activation and the onset of water reduction (IV). This region particularly in the vicinity of – 1 V is also marked by a steep increase in current density as the potential is changed. A similar trend is observed in the LSVs in Figure 8.1.

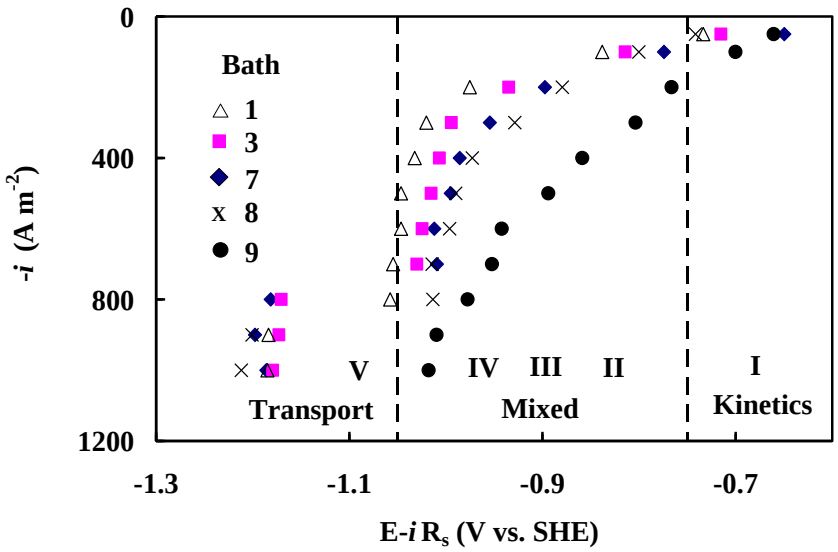

Figure 8.10. Experimental steady-state polarization curves obtained on copper disk electrodes rotating at 1000 rpm in solutions containing 1500 mol m^{-3} Na_2SO_4, 500 mol m^{-3} $B(OH)_3$ and different concentrations of $NiSO_4$ and $CoSO_4$ (bath) reported in Table 8.1 at pH 3.

When high current densities ($\geq$ 800 A m^{-2}) are applied and the system enters the region where the reduction of Ni(II), Co(II) and H^+ have all become mass transfer-limiting, the corresponding steady state potential jumps from ~ – 1 V to ~ – 1.2 V regardless of the bath composition rather than decrease smoothly, unlike what is observed in other portions of the plot (notice the gap in data points where the steady state potential lies between ~ – 1 V and ~ – 1.2 V). Consequently, steady state potentials between ~ – 1 V and ~ – 1.2 V are never obtained in this system. As observed in the previous LSVs, the onset of water reduction occurs at approximately –1.05 V, whereas the re-activation of the electrode after

breakdown of the passivating film occurs at approximately –1.2 V (Figure 8.1). In order to explain the cause of the jump in steady state potential, it is important to realize that the data shown in Figure 8.10 have been obtained from galvanostatic experiments. The jump in potential occurs when the steady state potential reaches close to – 1 V, the passivating film has formed and a current density larger than the value corresponding to peak V is applied. As evident from the LSVs, it is not possible for the system to operate at such a current density without the film first breaking down to re-activate the electrode surface. The LSVs also show that this only occurs when the electrode potential has decreased to ~ –1.2 V. Faced with the demand for the imposed current density, the steady state electrode potential must jump to this value. The system is in an unstable condition at potentials between – 1 V and – 1.2 V during the LSV scans when the film is breaking down. Further support for this explanation comes from the observation that a jump in steady state potential never occurs in the case of bath 9 (Figure 8.10) which, as noted above, contains a very high $NiSO_4$ concentration. As shown in Figure 8.1, the LSV scan obtained in this bath does not exhibit peak V associated with the formation of the passivating film due to water reduction and its subsequent breakdown. This also suggests a dependence of the water reduction on the $NiSO_4$ and $CoSO_4$ bulk concentrations. When the reduction of Co(II), Ni(II) and H^+ become mass transport-limited, the contribution of water reduction becomes important since the other reactions are already proceeding as rapidly as possible. This effect is discussed in more detail in section 8.2.5 where the relation between the steady state potential, alloy composition and deposition current efficiency is analyzed.

8.2.3 Alloy composition

Probably the most representative measure of the anomalous behavior of Ni-Co alloys is their metal composition. Figures 8.11a-e show the effect of electrode potential on the weight percentages of both metals (denoted by the symbols) in the resulting alloy coating once steady state has been reached. These compositions were measured at the end of the experiments that yielded the current-potential data reported in Figure 8.10. Also shown as solid horizontal lines are the ratios $[Ni^{2+}]/([Ni^{2+}] + [Co^{2+}])$ and $[Co^{2+}]/([Ni^{2+}] + [Co^{2+}])$ expressed as percentages) in the plating baths from which the alloys are produced. The results obtained in plating baths 1, 3, 7, 8 and 9 considered previously in the steady state

cathodic polarization curves (section 8.2.2) and given in Table 8.1 are included in Figure 8.11a – e, respectively.

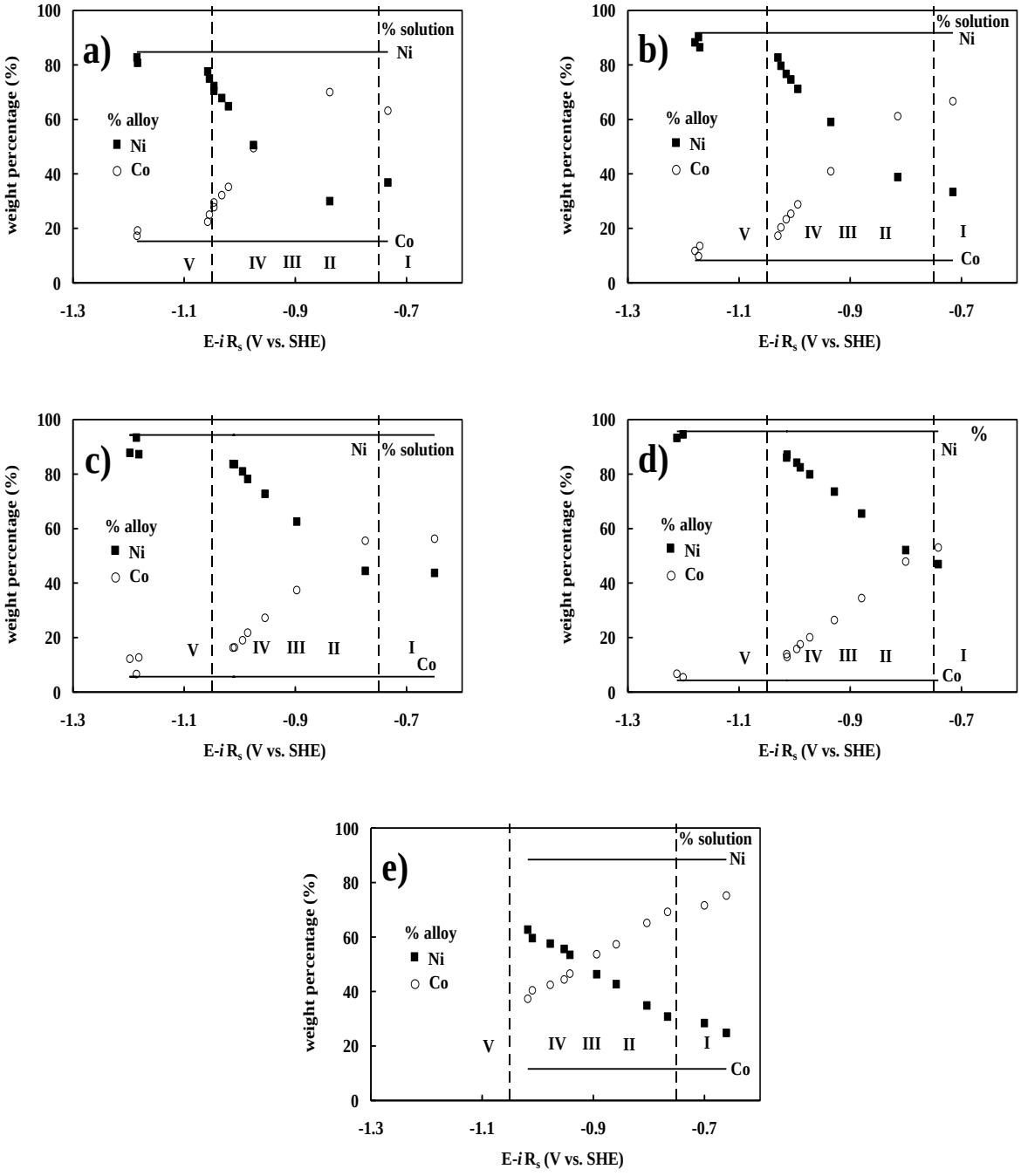

Figure 8.11. Weight percentages of nickel and cobalt in alloys (symbols) and in solution (continues line) formed on copper disk electrodes rotating at 1000 rpm in solutions containing 1500 mol m^{-3} Na_2SO_4, 500 mol m^{-3} $B(OH)_3$, and different concentrations of $NiSO_4$ and $CoSO_4$ (bath) reported in Table 8.1 at pH 3. a) bath 1, b) 3, c) 7, d) 8, and e) 9.

A comparison of these figures reveals that higher [Ni]/[Co] ratios in solution tend to promote regular behavior (i.e., non-anomalous) in the formation of the alloy and shift the steady state potentials in the positive direction. This effect is gradually promoted as the $NiSO_4$ concentration rises over the range from 100-400 mol m^{-3} (Figures 8.11a-d). Likewise, the nickel composition in the resulting alloy becomes closer to the $[Ni^{2+}]/([Ni^{2+}] + [Co^{2+}])$ ratio in solution as the $NiSO_4$ concentration increases. Comparison of the alloy compositions obtained in baths 1, 3, 7 and 8 (Figures 8.11a – d) to those obtained in bath 9 containing 1300 mol m^{-3} $NiSO_4$ and 170 mol m^{-3} $CoSO_4$ (Figure 8.11e) demonstrates the impact that the presence of Co(II) has on anomalous co-deposition. Although the $[Ni^{2+}]/([Ni^{2+}] + [Co^{2+}])$ ratio in solution steadily increases as one progresses from bath 1 to bath 8, the $CoSO_4$ concentration is kept fixed at 18 mol m^{-3}. On the other hand, the $CoSO_4$ concentration in bath 9 is much higher. Examination of Figure 8.11e shows that the resulting alloy compositions obtained in bath 9 tend to be richer in cobalt than those obtained in the other solutions at the same potentials. This suggests that no matter how high is the nickel concentration in solution, the system still exhibits anomalous behavior in which cobalt preferentially deposits if the amount of cobalt in solution is also high. However, it is worth mentioning that the preferential reduction of Co(II) is suppressed when it becomes mass transport-controlled and then the system follows regular behavior in which the cobalt composition in the alloy is very close to $[Co^{2+}]/([Ni^{2+}] + [Co^{2+}])$ in solution (see high overpotential regions in Figures 8.11a – d).

Figures 8.11a-e also show the general trend by which the cobalt content in the alloy decreases as the steady state potential becomes more negative. This trend is expected in view of the fact that mass transport plays an increasingly important role as the potential becomes more negative.

In order to explore the role of H^+ reduction and other aspects, the effect of the pH on the co-deposition of the Ni-Co alloys is considered in the next section.

8.2.4 Effect of pH

A few studies on the effect of pH on the Fe-Ni and Ni-Co systems were carried out some years ago [85, 90, 97, 100]. In general, these showed that the content of iron or cobalt (less noble component) produced in the alloy increases slightly as the pH is reduced. The variation of the alloy content with steady state potential at pH 2, 3 and 4 obtained in the present study

is shown in Figures 8.12a, 8.11b and 8.12b, respectively, at the same $NiSO_4$ (200 mol m^{-3}) and $CoSO_4$ (18 mol m^{-3}) concentrations. The trends shown here agree with those reported by these earlier researchers for conditions of high overpotentials (e.g. mixed and mass-transport controlled regions), although the effect is very small. However, where a difference from these previous studies is observed is at low applied current where the opposite behavior is exhibited, i.e., less cobalt is deposited in the alloy as the pH is lowered. As discussed previously, H^+ and Ni(II) reduction tend to be the predominant cathodic reactions at lower current densities on the order of –50 to –100 A m^{-2} (lower overpotentials). When the pH is 2, H^+ reduction should be particularly dominant and very little cobalt deposition should occur at low currents. An increase in pH to 3 and 4 obviously leads to less H^+ reduction, leaving more current for both nickel and cobalt deposition during these galvanostatic experiments. More Co(II) reduction inevitably leads to more anomalous behavior during deposition and higher cobalt content in the alloy (refer to Figures 8.11b and 8.12b). Thus, although the conclusion from previous studies has been that hydrogen evolution does not play much of a role in anomalous deposition of iron-group alloys, the results in Figures 8.11 and 8.12 indicate that H^+ reduction has an effect at low overpotentials. This effect is likely due to competition for the available current and adsorption sites rather than a direct effect on the metal deposition reactions themselves.

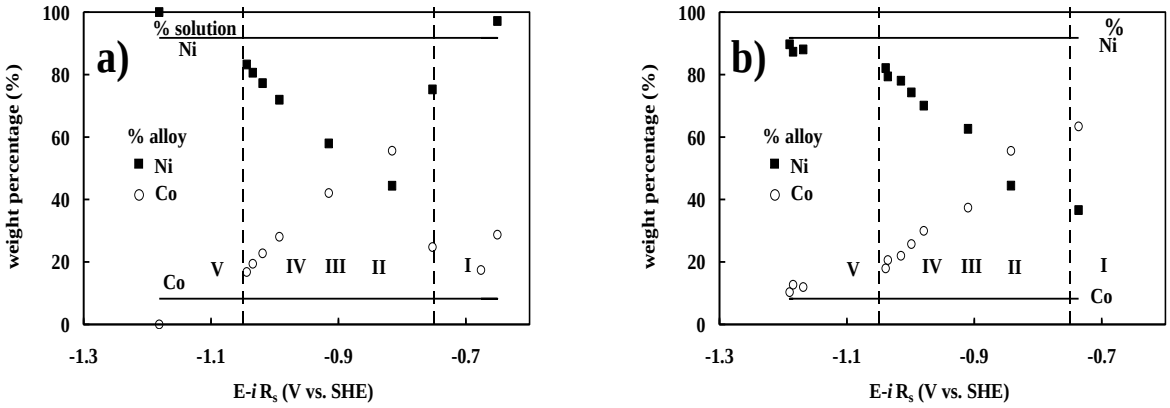

Figure 8.12. Weight percentages of nickel and cobalt in alloys (symbols) and in solution (continues line) formed on copper disk electrodes rotating at 1000 rpm in solutions containing 1500 mol m^{-3} Na_2SO_4, 500 mol m^{-3} $B(OH)_3$, and 200 mol m^{-3} $NiSO_4$ + 18 mol m^{-3} $CoSO_4$ at different pH values: a) 2 and b) 4.

8.2.5 Deposition current efficiency

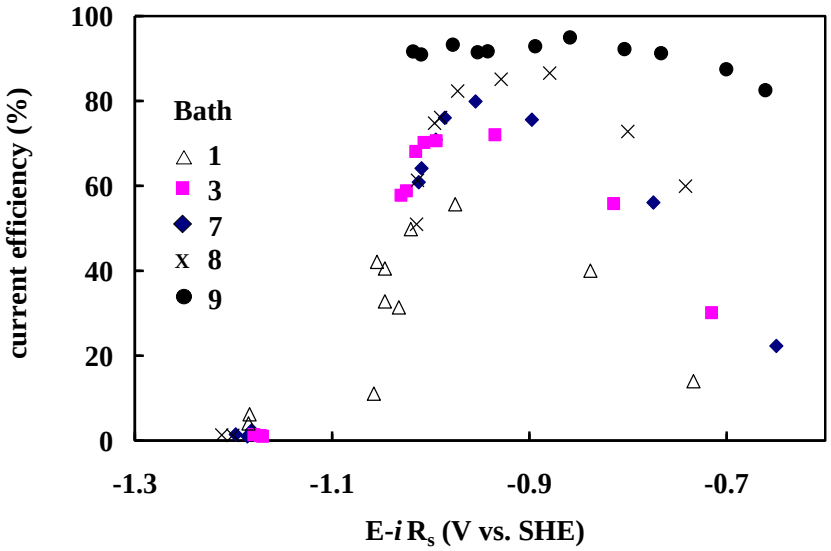

Figure 8.13. Experimental current efficiency obtained on copper disk electrodes rotating at 1000 rpm in solutions containing 1500 mol m^{-3} Na_2SO_4, 500 mol m^{-3} $B(OH)_3$, and different concentrations of $NiSO_4$ and $CoSO_4$ (bath) reported in Table 8.1 at pH 3.

The deposition current efficiency (%) measures the percentage of the total charge used for the reduction of both Co(II) and Ni(II) during the deposition process. As a result, it reflects the contribution of hydrogen evolution (e.g. H^+ and water reduction) to the total current density generated in the system. In order to calculate this current efficiency obtained during the galvanostatic experiments, a ratio of the total mass (i.e. cobalt and nickel) deposited to the theoretical mass calculated with Faraday's law assuming no hydrogen evolution occurs has been determined. Figure 8.13 shows the results obtained for the various baths included in this study (Table 8.1). Not surprisingly, higher $NiSO_4$ and $CoSO_4$ concentrations in solution lead to less input from the HER and an increase in deposition current efficiency. The deposits produced under these conditions appear bright to the naked eye with no visual evidence of the formation of oxides on the surface. Perhaps the most notable feature of the plots in Figure 8.13 (with the exception of the curve for bath 9) is the general trend in which the current efficiency is small at low overpotentials, increases as the overpotential rises to intermediate values before dropping sharply at high overpotentials. The sharp decline in current efficiency at high overpotentials coincides with the potentials where peak V appears in the LSV scans and where some sort of an oxide film forms. This is

confirmed by visual inspection of the coatings produced under these conditions. The coatings appear gray and dull when the steady state potential reaches approximately –1 V; the coatings darken considerably at more negative potentials, presumably due to the massive formation of oxides.

At low overpotentials, H^+ reduction is the main reaction before Ni(II) and Co(II) reduction have been completely activated. As the current is increased and the potential becomes more negative, the *ce* increases due to the onset of Ni(II) and Co(II) reduction. Once these reactions become mass transfer-limited at approximately –1 V, the current efficiency drops as a result of the onset of water reduction.

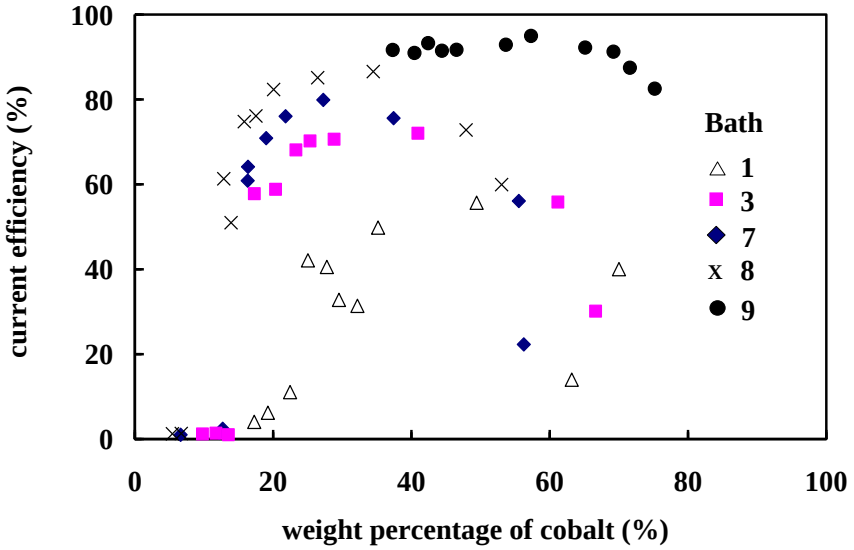

Figure 8.14. Experimental current efficiency as a function of the weight percentage of cobalt in alloys formed on copper disk electrodes rotating at 1000 rpm in solutions containing 1500 mol m^{-3} Na_2SO_4, 500 mol m^{-3} $B(OH)_3$, and different concentrations of $NiSO_4$ and $CoSO_4$ (bath) reported in Table 8.1 at pH 3.

As discussed above, a relationship between the anomalous co-deposition behavior and the contribution of the hydrogen evolution reaction is found to occur at low overpotentials. To date, this effect has not been noted since most of the studies conducted have not focused on the correlation between the content of cobalt in the alloy and the current efficiency. In order to examine this relationship more closely, the deposition current efficiency is plotted versus the weight percentage of cobalt in the alloy for the different baths in Figure 8.14. It is evident from this plot that the lowest amount of cobalt in the alloy is

produced when the current efficiency is virtually zero. This occurs at high overpotentials where cobalt deposition is mass-transport controlled and water reduction takes place. However, a condition of low current efficiency does not imply that low cobalt content in the alloy is always produced. As shown in Figure 8.14, cobalt-rich alloys can also be obtained when the current efficiency is low, but in this case the phenomenon occurs at low overpotentials due to the competition between Co(II) reduction and H^+ reduction.

8.2.6 Proposed reaction mechanism

On the basis of the results of this study and others reported in the literature [42, 66, 88, 91, 95, 96], we propose the following reaction mechanism for the regions I – V defined previously with regard to the LSVs measured during the co-deposition of Ni-Co alloys in acidic sulphate solutions buffered with boric acid (i.e. Figure 8.1):

$H^+ + e^- \rightarrow H_{ads}$ } **I**

$2H_{ads} \rightarrow H_2$

$Ni(II) + e^- \rightarrow Ni(I)_{ads}$ } **II**

$Ni(I)_{ads} + e^- \rightarrow Ni^0$

$Co(II) + e^- \rightarrow Co(I)_{ads}$ } **III**

$Co(I)_{ads} + e^- \rightarrow Co^0$

Inhibition of the nickel deposition & } **IV**

Acceleration of the cobalt co-deposition

$H_2O + e^- \rightarrow H_{ads} + OH^-$

$Me^{2+} + 2H_2O \rightarrow Me(OH)_{2(s)} \downarrow + 2H^+$

$Me(OH)_{2(s)} \downarrow \rightarrow MeO_{(s)} \downarrow + H_2O$ } **V**

The parentheses imply that the each region includes all the reactions preceding it as well.

During a cathodic scan, H^+ reduction is the first prominent reaction to take place on the surface of the electrode at more positive potentials. This reaction is followed by nickel deposition and soon after by Co(II) reduction and co-deposition of the alloy. At more negative potentials, the anomalous behavior could occur as a result of three different effects (that will be discussed and scrutinized when modeling of alloy formation is considered in

Chapter 9): catalysis of Co(II) reduction and simultaneous inhibition of Ni(II) reduction [42], preferential surface coverage of $Co(I)_{ads}$ over $Ni(I)_{ads}$ on the surface of the electrode [43] or a faster rate of charge transfer for Co(II) reduction in comparison with that of Ni(II) reduction. As previously proposed [42], the first effect could involve the formation of a mixed intermediate species adsorbed on the electrode (i.e. $NiCo(III)_{ads}$), whereas the second effect would entail the perpetuation of $Co(I)_{ads}$ on the surface.

At a given $CoSO_4$ concentration, nickel deposition is inhibited but not completely blocked, something which is partly counteracted when the $NiSO_4$ concentration in solution is increased. Some dependence of alloy co-deposition on pH is observed at low overpotentials where H^+ reduction can successfully compete with Co(II) and Ni(II) reduction. Water reduction becomes significant once alloy co-deposition becomes mass-transfer-limited. This leads to a significant rise in the surface pH and the formation of a film that tends to be passivating (e.g. hydroxides, oxides) and suppress the electrode response. Once the potential decreases below ~ –1.15 V, this film breaks down to re-activate the electrode surface. The presence of $B(OH)_3$ in the bath has a significant effect on the electrode response in this potential region presumably due to its effect on the formation of the film. The evidence suggests that the film forms earlier during the scan when the buffer is absent than when it is present although it is important to note that the film is never completely passivating regardless of the solution composition and always permits significant current to flow. Once the film breaks down, the electrode response in the presence of $B(OH)_3$ becomes identical to that in its absence, suggesting that the states of the electrode surfaces in the two cases have become very similar.

A higher [Ni(II)]/[Co(II)] ratio in solution promotes normal-type alloy co-deposition at more positive potentials. However, it appears that the anomalous behavior is ultimately determined by the $CoSO_4$ concentration since Co(II) reduction remains favoured over Ni(II) reduction (i.e. presumably faster adsorption and/or charge transfer) until it becomes limited by mass transport. At this point, the nickel content in the alloy can increase significantly as long as its deposition is also not transport-controlled. However, this situation requires that the Ni(II) concentration in solution be maintained much larger than that of Co(II).

Evidence for anomalous behavior during alloy co-deposition is observed for conditions where H^+ reduction is not mass transport-controlled. Thus, it is not necessary for H^+ reduction to be mass transfer-limited in order for anomalous behavior to be observed, as has been proposed in the past. Experiments on the effect of pH on the resulting alloy

composition show that Co(II) reduction is suppressed by hydrogen evolution at low overpotentials particularly when the pH is 2, presumably due to competition for current and sites on the electrode surface.

Higher $NiSO_4$ and $CoSO_4$ concentrations in solution reduce the extent of the HER and as a consequence cause the current efficiency for metal deposition to increase. This current efficiency is small at both low and high overpotentials due to competition from H^+ and water reduction. The lowest amount of cobalt in the alloy is produced at high overpotentials when very little metal whatsoever is deposited. On the other hand, conditions of low deposition current efficiency can also lead to cobalt-rich alloys, but this occurs under kinetically-controlled conditions when Co(II) reduction dominates over Ni(II) reduction in competition with H^+ reduction.

Chapter 9 Steady-state model of Ni-Co alloy electrodeposition in sulphate media

9.1 Introduction

As with other iron-group alloy systems, Co-Ni alloy electrodeposition exhibits anomalous behaviour in that cobalt is preferentially deposited over nickel even when the Ni(II) concentration is significantly higher than that of Co(II) in the bulk solution. This observation has motivated considerable research into this topic for many years. Several experimental and modeling studies [15, 42, 81-89] have been conducted to analyse this system and gain a better understanding of the factors controlling the amount of metal that is deposited and the composition of the resulting alloy. Alloy composition is crucial because it determines the properties (e.g. corrosion resistance, magnetic saturation, hardness, wear) associated with the material. To date, the composition has been determined empirically through experimental work, although a number of models have been presented to account for the electrode kinetics in the system and predict the metal percentages in these iron-group alloys (e.g. Fe-Ni, Fe-Co, Co-Ni) [42, 43, 86, 90, 91, 93, 94, 101].

Hessami and Tobias [94] acknowledged the complexity of this system and suggested that the hydrolysis of the metal ions plays an important role in anomalous co-deposition. They proposed a model accounting for diffusion, convection and the hydrolysis of Fe^{2+}, Ni^{2+} and water. The overall current density of the system is made up of contributions from the hydrogen evolution reaction (e.g. H^+ and water reduction in single 2-electron transfer steps) and co-deposition of iron and nickel through the reduction of $FeOH^+$, $NiOH^+$, Fe^{2+} and Ni^{2+}. Alloy co-deposition is considered to occur via 2-electron transfer steps for the reduction of Fe^{2+} and Ni^{2+} that takes place over the entire surface and competitive reduction of the metal hydroxides that occurs on surface sites. Sasaki and Talbot [93] stressed the importance of $MeOH^+$ in the formation of iron-group alloys and their incorporation in the electrodeposition mechanism. However, one factor not considered by these authors is that soluble metal sulphates and chlorides are the predominant species in the chloride and sulfate baths used in these studies rather than Fe^{2+}, Ni^{2+}, $FeOH^+$ and $NiOH^+$ [41, 51, 66, 95, 96]. For these reasons, the importance of metal hydrolysis is unclear and may not be responsible for the anomalous behaviour. Moreover, it is difficult to determine if the observed anomalous behaviour is

consistent with thermodynamic predictions since no data are available for adsorbed surface species.

On the other hand, Matlosz [43] proposed a model for co-deposition of Fe-Ni alloys based on the preferential surface coverage by the adsorbed iron-intermediate species due to differences in the kinetics of electrosorption, which has the effect of inhibiting the more noble nickel. This model considers the formation of adsorbed monovalent intermediates produced during the reduction of the dissolved metal species via consecutive 1-electron transfer steps. The model calculations suggested that changes in surface pH are not required for anomalous co-deposition to produce iron-rich deposits. Normal deposition in which nickel deposition is not inhibited was shown to occur at low overpotentials, whereas more iron-rich deposits are produced at higher overpotentials. Matlosz also suggested that the kinetics of Ni^{2+}, Fe^{2+} and H^{+} reduction are essentially uncoupled and may be treated separately.

A model that more comprehensively captures the phenomena occurring during co-deposition of iron-group metals was provided by Zech et al. [42, 89]. They compared the measured partial current densities of the metals co-depositing during the formation of the alloy with deposition of the single metals alone. Their results demonstrated that not only is Ni deposition inhibited in the presence of Fe^{2+} and Co^{2+} ions during alloy formation, but also the deposition of the less noble metal is accelerated, i.e. iron deposition rate is enhanced by Co^{2+} and Ni^{2+} ions [42, 89]. The inhibiting effect is generally stronger when the reaction rate of the less noble metal is kinetically controlled and diminishes as the limiting current is reached. In view of these findings, they derived a model considering the acceleration of the co-deposition of the less noble component and the inhibition of the more noble one [42]. The model accounts for three parallel reactions occurring in 1-electron transfer steps: reduction of the more noble (reactions 6.1 and 6.2) and less noble components (reactions 5.1 and 5.2) by independent reactions and catalytic-inhibiting reduction reactions in which the two components interact with each other (reactions 9.1 and 9.2). These reaction pathways involve the formation of adsorbed species on the surface of the electrode (e.g. reactions 6.2, 5.2 and 5), the last of which yields a mixed intermediate species containing both metal ions (*i.e.* $\mathrm{Ni\,Co\,(III)_{ads}}$).

$$\mathrm{Ni\,(II) + Co\,(II) + e^- \rightarrow Ni\,Co\,(III)_{ads}} \qquad (9.1)$$

$$\mathrm{Ni\,Co\,(III)_{ads} + e^- \rightarrow Co^0 + Ni\,(II)} \qquad (9.2)$$

Reactions (9.1) and (9.2) can be considered to be catalytic for Co(II) reduction in that they provide another pathway to deposit cobalt, but are inhibitory toward nickel deposition in that the Ni(II) involved is never reduced and the $\mathrm{NiCo(III)_{ads}}$ adsorbed intermediate can block sites otherwise available to $\mathrm{Ni(I)_{ads}}$ (and $\mathrm{Co(I)_{ads}}$). This model also considers side reactions due to H^+ and water reduction via 1-electron transfer steps and mass-transport by diffusion.

To date, this is the most comprehensive analysis of anomalous behaviour. However, as stressed by these authors [42], some gaps particularly with regard to the quantitative prediction of alloy composition exist in their model. One of these aspects is associated with role played by the HER in the co-deposition of the metals. From previous studies [41, 51, 66, 93, 96] conducted on deposition of the single metals Co, Ni and Fe, it is acknowledged that the HER involves the formation of an adsorbed species (i.e. H_{ads}) not considered in the model of Zech et al. [40], i.e., (reactions 5.3). H_{ads} can block active sites on the surface of the electrode that can otherwise be occupied by $\mathrm{Ni(I)_{ads}}$, $\mathrm{Co(I)_{ads}}$ and $\mathrm{NiCo(III)_{ads}}$. Given the importance of the competition between the different adsorbed species, this interaction may be significant and its effects should be considered. Reaction (5.3) tends to increase the pH at the electrode/solution interface and eventually can become limited by mass transfer, particularly when carried out at higher overpotentials [66, 95, 96]. These conditions can lead to a third cathodic reaction in which water itself is reduced by the reaction (5.5) [66, 95, 96]. The role of water reduction during the deposition of iron-group metals has been investigated in only a few studies [40, 88]. In addition, the buffering effect due to the addition of boric acid (i.e. typically added to iron-group metal baths) has not been studied and modelled during the co-deposition of these alloys. In single metal deposition of Co and Ni [66, 95, 96], these effects have been found to be very important since the calculated surface pH tends to be overestimated when they are not included. A similar situation should also exist during the co-deposition of Co-Ni alloys and so these phenomena should also be included in the model. Also, since most of the deposition studies have been conducted using a rotating disk electrode, convective mass transport becomes important and should also be considered. Another important limitation of these previous studies is that the models were not quantitatively and/or fit to experimental data. A least-square fit would enable the model parameters to be estimated with greater accuracy and better insight into the behaviour of the system to be gained.

Therefore, this study presents a comprehensive model accounting for the aforementioned phenomena in order to improve the understanding of the anomalous behaviour occurring during the co-deposition of Co-Ni alloys in a typical acidic sulphate-borate electrolyte (1500 mol m^{-3} Na_2SO_4, 500 mol m^{-3} $B(OH)_3$). More detailed electrode kinetics, homogeneous reactions (i.e., water hydrolysis, borate equilibrium) and mass-transport by diffusion and convection are considered. This study focuses on the effect of the $NiSO_4/CoSO_4$ concentration ratio (i.e., 200/100, 100/50 and 50/50) on alloy deposition at pH 3. The model is fit (least-square) to experimental steady state polarization curves to determine accurate model parameters of the system (electrode kinetic parameters and diffusion coefficients) for the various conditions considered. The experimental data to which the model is fit are alloy composition, partial current densities and metal deposition current efficiencies.

9.2 Modeling

9.2.1 Mechanism and kinetics

The physicochemical model used to describe the steady-state response obtained during the polarization experiments is presented in this section. This model is consistent with the solution thermodynamics presented in sections 5.2.1 and 6.2.1 considering all the possible Co(II) (Figure 5.1) and Ni(II) (Figure 6.1) species that co-exist in sulphate media buffered with boric acid [18-21]. The reaction mechanism for Ni(II) and Co(II) reduction, catalysis of cobalt co-deposition and inhibition of nickel inhibition presented in this section is based on previous studies of deposition of iron-group metals [9, 15-21]. The assumptions and formulation of the mass transport equations are provided in section 9.2.2.

Co(II) and Ni(II) reduction are considered to proceed via consecutive 1-electron transfer steps given by reactions (5.1) to (6.1) without the assumption as to which is rate-controlling. No evidence for the formation of a stable dissolved Ni(I) and Co(I) species has been reported in any modeling or experimental work reported in the literature [9, 15-21]. Thus, no such species are considered in the reaction mechanism. The effects of the catalysis of cobalt deposition and simultaneous inhibition of nickel deposition are described by reactions (9.1) and (9.2). Under this scheme, this is mediated by the formation of a mixed intermediate species $\mathrm{Ni\,Co\,(III)_{ads}}$ on the surface of the electrode. The model considers that

HER takes place concomitantly with the co-deposition of cobalt and nickel via H^+ (reaction 5.3) and water (reaction 5.5) reduction. Both these reactions occur by Volmer-type mechanisms and generate H_{ads} on the electrode surface which block active sites that otherwise could be occupied by $Ni(I)_{ads}$, $Co(I)_{ads}$ or $NiCo(III)_{ads}$ species. The consumption of the H_{ads} species proceeds by their chemical combination to form H_2 molecules (reaction 5.4). The reduction of water molecules furnishes H_{ads} species to the surface of the electrode at high overpotential or low metallic concentration. Based on previous studies on single metal deposition, the amount of $B(OH)_3$ that adsorbs is negligibly small and so is ignored in the model [18, 19].

Assuming Langmuir adsorption behavior for $Ni(I)_{ads}$ and $Co(I)_{ads}$ and neglecting the reverse direction of the electrode reactions, we can write the following expression for the current density i_{Ni} associated with nickel deposition (reactions 6.1 and 6.2):

$$i_{Ni} = -F\left(r_{1Ni} + r_{2Ni}\right) = -F\left[\begin{array}{l} k_{01Ni}\ \exp\left(-\alpha_{Ni1}\dfrac{FE'}{RT}\right)\ C^{s}_{Ni(II)}\left(1-\theta_{Ni}-\theta_{Co}-\theta_{H}-\theta_{A}\right) \\ \\ +\ k_{02Ni}\ \exp\left(-\alpha_{Ni2}\dfrac{FE'}{RT}\right)\theta_{Ni} \end{array}\right] \qquad (9.3)$$

and i_{Co} for cobalt deposition (reactions 5.1 and 5.2):

$$i_{Co} = -F\left(r_{1Co} + r_{2Co}\right) = -F\left[\begin{array}{l} k_{01Co}\ \exp\left(-\alpha_{Co1}\dfrac{FE'}{RT}\right)C^{s}_{Co(II)}\left(1-\theta_{Ni}-\theta_{Co}-\theta_{H}-\theta_{A}\right) \\ \\ +\ k_{02Co}\ \exp\left(-\alpha_{Co2}\dfrac{FE'}{RT}\right)\theta_{Co} \end{array}\right] \qquad (9.4)$$

The current density i_A for the simultaneous catalysis of cobalt deposition and inhibition of nickel deposition (reactions 9.1 and 9.2) can be described as follows:

$$i_{A} = -F\left(r_{1A} + r_{2A}\right) = -F\left(\begin{array}{l} k_{01A}\ \exp\left(-\alpha_{A1}\dfrac{FE'}{RT}\right)C^{s}_{Co(II)}C^{s}_{Ni(II)}\left(1-\theta_{Ni}-\theta_{Co}-\theta_{H}-\theta_{A}\right)^{2} \\ \\ +\ k_{02A}\ \exp\left(-\alpha_{A2}\dfrac{FE'}{RT}\right)\theta_{A} \end{array}\right) \qquad (9.5)$$

The $\left(1-\theta_{Ni}-\theta_{Co}-\theta_{H}-\theta_{A}\right)^{2}$ term appears in Eq (9.5) to account for the fact that $NiCo(III)_{ads}$ occupies two empty surface sites. The current density i_{HER} due to H^+ (reaction 5.3) and water reduction (reaction 5.5) is given by the following expression (also ignoring the reverse direction of each step):

$$i_{HER} = -F(r_{1H} + r_{1W}) = -F\left[\begin{array}{l} k_{01H}\ \exp\left(-\beta_H \dfrac{FE'}{RT}\right) C_H^s \\ +\ k_{01W}\ \exp\left(-\beta_W \dfrac{FE'}{RT}\right) \end{array}\right](1 - \theta_{Ni} - \theta_{Co} - \theta_H - \theta_A) \qquad (9.6)$$

Under steady-state conditions, the material balances for the rates of formation of $Ni(I)_{ads}$, $Co(I)_{ads}$, $NiCo(III)_{ads}$ and H_{ads} on the active surface sites are respectively:

$$r_{1Ni} - r_{2Ni} = 0 \qquad (9.7)$$

$$r_{1Co} - r_{2Co} = 0 \qquad (9.8)$$

$$r_{1A} - r_{2A} = 0 \qquad (9.9)$$

$$r_{1H} + r_{1W} - 2r_{2H} = 0 \qquad (9.10)$$

where $r_{2H} = k_{2H}\theta_H^2$ is the rate of chemical combination of H_{ads} by reaction (5.4). In Eqs. (9.3) – (9.10), $C^s_{Ni(II)}$, $C^s_{Co(II)}$ and C^s_H represent the surface concentrations of Ni(II), Co(II) and H^+, respectively, while θ_{Ni}, θ_{Co}, θ_A and θ_H are the fractions of the electrode area covered by $Ni(I)_{ads}$, $Co(I)_{ads}$, $NiCo(III)_{ads}$ and H_{ads}, respectively. k_{01Ni}, k_{02Ni}, k_{01Co}, k_{02Co}, k_{01A}, k_{02A}, k_{01H}, k_{2H} and k_{01W} are rate constants and $\alpha_{Ni1}, \alpha_{Ni2}, \alpha_{Co1}, \alpha_{Co2}, \alpha_{A1}, \alpha_{A2}, \beta_H$ and β_W are charge transfer coefficients for reactions (5.1)–(5.3), (5.5), (6.1), (6.2), (9.1) and (9.2). E' is the electrode potential corrected for the electrolyte ohmic resistance R_s (equation 3.2). The total current density i_T is composed of the partial current densities:

$$i_T = i_{Ni} + i_{Co} + i_A + i_{HER} \qquad (9.11)$$

9.2.2 Development of transport model

The same assumptions considered in section 5.3.2 are made in the present model to develop the transport equations applicable to a rotating disk working electrode. Coupling of the steady state transport equations for these species to the homogeneous reactions within the region $0 < y < 3\delta$ yields:

$$-\nabla \cdot N_{Ni(II)} = 0 \qquad (9.12)$$

$$-\nabla \cdot N_{Co(II)} = 0 \qquad (9.13)$$

$$-\nabla \cdot N_{H^+} + \nabla \cdot N_{OH^-} + \nabla \cdot N_{B_3O_3(OH)_4^-} = 0 \qquad (9.14)$$

$$-\nabla \cdot N_{B(OH)_3} - 3\nabla \cdot N_{B_3O_3(OH)_4^-} = 0 \qquad (9.15)$$

where the 1-dimensional flux N_j is described by equation (5.13). The following algebraic equations describing the equilibria of the homogeneous reactions (water dissociation and boric acid hydrolysis) apply everywhere within the boundary layer and complete the system of equations to be solved:

$$C_{OH^-} C_{H^+} - \beta_{H_2O} = 0 \qquad (9.16)$$

$$\frac{C_{B_3O_3(OH)_4^-} C_{H^+}}{(C_{B(OH)_3})^3} - \beta_{3B} = 0 \qquad (9.17)$$

The boundary condition at the outer edge $y = 3\delta$ of the region being modeled is given by:

$$C_j(3\delta) = C_j^b \qquad (9.18)$$

where C_j^b is the bulk concentration of species j. The boundary conditions at the electrode surface are:

$$D_{Ni(II)} \frac{\partial C_{Ni(II)}}{\partial y}\bigg|_{y=0} - r_{1Ni} - r_{1A} + r_{2A} = 0 \qquad (9.19)$$

$$D_{Co(II)} \frac{\partial C_{Co(II)}}{\partial y}\bigg|_{y=0} - r_{1Co} - r_{1A} = 0 \qquad (9.20)$$

$$D_H \frac{\partial C_H}{\partial y}\bigg|_{y=0} - D_{OH^-} \frac{\partial C_{OH^-}}{\partial y}\bigg|_{y=0} - D_{B_3O_3(OH)_4^-} \frac{\partial C_{B_3O_3(OH)_4^-}}{\partial y}\bigg|_{y=0} - r_{1H} - r_{1W} = 0 \qquad (9.21)$$

$$D_{B(OH)_3} \frac{\partial C_{B(OH)_3}}{\partial y}\bigg|_{y=0} + 3 D_{B_3O_3(OH)_4^-} \frac{\partial C_{B_3O_3(OH)_4^-}}{\partial y}\bigg|_{y=0} = 0 \qquad (9.22)$$

The equilibria described in Eqs. (9.16) and (9.17) also apply at y = 0 and in the bulk solution.

9.2.3 Numerical method for solution of model equations and parameter estimation

Numerical values for the rate constants (k_{01Ni}, k_{02Ni}, k_{01Co}, k_{02Co}, k_{01A}, k_{02A}, k_{01H}, k_{2H} and k_{01W}), transfer coefficients ($\alpha_{Ni1}, \alpha_{Ni2}, \alpha_{Co1}, \alpha_{Co2}, \alpha_{A1}, \alpha_{A2}, \beta_H$ and β_W) and diffusion coefficients ($D_{Ni(II)}, D_{Co(II)}$ and D_H) are estimated by least-square fitting the model to the experimental steady state polarization curves. This involves the combination of standard methods for parameter estimation with the numerical solution of the model equations

presented in the previous sections. The system of ODEs, algebraic expressions and boundary conditions given in Eqs. (10–33) has been solved using the finite element method in the COMSOL Multiphysics® 3.5a software package [102]. A second-order Lagrange quadratic polynomial is used as the shape function.

The model is fit (least-square) to the experimental data to obtain parameter estimates by minimization of the sum-of-squares error between the model predictions and data defined by the fitness function below using Matlab® *R2009b* toolbox [103]:

$$\text{Fitness Function} = \sum \left[\left(i_{Ni}^{model} - i_{Ni}^{experimental} \right)^2 + \left(i_{Co}^{model} + i_{A}^{model} - i_{Co}^{experimental} \right)^2 + \left(i^{model} - i^{experimental} \right)^2 \right] \quad (9.23)$$

where i^{model} and i_j^{model} are the model-predicted total and partial current densities, respectively, $i^{experimental}$ is the experimental total current density obtained from the cathodic polarization curves and $i_i^{experimental}$ are the experimental partial current densities obtained from chemical analysis of the resulting alloy composition. It is important to emphasize that the quantities $i^{experimental}$, $i_{Ni}^{experimental}$ and $i_{Co}^{experimental}$ were measured independently from one another on the basis of the potentiometry experiments for the total current ($i^{experimental}$) and ICP measurements of the Ni and Co content in the resulting deposits (refer to section 4.3) ($i_{Ni}^{experimental}$ and $i_{Co}^{experimental}$). An Intel Core i7 CPU running at 3.07 GHz with a RAM memory of 12.00 GB is used to carry out the calculations. This procedure typically requires a duration of about 8 hours to obtain a good fit for each polarization curve.

Table 9.1. Electrolyte compositions used in this study for Ni-Co alloy co-deposition in a supporting electrolyte (SE) containing 1500 mol m^{-3} Na_2SO_4 and 500 mol m^{-3} $B(OH)_3$ at pH 3.

Bath	[$NiSO_4$] (mol m^{-3})	[$CoSO_4$] (mol m^{-3})
1	200	100
2	100	50
3	50	50

9.2.4 Model fitting and discussion

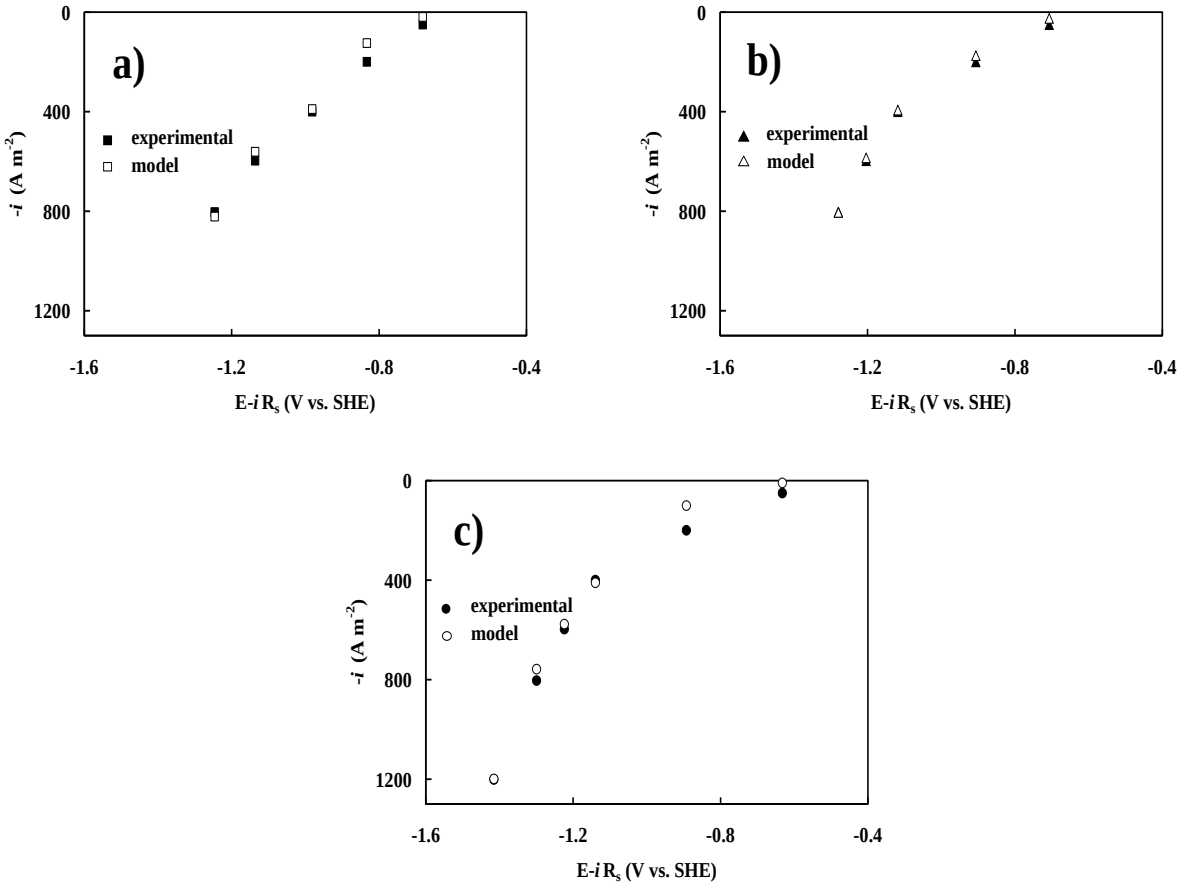

Figure 9.1. Experimental (black symbols) and model-fitted (open symbols) steady-state polarization curves on a copper substrate rotating at 1000 rpm in solutions containing 1500 mol m^{-3} Na_2SO_4, 500 mol m^{-3} $B(OH)_3$ and different concentration ratios of $NiSO_4/CoSO_4$: a) 200/100, b) 100/50 and c) 50/50 at pH 3. The computed curves are generated using parameters listed in Tables 9.2 and 9.3.

Figure 9.1 shows a comparison of experimental (black symbols) and model-fitted (open symbols) cathodic polarization curves recorded in solutions containing 1500 mol m^{-3} Na_2SO_4, 500 mol m^{-3} $B(OH)_3$ at pH 3 and the following molar concentration ratios of $NiSO_4/CoSO_4$: a) 200/100, b) 100/50 and c) 50/50 (refer to Table 9.1). The experimental curves are obtained from the galvanostatic experiments by monitoring the resulting electrode

potential until steady state is attained. The duration of each galvanostatic experiment is set to ensure that the total charge transferred is limited to 1.5 C. The fitting of the model presented in section 9.2 yields the kinetic parameters and diffusion coefficients reported in Tables 9.2 and 9.3, respectively. Kinetic parameters for the second step of nickel and cobalt deposition ($k_{02\,Ni}, \alpha_{Ni\,2}, k_{02\,Co}, \alpha_{Co\,2}$) are not reported in Table 9.2 because the model was found to have little or no sensitivity to their values and so could not be determined with good certainty.

Table 9.2. Kinetic parameters obtained from fitting the model to experimental steady-state polarization data at different concentration ratios of $NiSO_4/CoSO_4$.

Bath	$k_{01\,Co}$ (10^{-13} m s^{-1})	$\alpha_{Co\,1}$	$k_{01\,Ni}$ (10^{-15} m s^{-1})	$\alpha_{Ni\,1}$	$k_{01\,H}$ (10^{-10} m s^{-1})	$k_{2\,H}$ (10^{-2} mol m^{-2} s^{-1})	β_H	$k_{0\,W}$ (10^{-14} mol m^{-2} s^{-1})	β_W
1	7.95	0.5	1.92	0.48	8.18	2.19	0.49	1.86	0.49
2	9.35	0.5	1.74	0.5	5.91	1.71	0.5	7.77	0.49
3	3.16	0.5	1.64	0.5	6.57	1.49	0.5	1.69	0.5

Table 9.3. Diffusion coefficients obtained from fitting the model to experimental steady-state polarization data at different concentration ratios of $NiSO_4/CoSO_4$.

Bath	$D_{Ni\,(II)}$ (10^{-10} m^2 s^{-1})	$D_{Co\,(II)}$ (10^{-10} m^2 s^{-1})	D_H (10^{-9} m^2 s^{-1})
1	0.83	1.95	5.83
2	0.95	2.41	9.23
3	1.64	2.74	9.35
	υ	1.5 x 10^{-6} m^2 s^{-1}	
	R_s	~1.5 x 10^{-4} ohm m^2	

As observed for the three different experimental conditions analyzed, very good fits are obtained over the entire range of potentials. It is important to note that the model has been fit to the data for each bath one at a time since this yields considerably better results than

when the model is fit simultaneously to the data for the three different conditions to obtain a single set of parameters. In view of previous studies [41, 51, 66, 105, 106], this is not surprising since the kinetic parameters and diffusion coefficients have been shown to depend on electrolyte composition and electrode potential. Not surprisingly, a comparison of the three plots shown in Figure 1 reveals that the total current at any given potential rises as the Ni(II) and Co(II) concentrations in solution increases.

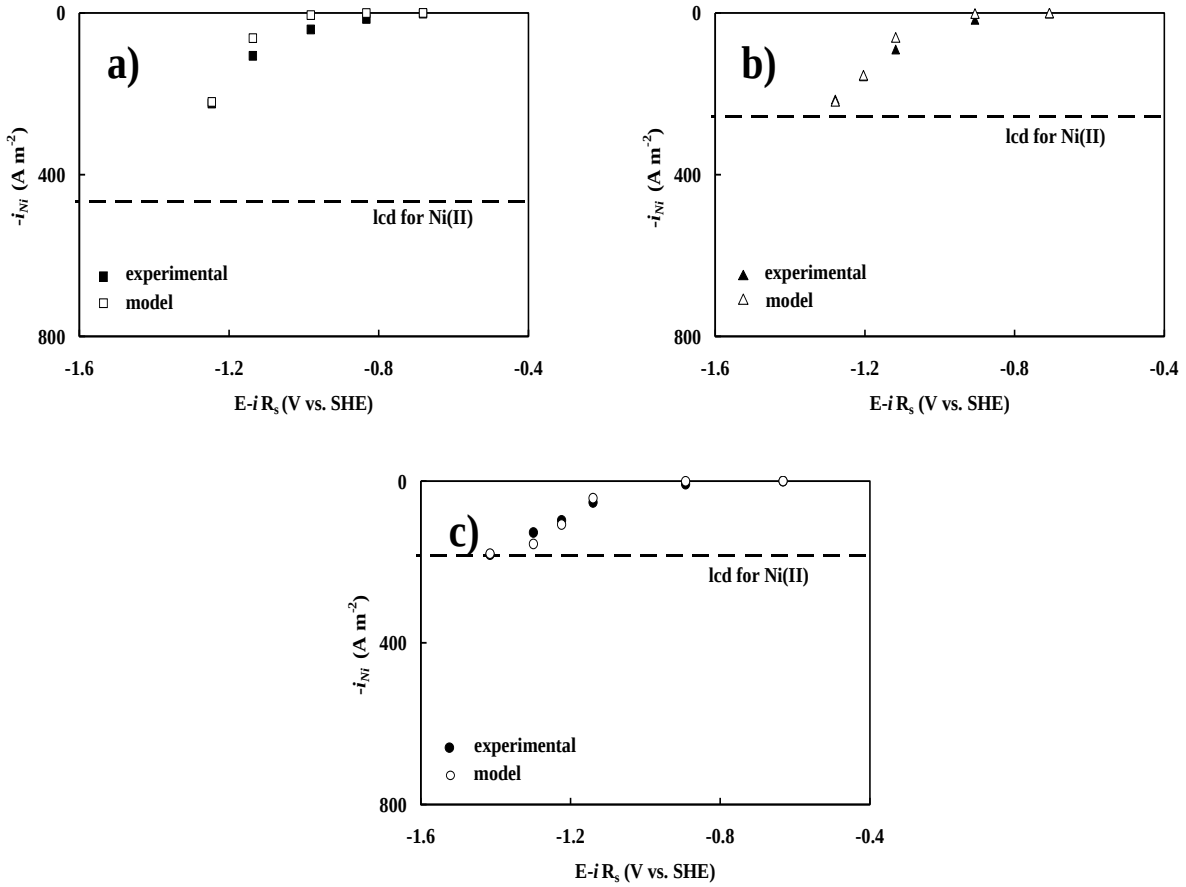

Figure 9.2. Variation of experimental (black symbols) and model-fitted (open symbols) partial current densities of nickel co-deposition with potential on a copper substrate rotating at 1000 rpm in solutions containing 1500 mol m^{-3} Na_2SO_4, 500 mol m^{-3} $B(OH)_3$ and different concentration ratios of $NiSO_4/CoSO_4$: a) 200/100, b) 100/50 and c) 50/50 at pH 3. The computed curves are generated using parameters listed in Tables 9.2 and 9.3. The limiting current densities are estimated with the Levich equation and $D_{Ni(II)}$ reported in Table 9.3 for each condition.

Figure 9.2 shows the experimental (black symbols) and model-fitted (open symbols) partial current densities for Ni(II) reduction during the overall processes analyzed in Figure

9.1. The experimental data were generated from ICP analysis of the nickel mass in the deposit. Also included on the plots are the limiting current densities (dashed line) for each of the experimental conditions as calculated using the Levich equation with the $D_{Ni(II)}$ values obtained from the fitting procedure (Table 9.3). As in the case of the total current densities in Figure 1, a very good agreement between the model and the experimental data is obtained over the entire potential range at the different $NiSO_4/CoSO_4$ concentration ratios. As expected, the current density for Ni(II) reduction increases as the $NiSO_4$ level in solution rises. It is also worth noting that both the experimental and model-fitted current densities approach the limiting current density determined from the Levich equation at the most negative potentials reached during the galvanostatic experiments when the $NiSO_4$ concentration is at its lowest level of 50 mol m^{-3} (Figure 9.2c), indicating that the system has reached very close to mass transfer limiting conditions.

Figure 9.3 shows the experimental (black symbols) and model-calculated (symbols) partial current densities for Co(II) reduction based on the contributions from the reaction pathways involving both intermediate $Co(I)_{ads}$ (reactions 5.1 and 5.2) and intermediate $NiCo(III)_{ads}$ (reactions 9.1 and 9.2). The experimental partial current densities of cobalt are also determined from the chemical analysis of the cobalt content in the deposited coatings. A comparison of the data in Figures 9.2 and 9.3 reveals that the partial current for cobalt deposition is always greater than that for nickel deposition at any given potential regardless of the bulk concentrations. This observation is another reflection of the aforementioned anomalous behavior whereby cobalt deposition occurs preferentially over nickel deposition.

Obviously, an important aspect of the model is that it can be used to assess the relative importance of the various steps in the reaction mechanism for this system to the electrode response. Although not shown in Figure 9.3, the model calculations clearly show that the contributions of the parallel reactions (9.1) and (9.2) for the formation and consumption of $NiCo(III)_{ads}$ are negligible over the entire potential range under all the conditions analyzed herein. Given the importance of this reaction pathway in the mechanism proposed by Zech et al [42], we have redone the fitting procedure a number of different ways to verify this result. These attempts included changing the initial guesses of the kinetic parameters associated with reactions (9.1) and (9.2) so as to enhance the current i_A and changing the technique for parameter estimation from the simplex method to a genetic algorithm.

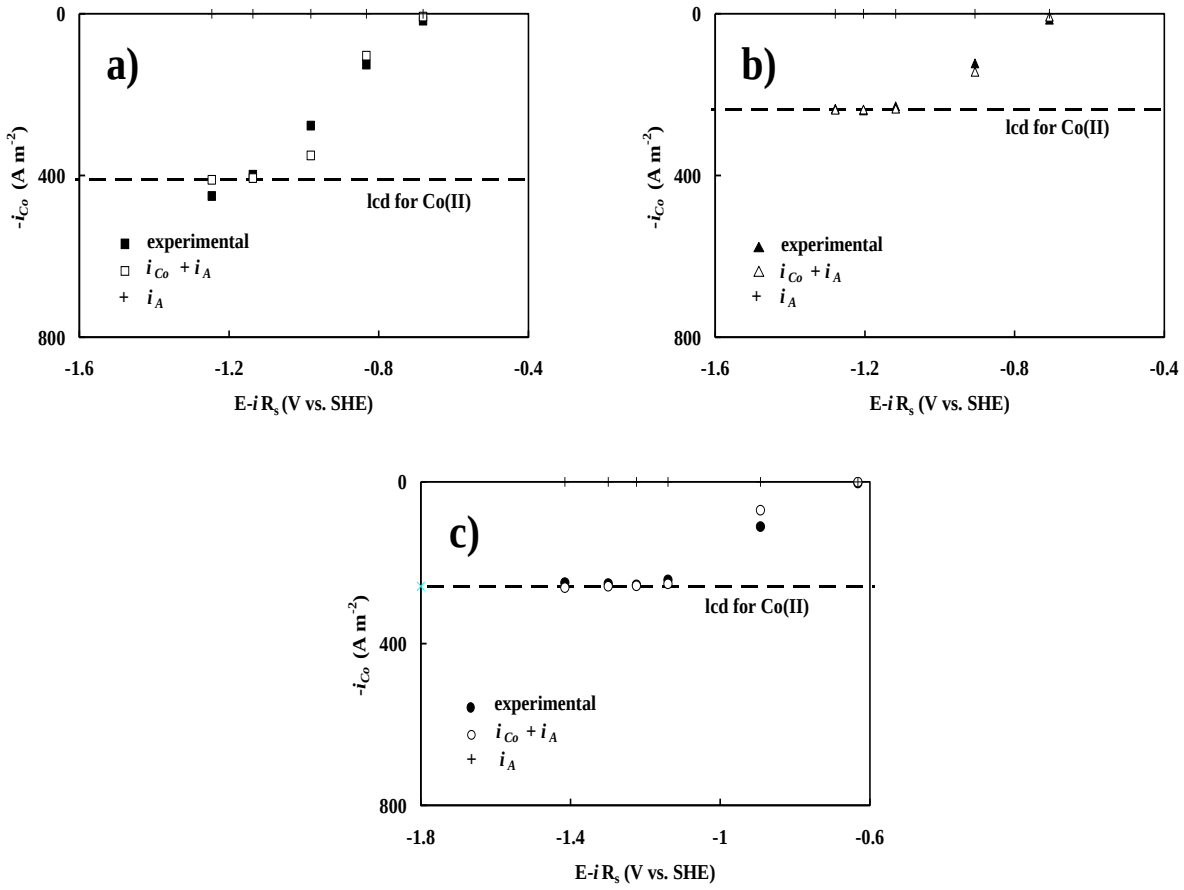

Figure 9.3. Variation of experimental (black symbols) and model-fitted (open symbols) partial current densities of cobalt co-deposition with potential on a copper substrate rotating at 1000 rpm in solutions containing 1500 mol m^{-3} Na_2SO_4, 500 mol m^{-3} $B(OH)_3$ and different concentration ratios of $NiSO_4/CoSO_4$: a) 200/100, b) 100/50 and c) 50/50 at pH 3. The computed curves are generated using parameters listed in Tables 9.2 and 9.3. The limiting current densities are estimated with the Levich equation and $D_{Co(II)}$ reported in Table 9.3 for each condition.

Genetic algorithms have advantages over traditional non-linear methods since it is less likely to lead to a situation where the search for the minimum sum-of-squares error becomes trapped in a local minimum. Thus, in classical methods (e.g. simplex) an optimal solution cannot always be achieved. The solvers in these non-linear methods generally use some form of gradient search technique to move along the steepest gradient until the lowest point (minimization) is reached. However, they may be subject to problems of convergence

to local optima, or in some cases, may be unable to find a feasible solution. This largely depends on the starting point of the solver. A starting point outside the feasible region may result in no feasible solution being found, even though feasible solutions may exist. Other starting points may lead to an optimal solution, but it is not possible to determine if it is a local or global optimum. In the case of a genetic algorithm, on the other hand, the population encompasses a range of possible outcomes. Solutions are identified purely on a fitness level, and therefore local optima are not distinguished from other equally fit individuals. Those solutions closer to the global optimum will thus have higher fitness values. Successive generations improve the fitness of individuals in the population until the optimisation convergence criterion is met. Thus, due to this probabilistic nature genetic algorithms tend to the global optimum. [104, 108]. However, the searches using a genetic algorithm led to the same parameter values and results as the original fitting procedure. We tried another approach of fitting only for the kinetic parameters associated with reactions (9.1) and (9.2) while keeping the parameters for reactions (5.1), (5.2), (6.1) and (6.2) fixed at the values obtained in our previous studies on single metal deposition of nickel and cobalt [41, 51]. However, this led to very poor fits of the overall model to the experimental data. Thus, contrary to the proposal made previously by Zech et al [42], this analysis shows that reactions (9.1) and (9.2) are not a significant pathway for cobalt deposition and cannot explain the anomalous behavior of the Ni-Co system. The removal of these reactions from the mechanism would have no observable effect on the computed electrode response. Thus, on the basis of our model, the explanation for the anomalous behavior must be related to the preferential surface coverage of $Co(I)_{ads}$ over that of $Ni(I)_{ads}$ or faster charge transfer for cobalt deposition in comparison to that of nickel. The relative importance of these two effects is further explored in the next section.

It is also worth mentioning that the computed electrode responses for Co(II) reduction are quite sensitive to the value of the diffusion coefficients (i.e. $D_{Co(II)}$, $D_{Ni(II)}$). For example, a small variation in $D_{Co(II)}$ from 2.41×10^{-10} to 2.74×10^{-10} $m^2 s^{-1}$ has a noticeable effect on the mass transport limiting plateau. As shown in Table 9.3, the fitted values of the diffusion coefficients for Ni(II), Co(II) and H^+ vary according to the electrolyte composition and tend to decrease as the concentration increases. The results show that the decrease of the diffusion coefficient of an ion does not depend on the concentration of that ion alone but on the concentration of the other species as well. Presumably, the variation of the diffusion

coefficients can be described in terms of the ionic strength of the solutions. The dependence of diffusion coefficients on concentration or ionic strength has been studied in the past and empirical expressions have been developed for this purpose [105, 106].

The weight percentage $W_{\%\,Ni}$ of nickel in the alloy is evaluated from the masses m_{Ni} and m_{Co} of nickel and cobalt, respectively, obtained from the ICP analysis of the coating, i.e.,

$$W_{\%\,Ni} = \frac{m_{Ni}}{m_{Ni} + m_{Co}} \times 100 \qquad (9.24)$$

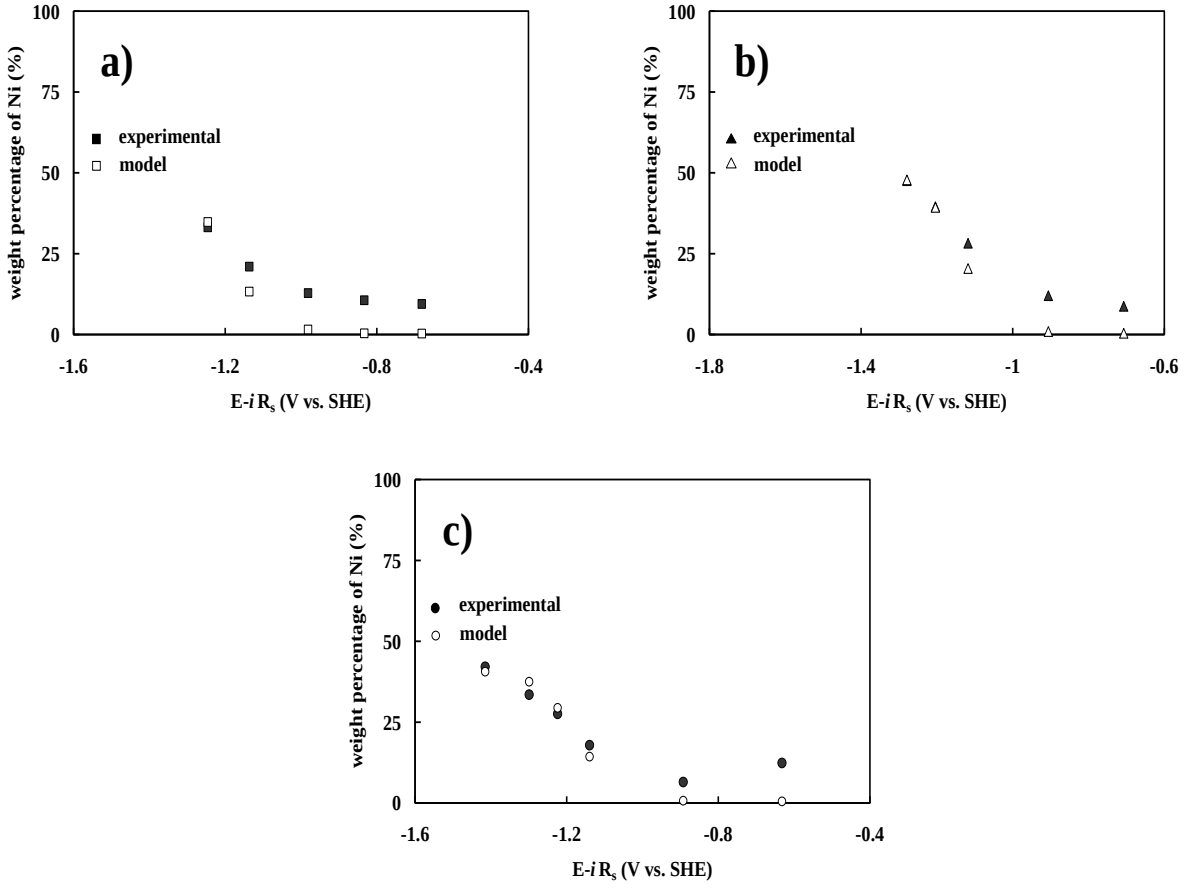

Figure 9.4. Variation of experimental (black symbols) and model-fitted (open symbols) alloy content (wt % Ni) with potential on a copper substrate rotating at 1000 rpm in solutions containing 1500 mol m^{-3} Na_2SO_4, 500 mol m^{-3} $B(OH)_3$ and different concentration ratios of $NiSO_4/CoSO_4$: a) 200/100, b) 100/50 and c) 50/50 at pH 3. The computed curves are generated using parameters listed in Tables 9.2 and 9.3.

As shown in Figure 9.4, the fitted values of $W_{\%\,Ni}$ agree well with the experimental values except at low overpotentials where the model tends to under-estimate the nickel

content. The results in Figure 9.4 confirm that the system is exhibiting anomalous behaviour for each of the conditions studied since the $w_{\%\,Ni}$ values always remain lower than the ratio $C^{b}_{Ni\,(II)} / \left(C^{b}_{Ni\,(II)} + C^{b}_{Co\,(II)}\right)$. However, in each of the plating baths studied, the nickel content in the alloy increases as the potential becomes more negative. An explanation becomes clear upon inspection of the variation of the partial current densities for Ni(II) and Co(II) reduction with potential in Figures 9.2 and 9.3. In all the cases, Co(II) reduction reaches mass transfer-limiting conditions at more positive potentials than does Ni(II) reduction. Anomalous behaviour arises due to kinetic factors. Consequently, as Co(II) reduction becomes more strongly influenced by mass transfer, it loses its kinetic advantage over Ni(II) reduction and the behaviour of the system becomes less anomalous.

Figure 9.5 shows the experimental (black symbols) and model-predicted (open symbols) partial current densities for the HER including contributions from both H^+ and water reduction. It is important to note that it is not possible to directly measure the partial current density for the HER and so the experimental data in this figure are not independently determined. Instead they are obtained from the previously presented experimental data by subtracting the partial current densities for Ni(II) reduction in Figure 9.2 and Co(II) reduction in Figure 9.3 from the total current density in Figure 9.1. As shown in Figure 9.5, the model calculations clearly show that both H^+ reduction and water reduction contribute significantly to the HER over the entire potential range. H^+ reduction predominates at low overpotentials, whereas water reduction becomes the main reaction at high overpotentials when the other reduction reactions (Ni(II) and Co(II) reduction as well as that of H^+) have become mass transfer-limited. Once metal deposition becomes limited by mass transport and cannot proceed faster, any further increase in the applied current during these galvanostatic experiments goes to decompose the solvent. This effect is most significant at the lowest metal concentration in the bath (Figure 9.5c).

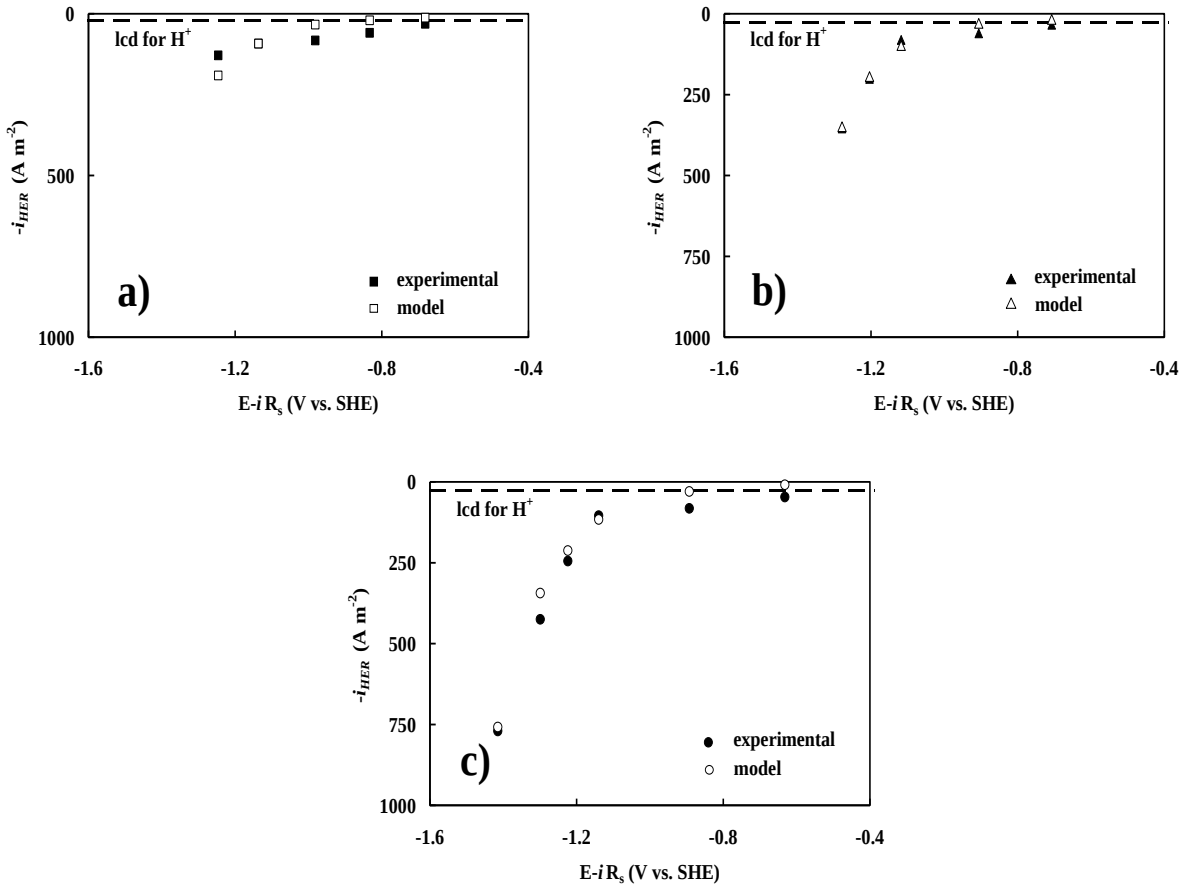

Figure 9.5. Variation of experimental (black symbols) and model-fitted (open symbols) partial current densities of HER with potential on a copper substrate rotating at 1000 rpm in solutions containing 1500 mol m^{-3} Na_2SO_4, 500 mol m^{-3} $B(OH)_3$ and different concentration ratios of $NiSO_4/CoSO_4$: a) 200/100, b) 100/50 and c) 50/50 at pH 3. The computed curves are generated using parameters listed in Tables 2 and 3. The limiting current densities are estimated with the Levich equation and D_H reported in Table 3 for each condition.

The importance of the HER is also reflected in the current efficiency for metal deposition which characterizes the percentage of total charge used to deposit the metals,

$$\text{i.e., } ce = \frac{i_{Ni} + i_{Co} + i_A}{i} \times 100 \qquad (9.25)$$

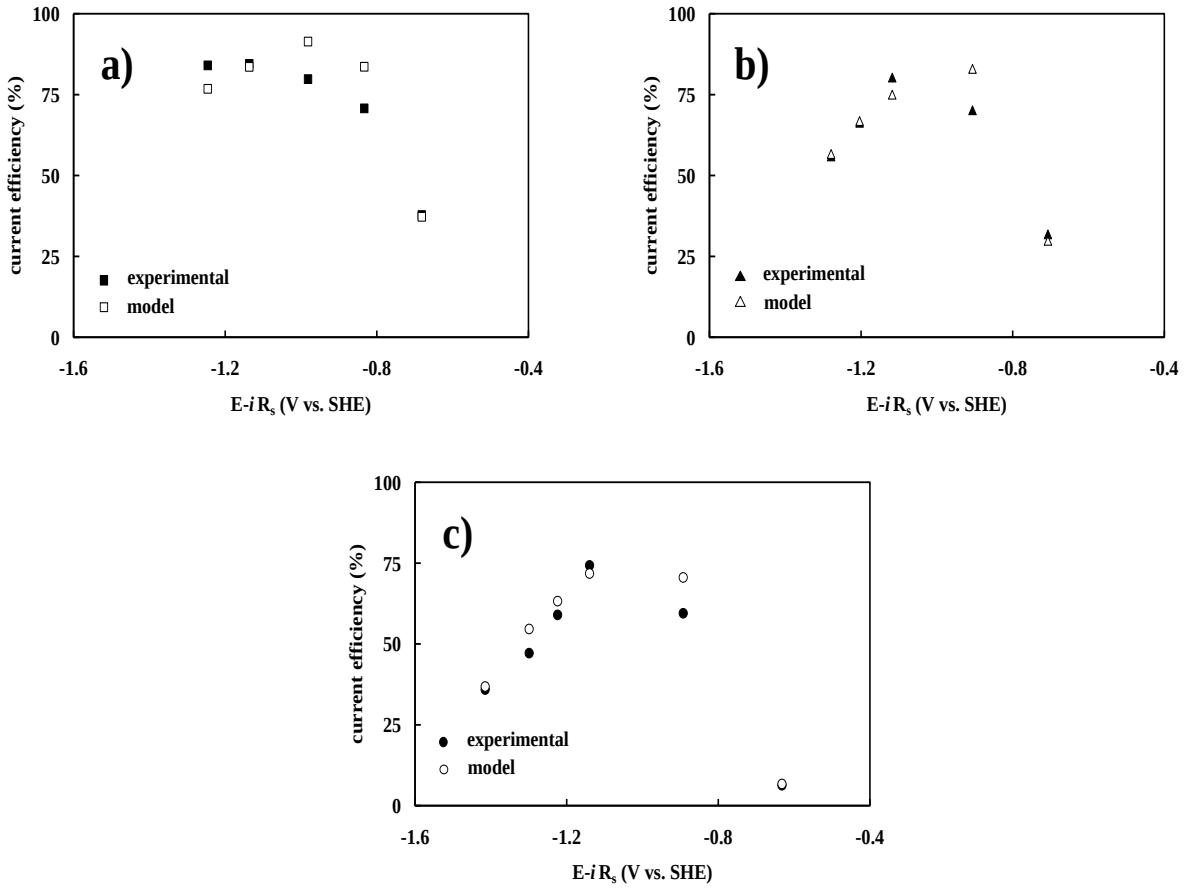

Figure 9.6. Variation of experimental (black symbols) and model-fitted (open symbols) metal deposition current efficiencies with potential on a copper substrate rotating at 1000 rpm in solutions containing 1500 mol m^{-3} Na_2SO_4, 500 mol m^{-3} $B(OH)_3$ and different concentration ratios of $NiSO_4/CoSO_4$: a) 200/100, b) 100/50 and c) 50/50 at pH 3. The computed curves are generated using parameters listed in Tables 9.2 and 9.3.

The variation of the experimentally derived and model-predicted current efficiencies with the steady state potential in the different solutions is shown in Figure 9.6. Figure 9.6c reinforces the finding from Figure 9.5 that the HER becomes more important as the metal concentration is lowered. Another important feature in Figure 9.6 is that both the experimental and model-predicted current efficiencies increase to a maximum at intermediate overpotentials before decreasing with further polarization. Such a maximum in current efficiency has been previously reported for the co-deposition of other iron-group alloys and attributed to the onset of mass transport effects on metal deposition [42]. As evident from

Figures 9.2, 9.3 and 9.5, H^+ reduction becomes mass transport-limited at potentials more negative than approximately –0.8 V where Ni(II) and Co(II) reduction are still kinetically controlled. Thus, as the potential becomes more negative than this value, the rate of metal deposition increases relative to that of H^+ reduction and so the current efficiency for metal deposition rises as well. However, once the applied current increases enough to approach the sum of the limiting current densities for the reduction of both metal ions, water reduction becomes significant and the current efficiency for metal deposition begins to decline as the current and the overpotential are further increased.

9.2.5 Analysis of the anomalous behavior

To date, the models presented by Matlosz [43], Baker and West [101], and Zech et al. [40] provide the best insights for the anomalous co-deposition of iron-group metal alloys. Matlosz considered that the preferential adsorption of the intermediate of the less noble metal (e.g., $Fe(I)_{ads}$) is the cause of the anomalous behavior. Baker and West took the same approach, but made a modification to the rate law for the first step of the reduction of the less noble metal. On the other hand, as discussed previously, Zech et al. proposed the formation of a mixed intermediate species (e.g. $NiCo(III)_{ads}$) which simultaneously can catalyze the deposition of the less noble metal and inhibit the deposition of the more noble metal. As pointed out by these last authors, theoretical predictions of models depend critically on the numerical values of the model parameters. This is a particularly telling point in view of the fact that no quantitative least-square fitting of the models to experimental data was done in any of these three earlier studies. Instead, only qualitative comparisons were made. Thus, the study described in this chapter presents the first analysis that is based on a least-square fitting of a model to experimental data for iron-group alloy co-deposition. In addition to this, the model presented in this study is the most comprehensive one to date and not only incorporates all of the phenomena described in these three previous studies but also accounts for several others that were not included, e.g., adsorption of H_{ads} intermediate on the electrode surface and convective mass transfer. Thus, our results can be used to assess their predictions and explanations for the origin of the anomalous behaviour.

As discussed in the previous section, our calculations clearly show that the current flowing through the pathway for Co(II) reduction via the $NiCo(III)_{ads}$ intermediate (i.e., reactions 9.1 and 9.2) proposed by Zech et al [40] is insignificant. Consequently, on the basis

of our analysis, we conclude that this route is not required in order to accurately model the behavior of the Ni-Co system. This difference may arise from the fact that our model accounts for a number of phenomena not considered by Zech et al. [40] (i.e., the buffering effect of boric acid, water dissociation, formation of the adsorbed H_{ads} intermediate during H^+ and water reduction and convective mass transfer) and that our model was actually fit (least-square) to experimental data.

In an effort to determine the origin of the anomalous behavior, other aspects of the model were more closely investigated. It has been proposed that blocking of Ni(II) from surface sites is an important factor for this phenomenon during the deposition of Ni-Fe alloys [41]. To examine this possibility for the Ni-Co system, we have plotted the variation of the computed steady state surface coverages θ_{Ni}, θ_{Co} and θ_{H} with electrode potential in Figure 9.7 for the three plating baths considered in this study. As shown in Figure 9.7b, the surface coverage of $Co(I)_{ads}$ in baths 2 and 3 remains very low at all potentials although the system still exhibits anomalous behavior under these conditions (see Figures 9.4b and c). Furthermore, the surface coverage of H_{ads} is always small at low overpotentials when the anomalous behavior is most apparent (Figure 7c).

Thus, a high surface coverage by $Co(I)_{ads}$ or H_{ads} is not a necessary factor for the anomalous Ni-Co co-deposition and so it does not appear that blocking of Ni(II) from surface sites is the problem. A more likely explanation becomes evident upon examination of the kinetic parameters in Table 9.2 obtained by fitting the model to the experimental data. The rate constant k_{01Co} for the first step of Co(II) reduction is more than 2 orders of magnitude larger than the corresponding rate constant k_{01Ni} for Ni(II) reduction. The values of these rate constants are important since the first step is rate controlling for the deposition of each metal. It appears that the faster kinetics of reaction (5.1) and Co(II) reduction than that of reaction (6.1) and Ni(II) reduction is the main factor accounting for anomalous co-deposition. Therefore, it may be appropriate to write the co-deposition reactions during the formation of Ni-Co alloys in sulphate media as follows:

$$Ni(II) + e^- \xrightarrow{Co(II)} Ni(I)_{ads} \qquad (9.26)$$

$$Ni(I)_{ads} + e^- \xrightarrow{Co(II)} Ni^0 \qquad (9.27)$$

$$Co(II) + e^- \xrightarrow{Ni(II)} Co(I)_{ads} \qquad (9.28)$$

$$Co(I)_{ads} + e^- \xrightarrow{Ni(II)} Co^0 \qquad (9.29)$$

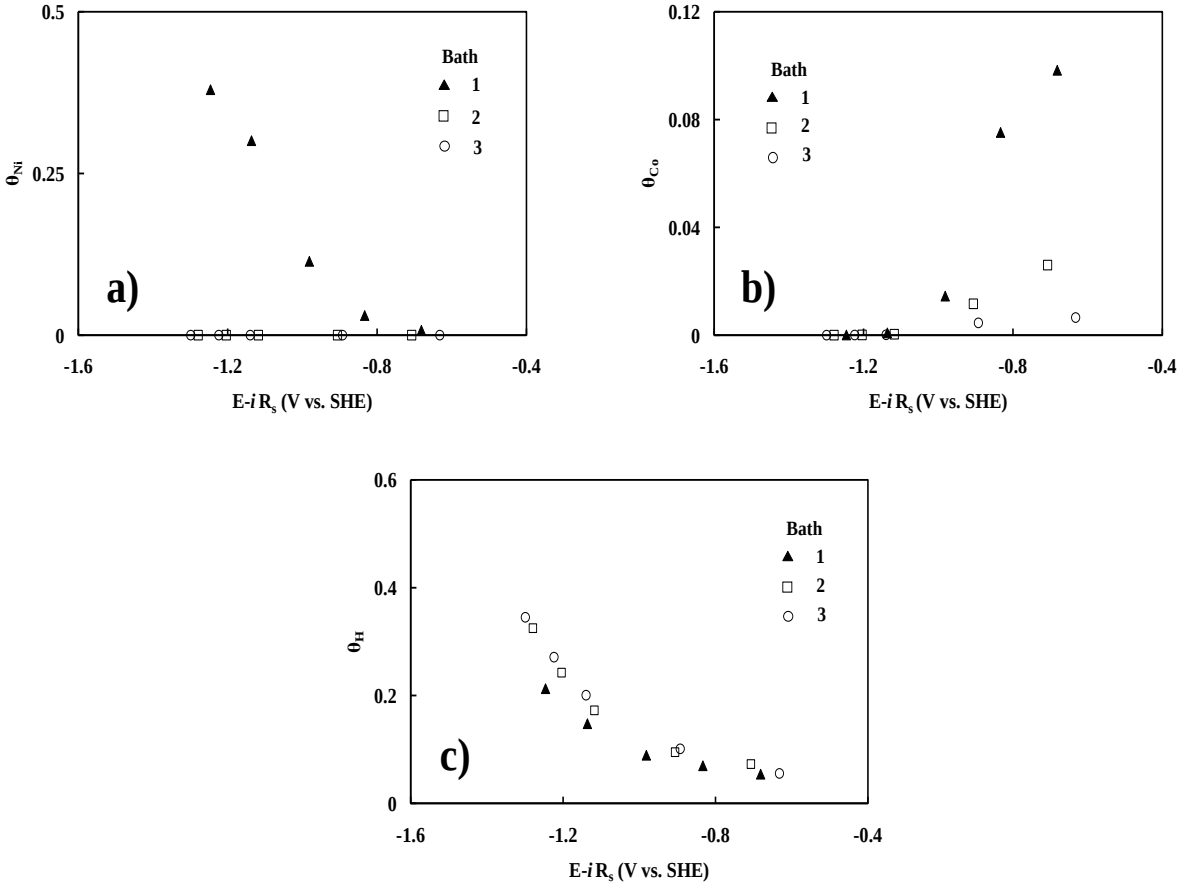

Figure 9.7. Variation of the computed steady state a) θ_{Ni}, b) θ_{Co} and c) θ_H with potential on a copper substrate rotating at 1000 rpm in solutions containing 1500 mol m^{-3} Na_2SO_4, 500 mol m^{-3} $B(OH)_3$ and different concentration ratios of $NiSO_4/CoSO_4$: a) 200/100, b) 100/50 and c) 50/50 at pH 3. The computed curves are generated using parameters listed in Tables 9.2 and 9.3.

As shown in Chapter 6 (section 6.3.1), Co(II) reduction onto cobalt and nickel substrates has faster kinetics than that of Ni(II) on the same substrates over a range of metal concentrations. This trend is similar to that observed in the current study on the alloy system. This observation calls into question to some extent the general view that the co-deposition of iron-group alloy systems exhibit anomalous behavior. Although it is reasonable to classify the co-deposition of Ni-Fe alloy coatings as being anomalous since Fe is a much less noble metal than Ni, the same may not hold in the case of the Ni-Co system. First of all, the Nernst potential for Co(II) reduction in sulphate solutions is virtually identical to that of Ni(II) reduction. Secondly, we have shown Co(II) reduction to have faster kinetics than Ni(II)

reduction in their single metal systems. For these reasons, the fact that it is preferentially deposited at all should not be surprising.

9.2.6 Influences of the HER and boric acid

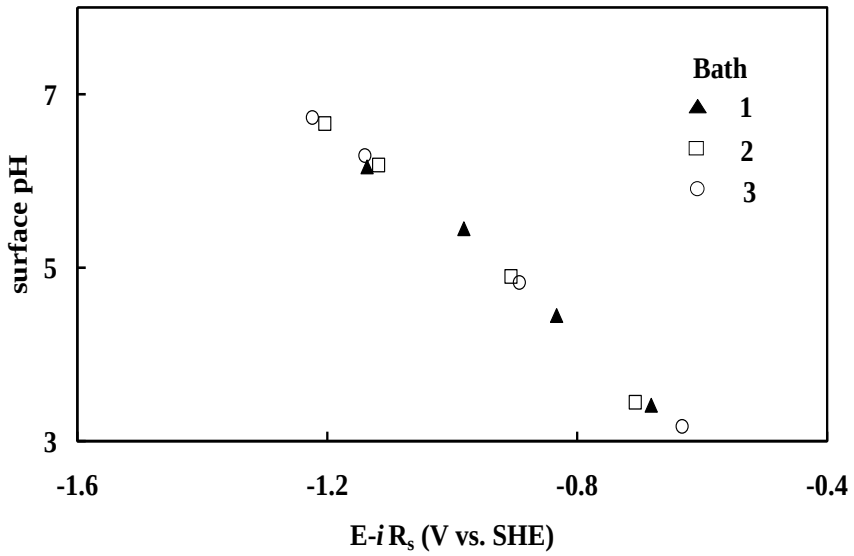

Figure 9.8. Variation of the computed steady state surface pH with potential on a copper substrate rotating at 1000 rpm in solutions containing 1500 mol m^{-3} Na_2SO_4, 500 mol m^{-3} $B(OH)_3$ and different concentration ratios of $NiSO_4/CoSO_4$: 200/100 (bath 1), 100/50 (bath 2) and 50/50 (bath 3) at pH 3. The computed curves are generated using parameters listed in Tables 9.2 and 9.3.

Another question that has been considered in previous studies on iron-group co-deposition is the effect of the HER during co-deposition. As shown in Figure 9.7c, the surface coverage of θ_H rises as the potential becomes more negative. This trend arises because of the enhancement of the first steps of the HER (i.e., reactions 9.7 and 9.9) as the overpotential increases and the formation of a large amount of H_{ads} on the electrode that cannot be as rapidly consumed by the chemical combination step (reaction 5.4) as they can at more positive potentials. As mentioned above, it does not appear that blocking of the electrode by H_{ads} is a critical factor for the anomalous behavior.

In sections 5.2.1 and 6.2.1, we discussed another possible process that could become a factor at high overpotentials. This concerns the formation of cobalt and nickel

oxides/hydroxides on the electrode surface if water reduction occurs to a significant enough extent that the surface pH rises to 6.8 for $Ni(OH)_{2(s)}$ (Figure 6.1) and 7.6 for $Co(OH)_{2(s)}$ (Figure 5.1c). Of course, the model presented in this study does not account for the formation of surface oxides/hydroxides. Nevertheless, it can be assessed to determine whether or not the electrode surface is ever predicted to reach a condition where these hydroxides can form on the basis of thermodynamic calculations. Figure 9.8 shows the variation of the surface pH with potential as computed by the model for the different plating baths. As observed from this figure, the interfacial pH is predicted to increase linearly with overpotential for all the conditions, but not to vary significantly with the $NiSO_4$ and $CoSO_4$ concentrations. The rise of the pH in the vicinity of the electrode is mitigated by the addition of $B(OH)_3$ to the electrolyte which undergoes hydrolysis to release H^+ ions (see Table 5.1 and reaction 5.19). The role that this reaction plays is examined in Figure 9.9 by plotting the variation of the surface concentrations of $B(OH)_3$ as a function of the potential. These calculations reveal the importance of $B(OH)_3$ in controlling the rise of the surface pH during co-deposition of the alloy. As the potential is made more negative and the surface pH rises, reaction 5.19 (Table 5.1) is shifted to the right and more $B(OH)_3$ is consumed in order to mitigate the depletion of the H^+ concentration due to the HER. The results in Chapter 5 and 6 for cobalt and nickel deposition have shown that the model predicts the surface pH to be higher when the $B(OH)_3/B_3O_3(OH)_4^-$ equilibrium is not considered in the model [95, 96].

As shown in Figure 9.8, the surface pH is predicted to reach ~6.73 when the electrode reaches its most negative value. Further thermodynamic calculations using the values for the surface concentrations of Co(II) and Ni(II) computed by the steady state model (i.e., $C^s_{Co(II)}$ = 0.26 mol m^{-3} and $C^s_{Ni(II)}$ =20.76 mol m^{-3}) at the most negative potential of –1.22 V reached during the steady state experiments reveal that the precipitation of $Co(OH)_{2(s)}$ and $Ni(OH)_{2(s)}$ would occur at pH ~8.97 and ~7.29, respectively. Thus, based on this analysis, it is not expected that these hydroxides should form on the electrode surface during the alloy formation of this study. Also, the fact that the model shows good agreement with the experimental data at high overpotentials (when the surface pH reaches its highest levels) suggests that oxide/hydroxide formation is not a significant factor under the experimental conditions considered in this study.

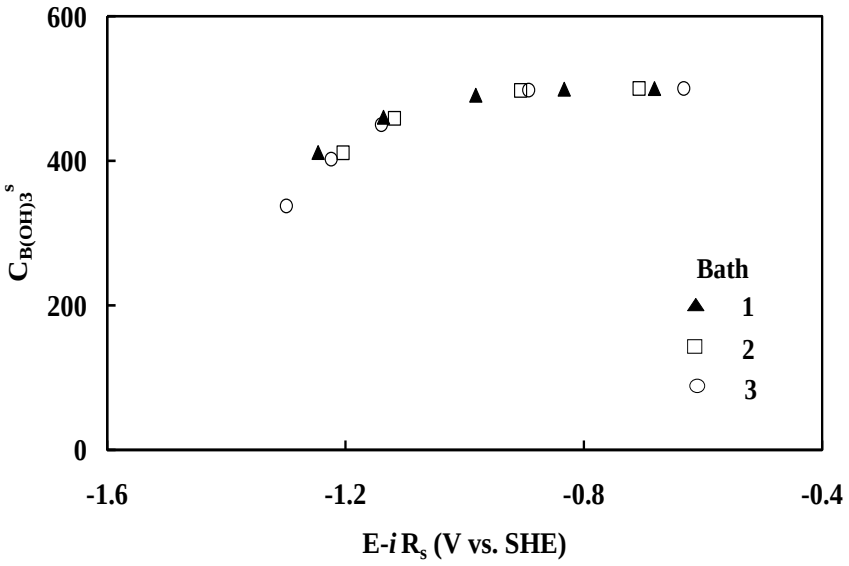

Figure 9.9. Variation of the computed surface concentrations of $B(OH)_3$ with potential on a copper substrate rotating at 1000 rpm in solutions containing 1500 mol m^{-3} Na_2SO_4, 500 mol m^{-3} $B(OH)_3$ and different concentration ratios of $NiSO_4/CoSO_4$: 200/100 (bath 1), 100/50 (bath 2) and 50/50 (bath 3) at pH 3. The computed curves are generated using parameters listed in Tables 9.2 and 9.3.

Chapter 10 Summary of Contributions and directions for future research

10.1 Summary of contributions

In this research, the electrodeposition of the single metals nickel and cobalt and Ni-Co alloys in sulphate media under different conditions (e.g. potential, current, electrolyte composition) has been investigated experimentally and through comprehensive modeling. A physicochemical model for cobalt electrodeposition onto a cobalt rotating disk electrode in sulphate-borate (pH 3) solutions was derived and fit using least-square methods to measured EIS spectra in **Chapter 5**. The model accounts for the simultaneous H_2 evolution by both H^+ and water reduction as well as diffusive and convective mass transport of dissolved species to and from the electrode surface. Based on a thermodynamic analysis of the solution chemistry for this system, $CoSO_{4(aq)}$, $B(OH)_{3(aq)}$, $B_3O_3(OH)_4^-$, H^+ and OH^- and two homogeneous reactions ($B(OH)_{3(aq)}$ hydrolysis and water dissociation) were considered in the model. The reaction mechanism involves the reduction of Co(II) by consecutive 1-electron transfer steps and the HER according to the Volmer-Tafel mechanism. $Co(I)_{ads}$ and H_{ads} intermediates form on the surface of the electrode in the first step of cobalt deposition and the HER, respectively. Fitting of the model to the experimental EIS spectra and a subsequent sensitivity analysis showed that the electrode response is very sensitive to kinetic parameters associated with the first step of Co(II) reduction, reflecting the fact that it controls the rate of deposition. On the other hand, the model shows only moderate sensitivity to parameters involved in H^+ reduction and near-complete insensitivity to water reduction over the range of potentials and Co(II) concentrations studied. Using the best-fit kinetic parameters, simulations were carried out to gain further insight into the behavior of the system under steady-state conditions. Evaluation of the partial current densities of Co(II), H^+ and water reduction showed that water reduction does not occur to any significant extent over the range of potentials considered in this study. A comparison of the computed surface pH with simpler models not considering the effects of the $B(OH)_3$ reveals that the rise of the surface pH is effectively mitigated by the hydrolysis of $B(OH)_3$ generating H^+ in the vicinity of the electrode. When $B(OH)_3$ hydrolysis is excluded from the model, the surface pH increases by approximately 2.6 units relative to the value obtained when it is included.

A similar analysis using EIS was carried out in Chapter 6 to analyze single nickel deposition. This study was conducted at more positive potentials than the one for cobalt deposition since it was found that nickel hydroxide formation occurs more easily than does cobalt hydroxide. The EIS model accounts for the same mass-transport effects as the model presented in Chapter 5 and the kinetic factors related to nickel deposition.Thermodynamic calculations corroborated the predominance in solution of the $NiSO_{4aq}$ ion pair during nickel plating at pH values between 3 and 6. A comparison of the voltammograms obtained for nickel and cobalt deposition reveals that Co(II) reduction exhibits faster kinetics than that of Ni(II) reduction. As in the case of cobalt deposition, analysis of the LSV in solutions revealed that $B(OH)_3$ clearly has no effect on the electrode response at lower overpotentials; however, at higher overpotentials, the curves are shifted toward more positive potentials in the presence of boric acid. The physicochemical model reveals that the surface pH tends to rise significantly at higher overpotentials primarily due to the water reduction reaction and that the hydrolysis of $B(OH)_3$ at the electrode surface acts to mitigate this effect by releasing H^+ into the solution.

A qualitative comparison of the EIS spectra obtained in $NiSO_4$ and $CoSO_4$ solutions discloses that the shapes of the spectra and the effect of potential and metal concentrations differ from each other. This could reflect significant differences in the rates of metal deposition or in the nature of the rate-controlling steps. For both the cobalt and nickel systems, it was not possible to determine one set of kinetic parameters that simultaneously fit the model to all EIS spectra obtained over the range of potentials and concentrations considered in this study. The variation of the kinetic parameters with metal concentration and potential can be explained in terms of the effects of solvent reorientation on ionic solvation during the charge-transfer processes that was not explicitly accounted for in the model due to the complexity of the interface. The following observations concerning the values of the kinetic parameters obtained from fitting the model to the EIS data can be made:

- The α_{Ni1} values are found to be less than 0.20, indicating a low-intermediate dependence on the applied potential, whereas the transfer coefficients for proton reduction (β_H) and the second step of nickel reduction (α_{Ni2}) always remain close to 0.5.
- The values of the rate constants for the first step of nickel deposition are of the same order of magnitude as those obtained for cobalt deposition. However, the transfer

coefficients are higher in the case of cobalt deposition. This explains the faster kinetics of Co(II) reduction in comparison with that of Ni(II).

- A comparison of the rate constants obtained for H^+ reduction during cobalt and nickel deposition showed that these parameters are virtually the same for both processes, suggesting that this reaction is unaffected by the nature of the two metals undergoing deposition.

The model also revealed that water reduction does not occur to any significant extent during nickel deposition over the range of potentials analyzed with EIS. The model showed some sensitivity to the value $\alpha_{Ni\,2}$ at low overpotential, which decreased significantly at high overpotential. This trend indicates that the first step of nickel deposition becomes progressively more rate-controlling as the potential becomes more negative.

The objective of **Chapter 7** was to extend the analysis of nickel deposition to higher overpotentials. A comprehensive physicochemical model for nickel electrodeposition extended from the presented in Chapter 6 to account for phenomena that can occur at more negative potentials was developed. This model was applied to experimental LSV measurements for this system since stable and reliable EIS measurements could not be obtained at higher ooverpotentials. The experiments and model calculations both supported the conclusion that H^+ reduction is the first cathodic process reaching completion during the scans, followed by nickel deposition. Although water reduction is the final reaction to begin, its rate rises very steeply once it is underway and experiences no mass transfer limitations, making it very important at high overpotentials. The hydrolysis of boric acid was also shown to mitigate the rise of the interfacial pH due to H^+ and water reduction and prevent the formation of nickel oxide or hydroxide on the electrode by the end of the scans. As with the EIS measurements, it was not possible to satisfactorily fit the model to the responses obtained over the entire range of experimental conditions with a single set of kinetic parameters. Comparison of the kinetic parameters obtained from EIS and LSV showed that their values can vary significantly depending on the experimental technique used. This effect may be due to differences in the effect of the input signals perturbing the system in the two cases on the re-organization of the solvent and other molecules adsorbed on the electrode surface during the experiments, which in turn can affect the kinetics of metal deposition.

A reaction mechanism for Ni-Co alloy formation in sulphate media (pH 3) based on LSV and steady-state polarization experiments was proposed in **Chapter 8**. The following

sequence of steps is proposed to occur on going from positive potentials toward more negatives ones: 1) H^+ reduction, 2) nickel deposition, 3) cobalt deposition, 4) simultaneous nickel inhibition and acceleration of cobalt deposition, 5) H_2O reduction, 6) formation of hydroxides (likely $NiOH_{(2)s}$) and 7) breakdown of the hydroxide film. Some dependence of alloy co-deposition on pH was observed. In particular, the precipitation of hydroxide species on the surface of the electrode is more likely to occur if $B(OH)_3$ is not present in solution. Also, it was found that the anomalous behavior is affected strongly by the $CoSO_4$ concentration and that Co(II) reduction becomes less preferred as it becomes more mass transfer-controlled or when the $NiSO_4$ concentration exceeds the $CoSO_4$ concentration by at least one order of magnitude. Thus, at high current densities the nickel content in the resulting alloy increases considerably as long as its deposition is not mass transport-limited. Evidence of the anomalous behavior in the alloys was found for conditions where H^+ reduction is not mass transport-controlled. Therefore, anomalous co-deposition cannot be attributed to the limiting current density for H^+ reduction being exceeded, as was proposed in the past. On the other hand, analysis of the variation of the pH showed that the acceleration of Co(II) reduction can be inhibited by HER as a consequence of the competition for electrons on the electrode surface and the adsorption of intermediates (i.e. H_{ads}). The current efficiency increased as the metal concentrations in solution were raised.

In **Chapter 9**, a steady state model for Ni-Co alloy deposition applicable to polarization experiments was developed and fit to measurements obtained at different $NiSO_4/CoSO_4$ concentration ratios in order to evaluate the kinetic parameters for the proposed reaction mechanism and diffusion coefficients of the electroactive species. The model can determine the total current densities, the partial current densities of nickel deposition, cobalt deposition and the HER, as well as the current efficiency for metal deposition. The analysis of the partial current densities and the limiting current density plateaus of metal deposition showed that both the kinetic parameters and diffusion coefficients obtained from fitting the model to the experimental data vary as the concentration is modified. This finding was not surprising since it is known that the diffusion coefficients of dissolved species decrease as the ionic strength of the solution increases. Further analysis of the model revealed that very little mixed intermediate ($NiCo(III)_{ads}$) forms on the surface of the electrode during alloy co-deposition and that the presence of this species is not required to explain the anomalous behavior of this system, contrary to a proposed mechanism appearing in the literature. The model also revealed that the preferential surface

coverage of $Co(I)_{ads}$ over that of $Ni(I)_{ads}$ is not required in order to accurately model the anomalous behavior of the Ni-Co system. Instead, the model indicates that the main factor accounting for anomalous Ni-Co alloy electrodeposition is the much faster charge-transfer of Co(II) reduction compared to that of Ni(II) reduction.

10.2 Directions for future research

Following are some proposals for future research to complement the present work.

- It would be interesting to incorporate in the models the effects of potential and metal concentration on solvent structure reorganization and adsorptive phenomena to account for the changes in the kinetic parameters that were observed depending on the experimental conditions and the experimental technique used to study metal deposition. One possible approach could be to incorporate some aspects of Marcus theory into the model equations.
- Incorporation of the explicit dependence of diffusion coefficient values on the ionic strength into the physicochemical models could improve the fits. Presumably a semi-empirical relation can be used for this purpose.
- The effects of migration on transport could be also incorporated into the model. Although its effects are minor when a concentrated supporting electrolyte is used, it could be important under certain conditions when the solutions contain higher metal concentrations.
- The models developed in this work could be also applied to the deposition of other iron-group alloys (e.g., Ni-Fe). The would allow us to determine if the finding from the present study that the faster charge-transfer of the less-noble component is the likely cause of anomalous co-deposition is true for other systems as well.
- Few impedance analyses for the formation of alloys have been reported in the literature. To the author's knowledge, no such research has been conducted on Ni-Co co-deposition. Although the use of this technique is restricted to conditions of low to intermediate overpotentials for systems in which H_2 evolution routinely occurs, it is a powerful technique for accurate determination of kinetic parameters. Such research would serve to complement the results obtained in this work.

- The formation of Ni-Co alloys using pulse-plating techniques is currently being analyzed. Studies using these techniques could be helpful in gaining more insight into the anomalous effects of the Ni-Co system. Perhaps more importantly, this would enable the many well known advantages of pulse plating such as improved morphology to be exploited through manipulation of the various variables associated with the pulse waveforms (i.e. pulse frequency, duty cycles, etc) that are unavailable to dc techniques.

References

[1] *Metals Handbook*, rev. ed., Am. Soc. for Metals, Cleveland, Ohio (1948).

[2] A. Brenner, *Electrodeposition of Alloys, Principles and Practice*, v. 1. Academic Press, New York (1963).

[3] R. M. Bozorth, *Ferromagnetism*, IEE Magnetics Society, New York (1993).

[4] G. W. Elmen, *J. Franklin Inst.*, 206 (1928) 317.

[5] A. Dolati, M. Sababi, E. Nouri and M. Ghorbani, *Materials Chemistry and Physics*, 102 (2007) 118.

[6] C. Q. Cui, S. P. Jiang, and A. C. C. Tseung, *J. Electrochem. Soc.*, 137 (1990) 3418.

[7] D. Golodnitsky, Y. Rosenberg and A. Ulus, *Electrochim. Acta*, 47 (2002) 2707.

[8] T. Osaka, M. Takai, K. Hayashi, K. I. Ohashi, M. Saito and K. Yamada, *Nature*, 392 (1998) 796.

[9] I. Paseka, *Electrochim. Acta*, 38 (1993) 2449.

[10] I. Paseka, *Electrochim. Acta*, 40 (1995) 1633.

[11] I. Paseka and Jana Velicka, *Electrochim. Acta*, 42 (1997) 237.

[12] B. Chi, J. Li, X. Yang, Y. Gong and N. Wang, *Int. J. Hydrogen Energy*, 30 (2005) 29.

[13] L. Brossard and C. Messier, *J. Appl. Electrochem.*, 23 (1993) 379.

[14] A. Restovic et al. *Electrochim. Acta*, 39 (1994) 1579.

[15] E. Gomez, J. Ramirez and E. Valles, *J. Appl. Electrochem.*, 28 (1998) 71.

[16] S. Goldbach, R. de Kermadec and F. Lapicque, *J. Appl. Electrochem,*. 30 (2000) 277.

[17] P.C. Andricacos and N. Robertson, *IBM J. Res. Develop.*, 42 (1998) 671.

[18] D. Kim, D. Y. Park, B.Y. Yoo, P.T.A. Sumodjo and N.V. Myung, *Electrochim. Acta*, 48 (2003) 819.

[19] P.T. Tang, H. Dylmer and P. Møller, *An Electroplating Method of Forming Platings of Nickel, Cobalt, Nickel Alloys and Cobalt Alloys with Reduced Stress*, EP 0835335 and US 6,036,833.

[20] G.W. Jernstedt, *Better Deposits at Greater Speeds by PR Plating*, Plating (reprint 4404) (1948).

[21] Y. Sverdlov et al, *Microelectronic Engineering*, 76 (2004) 258.

[22] E. Gomez, E. Pellicer and E. Valles, *Electrochemistry Communications*, 7 (2005) 275.

[23] S.S.P. Parkin, in: B. Heinrich, J.A.C. Bland (Eds.), *Ultrathin Magnetic Structures II*, Chap. 2, Springer, Berlin (1994).

[24] R. Wiart, *Electrochim. Acta*, 35 (1990) 1587.

[25] E. Barsoukov and J. R. Macdonald (Eds.), *Impedance Spectroscopy Theory, Experiment, and Applications*, 2nd ed. John Wiley & Sons, New Jersey (2005).

[26] D. Landolt, *Electrochim. Acta*, 39 (1994) 1075.

[27] F. A. Lowenheim (Ed.), *Modern Electroplating*, John Wiley & Sons, New Jersey (1974).

[28] B.E. Conway and J. O'M. Bockris, *Electrochim. Acta*, 3 (1961) 340.

[29] J. O'M. Bockris, in: J. O'M. Bockris and B. E. Conway (Eds), *Modern Aspects of Electrochemistry*, Vol. 1. Butterworth's, Washington, D. C (1954).

[30] E. H. Lyons, *J. Electrochem. Soc.*, 101 (1954) 376.

[31] A. J. Bard and L. R. Faulkner, *Electrochemical Methods: Fundamentals and Applications*, 2nd ed., John Wiley & Sons, New York (2001).

[32] F. Oplinger, *Met. Ind.*, 36 (1938) 513.

[33] D. Pletcher, *A First Course in Electrode Processes*, 1st. ed. The Electrochemical Consultancy, New York (1991).

[34] D. D. Macdonald, *Transient Techniques in Electrochemistry*, 1st. ed. Plenum Press, New York (1981).

[35] J. Newman and K. E. Thomas-Alyea, *Electrochemical Systems*, 3rd ed. John Wiley & Sons, New Jersey (2004).

[36] M. E. Huerta, "Copper Electrodeposition in the Absence and Presence of Chloride Ions and Polyethylene Glycol", PhD Thesis, University of Waterloo (2007).

[37] M. E. Orazem and B. Tribollet, *Electrochemical Impedance Spectroscopy*, 1st ed., John Wiley & Sons, New Jersey, 2008.

[38] I. Epelboin and R. Wiart, *J. Electrochem. Soc.*, 118 (1971) 1577.

[39] J.T. Matsushima, F. Trivinho-Strixino and E.C. Pereira, *Electrochim. Acta*, 51 (2006) 1960.

[40] J.S. Santos, R. Matos, F. Trivinho-Strixino and E.C. Pereira, *Electrochim. Acta*, 53 (2007) 644.

[41] J. Vazquez-Arenas and M. Pritzker, *J. Electrochem. Soc.*, 157 (2010) D283.

[42] N. Zech, E. J. Podlaha and D. Landolt, *J. Electrochem. Soc.* 146 (1999) 2892.

[43] M. Matlosz, *J. Electrochem. Soc.* 140 (1993) 2272.

[44] I. Epelboin, M. Joussellin and R. Wiart, *J. Electroanal. Chem.*, 119 (1981) 61.

[45] I. Epelboin, M. Joussellin and R. Wiart, *J. Electroanal. Chem.*, 157 (1983) 75.

[46] K. Y. Sasaki and J. B. Talbot, *J. Electrochem. Soc.*, 140 (1993) 669.

[47] C. C. Cheng and A. C. West, *J. Electrochem. Soc.*, 144 (1997) 3050.

[48] D. R. Gabe, *J. Appl. Electrochem.*, 27 (1997) 908.

[49] N. Zech and D. Landolt, *Electrochim. Acta*, 45 (2000) 3461.

[50] J. Matulis and R. Slizys, *Electrochim. Acta*, 9 (1964) 1177.

[51] J. Vazquez-Arenas and M. Pritzker, *Electrochim. Acta*, 55 (2010) 8376.

[52] I. Puigdomenech, INPUT, SED, and PREDOM: Computer programs, drawing equilibrium diagrams, TRITA-OOK-3010, Royal Institute of Technology, September (1983).

[53] Hydrochemical Equilibrium Constant Database (HYDRA), Inorganic Chemistry, Royal Institute of Technology (KTH), Stockholm, Sweden (2010).

[54] C. F. Baes and R. E. Mesmer, *The Hydrolysis of Cations*, Wiley, New York, 1976.

[55] A. Bousher, *J. Coord. Chem*., 31 (1995) 1.

[56] B. V. Tilak, A. S. Gendron and M. A. Mosoiu, *J. Appl. Electrochem.*, 7 (1977) 495.

[57] B. Boukamp, *Equivalent Circuit*, University of Twente, Netherlands, 1989.

[58] B. Tribollet and J. Newman, *J. Electrochem. Soc.*, 130 (1983) 2016.

[59] R. Greef, R. Peat, L. M. Peter, D. Pletcher and J. Robinson, *Instrumental Methods in Electrochemistry*, 1st. ed. John Wiley & Sons, Ontario (1985).

[60] Ionic conductivity and diffusion at infinite dilution, D. R. Lide (Ed.), *CRC Handbook of Chemistry and Physics*, Taylor & Francis, Boca Raton, 2004.

[61] E. Mattsson and J.O'M. Bockris, *Trans. Faraday Soc*., 55 (1959) 1586.

[62] J. O'M. Bockris and G. A. Razumney, *Fundamental Aspects of Electrocrystallization*, Plenum Press, New York, 1967.

[63] Nekrassov, private communication with Bockris (in J. O'M. Bockris and G. A. Razumney, *Fundamental Aspects of Electrocrystallization*, Plenum Press, New York, 1967).

[64] W. G. Proud and C. Mueller, *Electrochim. Acta*, 38 (1993) 405.

[65] L. B. Harris, *J. Electrochem. Soc*., 120 (1973) 1034.

[66] Jorge Vazquez-Arenas and M. Pritzker, *8th Int. Symp. on EIS,* Algarve, Portugal (2010).

[67] H. G. Bochmann and W. Vielstich, *Electrochim. Acta* 33, (1988) 805.

[68] H. H. Bauer, *J. Electroanal. Chem. Interfac. Electrochem.*, 16 (1968) 419.

[69] A. N. Frumkin, *Z. Elektrochem*. 59 (1955) 807.

[70] M.E. Huerta Garrido and M.D. Pritzker, *J. Electroanal. Chem.*, 594 (2006) 118.

[71] R.A. Marcus, *J. Chem. Phys.*, 24 (1956) 966.

[72] D. Yang and S. Sheu, *J. Chem. Phys.*, 22 (1997) 9361.

[73] W. J. Schmickler, *J. Electroanal. Chem.*, 82 (1977) 65.

[74] H. O. Finklea and D. H. Dwight, *J. Am. Chem. Soc.*, 114 (1992) 3173.

[75] K. B. Oldham, *J. Electroanal. Chem.*, 16 (1968) 125.

[76] P. T. Sanecki, P. M. Skital, *Electrochim. Acta*, 53 (2008) 7711.

[77] P. Delahay, *Double layer and Electrode Kinetics*. Interscience, New York (1965).

[78] N. Tanaka and A. Yamada, *Electrochim. Acta*, 14 (1969) 491.

[79] R. Orinakova, A. Turonova, D. Kladekova, M. Galova and R. M. Smith, *J. Appl. Electrochem*., 36 (2006) 957.

[80] S. N. Srimathi, S. M. Mayana and B. S. Sheshadri, *Surf. Technol*. 16 (1982) 277.

[81] M. Duch, J. Esteve, E. Gomez, R. Perez-Castillejos and E. Valles, *J. Micromech. Microeng*., 12 (2002) 400.

[82] B. Chi, J. Li, X. Yang, Y. Gong and N. Wang, *Int. J. Hydrogen Energy*, 30 (2005) 29.

[83] H. Barker (Ed), ASM Handbook, ASM International, Ohio (1992).

[84]Ch-Ch. Hu and A. Bai, *J. Electrochem. Soc*., 149 (2002) C615.

[85] A. Bai, Ch-Ch. Hu, *Electrochim. Acta*, 47 (2002) 3447.

[86] D. Golodnitsky, N.V. Gudin and G.A. Volyanuk, *J. Electrochem. Soc*., 147 (2000) 4156.

[87] Ch. Fan and D.L. Piron, *Electrochim. Acta* 41 (1996) 1713.

[88] N. Zech, E. J. Podlaha, and D. Landolt, *J. Appl. Electrochem.*, 28, 1251 (1998).

[89] N. Zech, E. J. Podlaha, and D. Landolt, *J. Electrochem. Soc.*, 146 (1999) 2886.

[90] H. Dahms and I. M. Croll, *J. Electrochem. Soc,* 112, 771 (1965).

[91] P. Andricacos, C. Arana, J. Tabib, J. Dukovic, and L. T. Romankiw, *J. Electrochem. Soc*., 136, 1336 (1989).

[92] R. M. Smith and A. E. Martell, *Critical Stability Constants*, Vol. 4, Plenum Press, New York (1989).

[93] K. Y. Sasaki, J. B. Talbot, *J. Electrochem. Soc*., 147 (2000) 189.

[94] S. Hessami, C.W. Tobias, *J. Electrochem. Soc*. 136 (1989) 3611.

[95] J. Vazquez-Arenas and M. Pritzker, submitted to *Electrochim. Acta*.

[96] J. Vazquez-Arenas, L. Altamirano-Garcia, M. Pritzker, R. Luna-Sánchez and R. Cabrera-Sierra, *J. Electrochem. Soc. J. Electrochem. Soc*., 158 (2011) D33.

[97] S. Glasstone, *J. Chem. Soc.*, 129 (1926) 2887.

[98] S. Glasstone, T. E. Symes, *Trans. Faraday Soc.*, 23 (1927) 213.

[99] C. B. F. Young, C. Egerman, *Trans. Electrochem. Soc.*, 72 (1937) 447.

[100] T. M. Harris and J. St. Clair, *J. Electrochem. Soc.*, 143 (1996) 3918.

[101] B. C. Baker and A. C. West., *J. Electrochem. Soc*., 144 (1997) 169.

[102] COMSOL 3.5a, 2008, User's Guide, COMSOL AB (USA).

[103] http://www.mathworks.com/access/helpdesk/help/techdoc/matlab.shtml, last accessed April 2011.

[104] http://www.mathworks.com/help/toolbox/gads/ga.html, last accessed March 2011.

[105] W. E. Price, R. Mills and L. A. Woolf, *J. Phys. Chem.*, 100 (1996) 1406.

[106] N. L. Burns, J. C. Clunie and J. K. Baird, *J. Phys. Chem*., 95 (1991) 3801.

[107] J. Vazquez-Arenas and M. Pritzker, submitted to *Electrochim. Acta*.

[108] Simon Mardle and Sean Pascoe, *Computers in Higher Education Economics Review*, 13 (1999).

[109] J. M. Saveant and D. Tessier, *J. Electroanal. Chem*., 65 (1975) 57.

[110] R.A. Marcus, J. Chem. Phys., 43 (1965) 679.

[111] K. Kontturi, J. A. Manzanares and L. Murtomaki, *Electrochimica Acta*, 18 (1995) 2979.

[112] T. Wandlowski, V. Marecek and Z. Samec, *J. Electroanal. Chem*. 242, (1988) 291.

[113] I. Benjamin, *Chem. Phys.*, 180 (1994) 287.

[114] D.M. Bates, D.G. Watts, Nonlinear Regression Analysis and its Applications, Wiley, New York (1988).

[115] D. Montgomery, Design and Analysis of Experiments, Wiley 5th edition, New York (1997).